Jansen, E., Raymo, M.E., Blum, P., et al., 1996
Proceedings of the Ocean Drilling Program, Initial Reports, Vol. 162

6. SITE 984[1]

Shipboard Scientific Party[2]

HOLE 984A

Position: 61°25.507′N, 24°04.939′W

Start hole: 1015 hr, 24 July 1995

End hole: 0245 hr, 25 July 1995

Time on hole: 16.5 hr (0.69 days)

Seafloor (drill pipe measurement from rig floor, mbrf): 1660.4

Total depth (drill pipe measurement from rig floor, mbrf): 1836.5

Distance between rig floor and sea level (m): 11.1

Water depth (drill pipe measurement from sea level, m): 1649.3

Penetration (mbsf): 176.1

Coring totals:
Type: APC
Number: 19
Cored: 176.1 m
Recovered: 180.16 m, 102.3%

Formation:
Unit I: 0–176.1 mbsf; Holocene to early Pleistocene; clay with silt, nannofossils, and mixed sediments

HOLE 984B

Position: 61°25.517′N, 24°04.949′W

Start hole: 0245 hr, 25 July 1995

End hole: 0815 hr, 28 July 1995

Time on hole: 77.5 hr (3.23 days)

Seafloor (drill pipe measurement from rig floor, mbrf): 1659.0

Total depth (drill pipe measurement from rig floor, mbrf): 2162.7

Distance between rig floor and sea level (m): 11.2

Water depth (drill pipe measurement from sea level, m): 1647.8

Penetration (mbsf): 503.7

Coring totals:
Type: APC
Number: 31
Cored: 293.5 m
Recovered: 299.55 m, 102.1%

Type: XCB
Number: 22
Cored: 210.2 m
Recovered: 158.71 m, 75.5%

Total:
Number: 53
Cored: 503.7 m
Recovered: 458.26 m, 91.0%

Formation:
Unit I: 0–503.7 mbsf; Holocene to late Pleistocene; clay with silt, nannofossils, and mixed sediments

HOLE 984C

Position: 61°25.524′N, 24°04.951′W

Start hole: 0815 hr, 28 July 1995

End hole: 0145 hr, 29 July 1995

Time on hole: 17.5 hr (0.73 days)

Seafloor (drill pipe measurement from rig floor, mbrf): 1659.7

Total depth (drill pipe measurement from rig floor, mbrf): 1950.1

Distance between rig floor and sea level (m): 11.2

Water depth (drill pipe measurement from sea level, m): 1648.5

Penetration (meters below seafloor, mbsf): 290.4

Coring totals:
Type: APC
Number: 31
Cored: 290.4 m
Recovered: 296.00 m, 101.9%

Formation:
Unit I: 0–290.4 mbsf; Holocene to late Pleistocene; clay with silt, nannofossils, and mixed sediments

HOLE 984D

Position: 61°25.528′N, 24°04.957′W

Start hole: 0145 hr, 29 July 1995

End hole: 1700 hr, 29 July 1995

Time on hole: 15.25 hr (0.64 days)

Seafloor (drill pipe measurement from rig floor, mbrf): 1659.1

Total depth (drill pipe measurement from rig floor, mbrf): 1929.8

Distance between rig floor and sea level (m): 11.1

Water depth (drill pipe measurement from sea level, m): 1647.9

Penetration (meters below seafloor, mbsf): 270.7

Drilled interval (mbsf): 0–157.8

Coring totals:
Type: APC
Number: 12
Cored: 112.9 m
Recovered: 115.22 m, 102.1%

Formation:
Unit I: 157.8–270.7 mbsf; Pleistocene to Pliocene; clay with silt, nannofossils, and mixed sediments

Principal results: A continuous sequence of sediments ranging in age from Holocene to late Pliocene (0–3.0 Ma) was recovered at Site 984 (BJORN-1), located on the eastern flank of the Reykjanes Ridge, at a shallower

[1]Jansen, E., Raymo, M.E., Blum, P., et al., 1996. *Proc. ODP, Init. Repts.,* 162: College Station, TX (Ocean Drilling Program).
[2]Shipboard Scientific Party is given in the list preceding the Table of Contents.

depth than Site 983. The primary drilling objective at Site 984 was to recover high-sedimentation-rate pelagic sequences with which to study climate evolution in the North Atlantic region over the last few million years. Biostratigraphic information suggests that the Site 984 sedimentary sequence is continuous, without significant hiatuses. Sedimentation rates were determined using magnetic polarity data combined with the biostratigraphic datums, and indicate accumulation rates of ~10–16 cm/k.y. Multisensor track data allowed the construction of a continuous composite section down to about 270 mbsf. Shipboard analyses document a section without hiatuses, well suited for high-resolution paleoclimatic studies, which will enable us to reach the scientific objectives of the site. Preliminary studies done on board indicate strong variance in a number of parameters on both Milankovitch and sub-Milankovitch time scales.

Sediments at Site 984 are predominantly composed of rapidly accumulated fine-grained terrigenous particles. Discrete ash layers occur throughout the upper sediment column, and pale to dark brown glass commonly occurs as a constituent of the silt- and sand-sized fractions. Authigenic iron sulfides, primarily in the form of disseminated pyrite, are also commonly present in minor amounts. The dominant lithologies include silty clay, clay, clayey nannofossil mixed sediment, and clay with variable amounts of nannofossils and silt. Nannofossil oozes with variable amounts of clay and sponge spicules also occur. As at Site 983, lithologic variation on decimeter to meter scales characterizes the sediment at this site, and is due to changes in the abundance of silt and biogenic materials relative to clay content. The range of variation in these components is smaller than in sediments of comparable age at Sites 980 to 982.

Only one lithostratigraphic unit is defined at Site 984 and is subdivided into four subunits, IA through ID. Changes in the spectral reflectance data, the character of the magnetic susceptibility signal, and the occurrence or abundance of minor lithologies, interbedded within the dominant clays and silty clays, define subunit boundaries at 120, 165, and 279 mbsf. While the sediments recovered at Sites 983 and 984 share many similarities, there are notable differences. These include the more common occurrence of dropstones at Site 984 possibly due to iceberg trajectories and/or increased melting in this region. Another difference between the two sites is the pronounced abundance of discrete ash layers in Subunits IA and IB at Site 984. This may be due to the proximity of Site 984 to Iceland, an obvious source of ash falls from discrete eruptions.

Calcium carbonate content in Hole 984B fluctuates between 0.4% and 32.2%, with an average value of 8.0%. $CaCO_3$ content gradually decreases downhole and fluctuates, having a lower amplitude with increasing depth. As at Site 983, the carbonate cycles of Hole 984B reflect glacial/interglacial fluctuations.

Calcareous nannofossils are generally abundant and well preserved in the upper 200 m at this site, with both the abundance and preservation deteriorating lower in the section. All the standard Quaternary nannofossil zones are recognizable. Like the nannofossils, planktonic and benthic foraminifers are generally well preserved and common throughout the late Pliocene to Holocene sequence at Site 984, but become progressively scarcer below 200 m. Diatoms vary in preservation and abundance while siliceous flagellates display scattered occurrences downsection in Holes 984A and 984B. The abundance of these microfossils ranges from trace to common, and the preservation from good to poor.

The Brunhes/Matuyama boundary and the Jaramillo, Olduvai, and Reunion Subchrons are well defined in Holes 984A, 984B, and 984C. The Olduvai and Reunion Subchrons are well defined in Hole 984D. The high fidelity of the magnetic polarity stratigraphy and the high sedimentation rates (~10–16 cm/k.y.) bode well for the possibility of high-resolution polarity transition records at Site 984. Below about 250 mbsf, the magnetic measurements became incoherent in conjunction with an abrupt increase in visible drilling disturbance.

As at Site 983, sulfate reduction and methanogenesis control the pore-water gradients of dissolved sulfate, ammonia, alkalinity, salinity, and phosphate. Sulfate decreases from near seawater values at the top of the section to zero at 120 mbsf. At this level, methane in headspace samples begins to increase, reaching a maximum between 260 and 280 mbsf. The C_1/C_2 ratios decrease consistently with burial depth due to the increasing influence of early diagenetic generation of hydrocarbons.

Physical properties show downhole changes related to normal compaction of the sediments, testifying to uninterrupted sedimentation at the site. Downhole temperature measurements on Cores 984B-3H through 13H, and 15H, 17H, and 19H, yielded an average temperature gradient of 105°C/km and a heat flow of about 0.1 W/m^2.

The seismic data acquired during the survey show the area adjacent to Site 984 to have a sedimentary section thickness of approximately 0.8–0.9 s (two-way traveltime) above acoustic basement. Acoustic stratification is subconformable with the seafloor, and with the exception of an angular unconformity near the seafloor to the south of Site 984, no indications of major erosion are observed in the seismic sections.

At Hole 984B, all three standard downhole logging tool strings were used. In addition, the geological high-resolution magnetometer tool (GHMT) was deployed. Preliminary comparison of logging results with core measurements of density, natural gamma radiation, and especially magnetic susceptibility show good correlations resolving cycles on the Milankovitch scale. Both laboratory and downhole logging velocity measurements show two short (2–3-m) intervals of high velocities around 400 mbsf. This corresponds to Reflector R4, a prominent seismic unit boundary. The downhole Formation MicroScanner (FMS), as well as the resistivity logs, also detected distinct changes at the same level, probably due to the presence of indurated beds. Furthermore, pore-water geochemistry indicate increased silicification of the sediments at this level.

BACKGROUND AND OBJECTIVES

Site 984 (BJORN-1) is located on the Bjorn Drift in approximately 1650 m water depth on the eastern flank of the Reykjanes Ridge (Fig. 1). The primary drilling objective at Site 984 was to recover high-sedimentation-rate pelagic sequences with which to study climate evolution in the North Atlantic region over the last few million years. The site is located within the core of Glacial North Atlantic Intermediate Water (GNAIW) during the last glaciation (Oppo and Lehman, 1983). Obtaining a long-term history of this water mass is one of the primary scientific objectives of this site. With the sediments in hand we should be able to extend such a record back to the "preglacial" Pliocene. In conjunction with Sites 980, 981, and 982 to the east, and Site 983 located in deeper waters just to the south, this site forms a depth transect of five sites roughly spanning the interval between 1 and 2 km water depth.

This same suite of sites also defines a northwest-southeast transect extending from ~24°W to ~14°W. Intercomparison of carbonate, faunal, and geochemical records from these sites should define changes in surface-water temperature and hydrography over the Pliocene–Pleistocene. In addition, Site 984 should prove very sensitive to Nordic Seas overflows across the Greenland-Scotland Ridge (GSR). This site lies on the northwest margin of the Iceland Basin directly downstream of overflows from the Iceland-Faeroe Ridge (see fig. 2, chapter 1, this volume). This water passes as a deep northern boundary current through the Charlie-Gibbs Fracture Zone south of Sites 983 and 984 (e.g., McCartney, 1992). Using this site, along with the other sites drilled north and south of the GSR, we hope to unravel the long-term history of deep- and intermediate-water formation in the Nordic Seas and subpolar North Atlantic. Comparison of $\delta^{13}C$ and trace element gradients between these sites should allow us to define glacial-interglacial changes in North Atlantic Intermediate Water formation. Such changes are implicated as a key driving force in conceptual models of atmospheric CO_2 variations and global climate change (Imbrie et al., 1992, 1993; Saltzman and Verbitsky, 1994); however, until now, the lack of high-quality records from high northern latitudes has precluded comprehensive evaluation of these hypotheses.

As predicted from previously studied piston and gravity cores in the region, we recovered a sedimentary sequence with unusually high

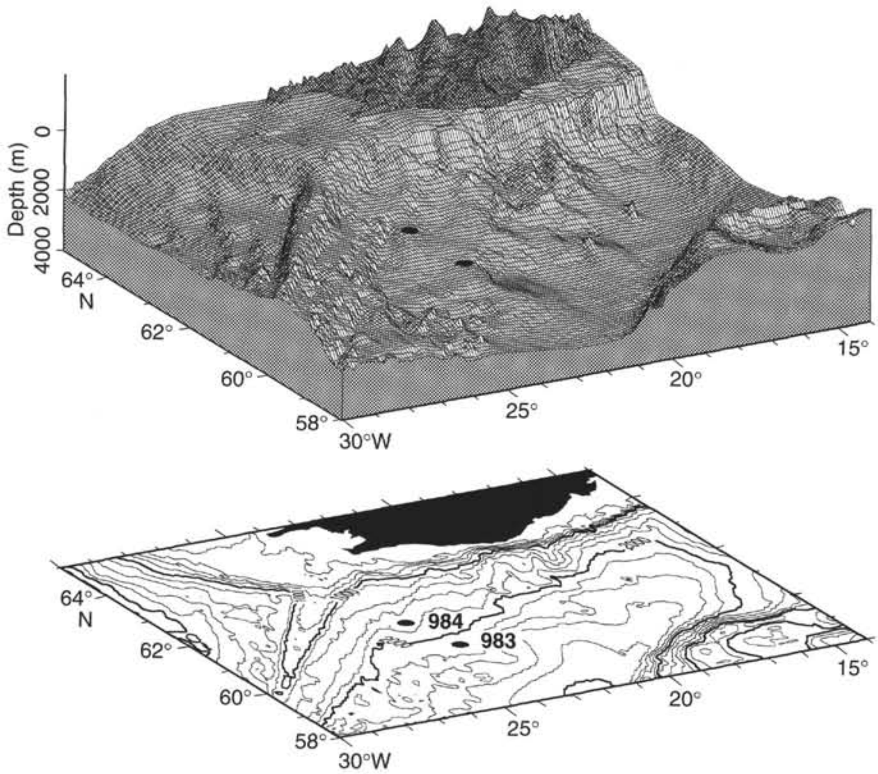

Figure 1. Detailed topographic view of Gardar and Bjorn Drift region showing location of Sites 983 and 984.

sedimentation rates (between 10 and 20 cm/k.y.). This will provide us with an unprecedented record of both glacial-interglacial and millennial-scale variations in thermohaline circulation, surface-water temperatures, and ice-rafting history over the late Pliocene and Pleistocene. In particular, we plan to investigate the long-term history of rapid century- to millennial-scale oscillations, such as those observed in temperature and dustiness in Greenland ice cores (Dansgaard-Oeschger events). In piston cores, such events can be seen as changes in surface foraminiferal fauna (sea-surface temperature), carbonate, color, and deep-ocean chemistry (e.g., Bond et al., 1992, 1993; Bond and Lotti, 1995; Fronval et al., 1995). The transitions between cold and warm epochs in ice cores are abrupt: ~6°C warmings and four-fold drops in dust content in as little as 20 years. Broecker (1994) reviews possible causes for these oscillations and the linkages between deep-sea sedimentation and ice-core records. One possibility is that millennial-scale climate variations in ice cores are related to the strength of the thermohaline "conveyor belt."

Site 984 will be used to address a number of questions relating to these "sub-Milankovitch" cycles. In particular, we expect to determine whether these rapid climate oscillations characterized the marine record during earlier, warmer climatic regimes, for instance, during the late Pliocene. We will look for variations in color, foraminiferal faunal composition, stable isotope composition, and lithic concentration. Many of the continuous records of physical properties collected on the ship (e.g., MST and spectral reflectance data) will be used for this purpose, and an early research priority will be to determine how these signals relate to lithologic variations in the sediment (e.g., Robinson and McCave, 1994).

Superimposed on the "Dansgaard-Oeschger" events of the last glacial period are "Heinrich" layers, events with longer characteristic repeat times (~10,000 yr), which may be related to surges of the eastern Laurentian and other major ice sheets (Heinrich, 1988; Bond et al., 1993; MacAyeal, 1993; Broecker, 1994; Fronval et al., 1995). Determining the geographic distribution of these Heinrich events, their long-term character, and the timing of their first occurrence is a main objective of our drilling on the Feni (Sites 980 and 981), Gardar (Site 983), and Bjorn (Site 984) Drifts. Are they restricted to the "100-k.y. world" of the Brunhes Chron, which was characterized by large marine-based continental ice sheets? Do they occur in intervals characterized by higher frequency variations in smaller ice sheets or in intervals prior to the existence of continental ice sheets? Do Heinrich events always have a characteristic repeat time of 10,000 years? What is the influence of orbital forcing on climate variability on frequency scales less than the ~20-k.y. precessional band?

By studying deep-water variability using carbon isotopes, Cd/Ca ratios, and other proxies, we will also be able to determine whether millennial-scale variations in surface temperature are associated with variations in thermohaline circulation (Boyle and Keigwin, 1987; Rahmstorf, 1994; Weaver and Hughes, 1994). Combining data from Site 983 with that from shallower and deeper drift sites (Sites 980, 981, and 984), we will examine if, and how, changes in the vertical nutrient distribution in the North Atlantic occur. By studying sedimentation patterns, surface-water properties, and deep-water variability on suborbital time scales and relating these observations to ice cores, we hope to better understand the forcing and dynamics of decadal to millennial climate variability in the North Atlantic–Arctic region.

We will also study the relationship between drift sedimentation rates and the strength of GSR overflows during the Pliocene–Pleistocene (e.g., Wold, 1994). Lastly, the numerous ash layers observed at Site 984 suggest that this site is close enough to Iceland to provide a detailed record of the long-term history of volcanism in this region.

OPERATIONS

The operational plan for proposed site BJORN-1 called for three piston-cored holes to approximately 300 m below seafloor, one of them to be deepened to approximately 500 mbsf using the XCB coring system. Core orientation was desired on at least two of the holes, along with the possibility of Adara temperature measurements on one hole. All four logging strings were to be deployed on the deepest hole.

After a brief, 57-nmi transit to Site 984 (BJORN-1), the vessel slowed to survey speed (6.0 kt) at 0636 hr on 24 July 1995 and the seismic profiling gear was deployed for a short seismic site survey (see "Seismic Stratigraphy" section, this chapter). By 1020 hr on 24 July the seismic profiling gear had been recovered, the vessel had returned to the drilling location based on GPS coordinates, and the positioning beacon had been deployed, initiating Hole 984A.

A standard APC/XCB bottom-hole assembly was used for all holes at Site 983, including a nonmagnetic drill collar. Subsequent (B and C) holes were offset 15 m to the north. The mudline was established for each hole. The APC firing depth was offset by a few meters for subsequent holes to establish continuous sediment sections. Position, depths, and coring totals for each hole are summarized at the top of this chapter. All cores are listed in Table 1.

Routine piston coring at Hole 984A proceeded until the core barrel for Core 984-20H jammed inside the drill pipe while running in the hole. The barrel was stuck at approximately 1605 m depth. After several limited attempts to free the barrel, the overshot shear pin was sheared and the sinker bar string with the Tensor core orientation hardware was recovered. The orientation gear was removed and the sinker bar string was run in for another, more vigorous but unsuccessful attempt at jarring the barrel free. The decision was made to abandon the hole and the drill pipe cleared the seafloor at 0246 hr on 25 July 95, ending Hole 984A. Upon recovery the barrel was found jammed by a shear-pin stub.

At Hole 984B, APC coring proceeded without incident until Core 984A-31H required 100,000 lb of overpull and drill-over to recover.

Table 1. Coring summary for Site 984.

Core	Date (July 1995)	Time (UTC)	Depth (mbsf)	Length cored (m)	Length recovered (m)	Recovery (%)
162-984A-						
1H	24	1440	0.0–5.1	5.1	5.09	99.8
2H	24	1500	5.1–14.6	9.5	8.24	86.7
3H	24	1530	14.6–24.1	9.5	9.73	102.0
4H	24	1555	24.1–33.6	9.5	9.74	102.0
5H	24	1625	33.6–43.1	9.5	9.09	95.7
6H	24	1655	43.1–52.6	9.5	9.76	103.0
7H	24	1725	52.6–62.1	9.5	9.89	104.0
8H	24	1755	62.1–71.6	9.5	9.89	104.0
9H	24	1830	71.6–81.1	9.5	9.84	103.0
10H	24	1855	81.1–90.6	9.5	9.96	105.0
11H	24	1930	90.6–100.1	9.5	9.84	103.0
12H	24	1955	100.1–109.6	9.5	9.96	105.0
13H	24	2025	109.6–119.1	9.5	9.86	104.0
14H	24	2055	119.1–128.6	9.5	9.92	104.0
15H	24	2125	128.6–138.1	9.5	9.87	104.0
16H	24	2150	138.1–147.6	9.5	9.90	104.0
17H	24	2220	147.6–157.1	9.5	9.88	104.0
18H	24	2255	157.1–166.6	9.5	9.84	103.0
19H	24	2325	166.6–176.1	9.5	9.90	104.0
			Coring totals:	176.1	180.20	102.3
162-984B-						
1H	25	1105	0.0–8.5	8.5	8.43	99.2
2H	25	1140	8.5–18.0	9.5	9.77	103.0
3H	25	1240	18.0–27.5	9.5	9.81	103.0
4H	25	1330	27.5–37.0	9.5	9.86	104.0
5H	25	1425	37.0–46.5	9.5	10.01	105.3
6H	25	1520	46.5–56.0	9.5	9.81	103.0
7H	25	1615	56.0–65.5	9.5	10.11	106.4
8H	25	1710	65.5–75.0	9.5	9.98	105.0
9H	25	1750	75.0–84.5	9.5	9.96	105.0
10H	25	1825	84.5–94.0	9.5	9.58	101.0
11H	25	1900	94.0–103.5	9.5	9.92	104.0
12H	25	1940	103.5–113.0	9.5	9.99	105.0
13H	25	2015	113.0–122.5	9.5	9.92	104.0
14H	25	2050	122.5–132.0	9.5	9.29	97.8
15H	25	2125	132.0–141.5	9.5	9.95	105.0
16H	25	2150	141.5–151.0	9.5	9.84	103.0
17H	25	2225	151.0–160.5	9.5	9.59	101.0
18H	25	2255	160.5–170.0	9.5	9.79	103.0
19H	25	2330	170.0–179.5	9.5	9.57	101.0
20H	26	0000	179.5–189.0	9.5	9.69	102.0
21H	26	0040	189.0–198.5	9.5	9.62	101.0
22H	26	0115	198.5–208.0	9.5	9.54	100.0
23H	26	0140	208.0–217.5	9.5	9.71	102.0
24H	26	0235	217.5–227.0	9.5	9.46	99.6
25H	26	0305	227.0–236.5	9.5	9.71	102.0
26H	26	0335	236.5–246.0	9.5	9.64	101.0
27H	26	0405	246.0–255.5	9.5	9.82	103.0
28H	26	0435	255.5–265.0	9.5	9.38	98.7
29H	26	0505	265.0–274.5	9.5	9.32	98.1
30H	26	0535	274.5–284.0	9.5	9.00	94.7
31H	26	0705	284.0–293.5	9.5	9.46	99.6
32X	26	0830	293.5–301.8	8.3	9.86	119.0
33X	26	0930	301.8–311.4	9.6	9.89	103.0
34X	26	1045	311.4–321.0	9.6	9.03	94.0
35X	26	1220	321.0–330.6	9.6	9.91	103.0
36X	26	1330	330.6–340.2	9.6	6.19	64.5
37X	26	1420	340.2–349.8	9.6	9.82	102.0
38X	26	1515	349.8–359.4	9.6	9.97	104.0
39X	26	1600	359.4–369.1	9.7	9.70	100.0
40X	26	1635	369.1–378.7	9.6	9.84	102.0
41X	26	1740	378.7–388.4	9.7	9.19	94.7
42X	26	1820	388.4–398.0	9.6	9.70	101.0
43X	26	1900	398.0–407.6	9.6	9.85	102.0
44X	26	1945	407.6–417.3	9.7	9.79	101.0
45X	26	2035	417.3–426.9	9.6	9.80	102.0
46X	26	2120	426.9–436.5	9.6	9.63	100.0
47X	26	2210	436.5–446.1	9.6	9.88	103.0
48X	26	2250	446.1–455.7	9.6	0.00	0.0
49X	26	2325	455.7–465.3	9.6	0.00	0.0
50X	27	0030	465.3–474.9	9.6	0.00	0.0
51X	27	0130	474.9–484.5	9.6	0.00	0.0
52X	27	0245	484.5–494.1	9.6	0.00	0.0
53X	27	0400	494.1–503.7	9.6	6.66	69.4
			Coring totals:	503.7	458.26	91.0
162-984C-						
1H	28	1020	0.0–6.8	6.8	6.79	99.8
2H	28	1115	6.8–16.3	9.5	9.67	102.0
3H	28	1140	16.3–25.8	9.5	9.82	103.0
4H	28	1200	25.8–35.3	9.5	9.79	103.0
5H	28	1225	35.3–44.8	9.5	9.77	103.0
6H	28	1250	44.8–54.3	9.5	9.84	103.0
7H	28	1325	54.3–63.8	9.5	10.03	105.6
8H	28	1340	63.8–73.3	9.5	9.96	105.0
9H	28	1405	73.3–82.8	9.5	9.90	104.0
10H	28	1430	82.8–92.3	9.5	9.97	105.0
11H	28	1455	92.3–101.8	9.5	10.04	105.7
12H	28	1520	101.8–111.3	9.5	9.92	104.0
13H	28	1540	111.3–120.8	9.5	9.87	104.0
14H	28	1605	120.8–130.3	9.5	9.96	105.0
15H	28	1630	130.3–139.8	9.5	9.94	104.0
16H	28	1650	139.8–149.3	9.5	9.88	104.0
17H	28	1715	149.3–158.8	9.5	9.95	105.0
18H	28	1745	158.8–168.3	9.5	9.89	104.0
19H	28	1810	168.3–177.8	9.5	9.83	103.0
20H	28	1835	177.8–187.3	9.5	9.90	104.0
21H	28	1900	187.3–196.8	9.5	9.95	105.0
22H	28	1925	196.8–206.3	9.5	9.58	101.0
23H	28	1950	206.3–215.8	9.5	9.80	103.0
24H	28	1915	215.8–225.3	9.5	9.81	103.0
25H	28	2050	225.3–234.8	9.5	9.72	102.0
26H	28	2120	234.8–244.3	9.5	9.74	102.0
27H	28	2145	244.3–253.8	9.5	9.59	101.0
28H	28	2210	253.8–263.3	9.5	9.21	96.9
29H	28	2245	263.3–272.8	9.5	9.65	101.0
30H	28	2310	272.8–282.3	9.5	6.15	64.7
31H	28	2345	282.3–290.4	8.1	8.08	99.7
			Coring totals:	290.4	296.00	101.9
162-984D-						
1H	29	0335	0.0–8.4	8.4	8.37	99.6
2H	29	0710	166.2–175.7	9.5	9.88	104.0
3H	29	0740	175.7–185.2	9.5	9.94	104.0
4H	29	0810	185.2–194.7	9.5	9.62	101.0
5H	29	0840	194.7–204.2	9.5	9.80	103.0
6H	29	0910	204.2–213.7	9.5	9.67	102.0
7H	29	0940	213.7–223.2	9.5	9.59	101.0
8H	29	1010	223.2–232.7	9.5	9.82	103.0
9H	29	1040	232.7–242.2	9.5	9.68	102.0
10H	29	1110	242.2–251.7	9.5	9.68	102.0
11H	29	1135	251.7–261.2	9.5	9.53	100.0
12H	29	1205	261.2–270.7	9.5	9.64	101.0
			Coring totals:	112.9	115.2	102.1

XCB coring was initiated with Core 984B-32X and continued with remarkable recovery (100%) until Core 984B-48X. Beginning at a depth of 446.1 mbsf, five straight zero-recovery cores were taken. All attempts to recover the formation proved futile. The final Core 984B-53X reached scientific target depth and recovered 6.6 m of what appeared to be a similar, perhaps slightly more friable, formation as had been recovered earlier with good success. No satisfactory explanation of the recovery problems was found.

Upon completion of coring operations at Hole 984B, two annular-hole volumes of seawater were circulated and a wiper trip with the drill string was made to 1759.0 m (100.0 mbsf). No overpull or drag was identified during the wiper trip and no fill identified on bottom. The go-devil for locking open the LFV was pumped downhole and the pipe was pulled to a logging depth of 102.2 mbsf. The hole was considered to be in excellent condition and therefore it was unnecessary to displace it with mud for logging. Four successful logging runs (Quad combo, FMS, GHMT, and geochemical tool) were made, and all tool strings reached to within 3.7 m or less of bottom (see "Wireline Logging" section, this volume).

At Hole 984C, APC coring proceeded until the scientific target had been reached. Severe liner collapse problems were encountered on the final two cores. The barrel for Core 984C-30H was actually removed from the pipe with several feet of liner (with core) dangling below the shoe. The liner had collapsed and stretched, resulting in a significantly reduced outer diameter.

Because Hole 984A was terminated prematurely it was decided to once again offset the vessel 15 m north and spud Hole 984D. After establishing mudline with Core 984D-1H, the hole was deepened by drilling ahead an additional 157.8 m. Continuous APC coring then commenced at a depth of 166.2 mbsf and continued until the scientific target for the hole had been reached. Coring was terminated slightly higher than on Hole 984C to avoid a repeat of the severe liner collapse problems encountered on the final two cores of that hole.

Adara temperature measurements were taken continuously on Cores 984B-3H through 13H and Cores 984B-15H, 17H, and 19H. The bottom-water temperature was measured with the Adara tool before taking Core 984D-1H. The following cores were oriented with the Tensor tool: Cores 984A-3H through 19H and Cores 984B-3H through 19H.

The positioning beacon was released and subsequently recovered at 1420 hr on 29 July. The vessel was secured for transit and got underway for Site 907 (ICEP-1) at 1742 hr on 29 July 1995.

COMPOSITE DEPTHS

Continuity of the sedimentary sequence at Site 984 was documented for the upper 245 mbsf (meters below seafloor), extending from the upper Pliocene to the Holocene. Sufficient overlap between the cores drilled in the upper parts of the holes at this site allowed a composite section to be developed, as discussed in the "Composite Depth" section, "Explanatory Notes" chapter (this volume). Hole 984A was terminated due to drilling problems at Core 984A-19H. Core 984D-1H was drilled to confirm recovery of the mudline, and to ensure overlap at the first core break. Cores 984D-2H (166.2 mbsf) and below extend the record from Hole 984A. The offsets that comprise the composite depth section at Site 984 are given in Table 2.

Multisensor-track (MST) data used in correlations are displayed on the composite depth scale in Figure 2 (see also back pocket). Magnetic susceptibility was the primary parameter used to develop the composite section. Gamma-ray attenuation porosity (GRAPE), natural gamma radiation, and *P*-wave velocity measurements from the MST, and percentage spectral reflectance in the 650–700-nm band (see "Lithostratigraphy" section, this chapter), were also used to confirm the hole-to-hole correlations. Susceptibility, natural gamma radiation, and GRAPE data showed a weak positive correlation through much of the depth range of the composite section, with common exceptions. The relative independence of the three parameters made the splice more precise by allowing features that were not apparent in one data set to be correlated in another.

The base of the composite depth section is at 267 mcd. The remainder of the Hole 984B cores have been appended to the composite section below this depth. No adjustment of relative depths of the Hole 984B cores was made below 267 mcd.

The mcd scale grows relative to the mbsf scale in all four holes by about 10% over the range of the composite section as shown in Figure 3. This growth is presumably caused by physical expansion of the cores after recovery and by stretching of the sequence during the coring process.

After construction of the composite depth section for Site 984, a single spliced record, representing an uninterrupted sedimentary sequence suitable for high-resolution sampling, was developed, as discussed in the "Explanatory Notes" chapter (this volume). Although between-hole correlations remained excellent down to 300 mcd, alignment of the core breaks at Cores 984B-26H, 984C-26H, and 984D-10H prevented continuation of the splice below 267 mcd. The tie points between the cores used to construct the splice are given in Table 3. The spliced GRAPE density, natural gamma radiation, and magnetic susceptibility data are shown in Figure 4.

LITHOSTRATIGRAPHY

The sediments at Site 984, like those of Site 983, are predominantly composed of rapidly accumulated fine-grained terrigenous particles. They have an average calcium carbonate content of 8%. Biocarbonate and, to a lesser extent, biosilica are present in variable minor amounts. Discrete ash layers occur throughout the upper sediment column, and pale to dark brown glass often occurs as a constituent of the silt- and sand-sized fractions. Authigenic iron sulfides, primarily in the form of disseminated pyrite, are also commonly present in minor amounts. The dominant lithologies include silty clay, clay, clayey nannofossil mixed sediment, and clay with variable amounts of nannofossils and silt. Nannofossil oozes with variable amounts of clay and sponge spicules also occur. As at Site 983, lithologic variation on decimeter to meter scales characterizes the sediment at this site, and is due to changes in the abundance of silt and biogenic materials relative to clay content. The range of variation in these components is smaller than in sediments of comparable age at Sites 980, 981, and 982.

The primary lithostratigraphic unit and subunits for the Site 984 sedimentary sequence are defined on the basis of data obtained from seven sources: (1) visual observation of color, (2) smear slide examination, (3) bulk calcium carbonate measurements, (4) spectral reflectance measurements, (5) magnetic susceptibility measurements, (6) natural gamma-ray measurements, and (7) X-ray diffraction analysis. No major lithologic boundaries occur within the 504 m of sediment recovered at this site. Changes in the spectral reflectance, the character of the magnetic susceptibility signal, and the occurrence or abundance of minor lithologies, interbedded within the dominant clays and silty clays, define boundaries which divide Unit I into four subunits. These divisions occur at 120, 165, and 279 mbsf. The shallowest boundary is recognized primarily in the spectral reflectance signal. It is characterized by a downcore decrease in the amplitude of the higher frequency (decimeter- to meter-scale) reflectance signal and an absence of the lower frequency reflectance signal (>10 m scale). Interbedded ash layers are common above this uppermost division. The boundary at 165 mbsf is recognized in visual examination of split cores and smear slides. It is characterized by the downcore absence of layers in which biocarbonate is predominant. Ash layers and dropstones are rare below this division. The deepest boundary is recognized by a downcore increase in sediment induration and an in-

Table 2. Site 984 composite depths.

Core, section	Length (cm)	Depth (mbsf)	Depth (mcd)	Offset (mcd – mbsf)
162-984A-				
1H-1	150	0.00	0.05	0.05
1H-2	150	1.50	1.55	0.05
1H-3	150	3.00	3.05	0.05
1H-4	42	4.50	4.55	0.05
1H-CC	17	4.92	4.97	0.05
2H-1	150	5.10	7.23	2.13
2H-2	150	6.60	8.73	2.13
2H-3	150	8.10	10.23	2.13
2H-4	150	9.60	11.73	2.13
2H-5	150	11.10	13.23	2.13
2H-6	59	12.60	14.73	2.13
2H-C	15	13.19	15.32	2.13
3H-1	150	14.60	16.83	2.23
3H-2	150	16.10	18.33	2.23
3H-3	150	17.60	19.83	2.23
3H-4	150	19.10	21.33	2.23
3H-5	150	20.60	22.83	2.23
3H-6	150	22.10	24.33	2.23
3H-7	55	23.60	25.83	2.23
3H-CC	18	24.15	26.38	2.23
4H-1	150	24.10	26.64	2.54
4H-2	150	25.60	28.14	2.54
4H-3	150	27.10	29.64	2.54
4H-4	150	28.60	31.14	2.54
4H-5	150	30.10	32.64	2.54
4H-6	150	31.60	34.14	2.54
4H-7	60	33.10	35.64	2.54
4H-CC	14	33.70	36.24	2.54
5H-1	150	33.60	37.35	3.75
5H-2	150	35.10	38.85	3.75
5H-3	150	36.60	40.35	3.75
5H-4	150	38.10	41.85	3.75
5H-5	150	39.60	43.35	3.75
5H-6	137	41.10	44.85	3.75
5H-CC	22	42.47	46.22	3.75
6H-1	150	43.10	47.44	4.34
6H-2	150	44.60	48.94	4.34
6H-3	150	46.10	50.44	4.34
6H-4	150	47.60	51.94	4.34
6H-5	150	49.10	53.44	4.34
6H-6	150	50.60	54.94	4.34
6H-7	51	52.10	56.44	4.34
6H-CC	25	52.61	56.95	4.34
7H-1	150	52.60	58.67	6.07
7H-2	150	54.10	60.17	6.07
7H-3	150	55.60	61.67	6.07
7H-4	150	57.10	63.17	6.07
7H-5	150	58.60	64.67	6.07
7H-6	150	60.10	66.17	6.07
7H-7	60	61.60	67.67	6.07
7H-CC	29	62.20	68.27	6.07
8H-1	150	62.10	68.90	6.80
8H-2	150	63.60	70.40	6.80
8H-3	150	65.10	71.90	6.80
8H-4	150	66.60	73.40	6.80
8H-5	150	68.10	74.90	6.80
8H-6	150	69.60	76.40	6.80
8H-7	66	71.10	77.90	6.80
8H-CC	23	71.76	78.56	6.80
9H-1	150	71.60	79.15	7.55
9H-2	150	73.10	80.65	7.55
9H-3	150	74.60	82.15	7.55
9H-4	150	76.10	83.65	7.55
9H-5	150	77.60	85.15	7.55
9H-6	150	79.10	86.65	7.55
9H-7	66	80.60	88.15	7.55
9H-CC	18	81.26	88.81	7.55
10H-1	150	81.10	89.21	8.11
10H-2	150	82.60	90.71	8.11
10H-3	150	84.10	92.21	8.11
10H-4	150	85.60	93.71	8.11
10H-5	150	87.10	95.21	8.11
10H-6	150	88.60	96.71	8.11
10H-7	74	90.10	98.21	8.11
10H-CC	22	90.84	98.95	8.11
11H-1	150	90.60	100.72	10.12
11H-2	150	92.10	102.22	10.12
11H-3	150	93.60	103.72	10.12
11H-4	150	95.10	105.22	10.12
11H-5	150	96.60	106.72	10.12
11H-6	150	98.10	108.22	10.12
11H-7	60	99.60	109.72	10.12
11H-CC	24	100.20	110.32	10.12
12H-1	150	100.10	109.99	9.89
12H-2	150	101.60	111.49	9.89
12H-3	150	103.10	112.99	9.89
12H-4	150	104.60	114.49	9.89
12H-5	150	106.10	115.99	9.89
12H-6	150	107.60	117.49	9.89
12H-7	80	109.10	118.99	9.89
12H-CC	16	109.90	119.79	9.89
13H-1	150	109.60	120.70	11.10
13H-2	150	111.10	122.20	11.10
13H-3	150	112.60	123.70	11.10
13H-4	150	114.10	125.20	11.10
13H-5	150	115.60	126.70	11.10
13H-6	150	117.10	128.20	11.10
13H-7	64	118.60	129.70	11.10
13H-CC	22	119.20	130.34	11.10
14H-1	150	119.10	131.44	12.34
14H-2	150	120.60	132.94	12.34
14H-3	150	122.10	134.44	12.34
14H-4	150	123.60	135.94	12.34
14H-5	150	125.10	137.44	12.34
14H-6	150	126.60	138.94	12.34
14H-7	66	128.10	140.44	12.34
14H-CC	26	128.80	141.10	12.34
15H-1	150	128.60	141.73	13.13
15H-2	150	130.10	143.23	13.13
15H-3	150	131.60	144.73	13.13
15H-4	150	133.10	146.23	13.13
15H-5	150	134.60	147.73	13.13
15H-6	150	136.10	149.23	13.13
15H-7	58	137.60	150.73	13.13
15H-CC	29	138.20	151.31	13.13
16H-1	150	138.10	151.95	13.85
16H-2	150	139.60	153.45	13.85
16H-3	150	141.10	154.95	13.85
16H-4	150	142.60	156.45	13.85
16H-5	150	144.10	157.95	13.85
16H-6	150	145.60	159.45	13.85
16H-7	61	147.10	160.95	13.85
16H-CC	29	147.71	161.56	13.85
17H-1	150	147.60	162.44	14.84
17H-2	150	149.10	163.94	14.84
17H-3	150	150.60	165.44	14.84
17H-4	150	152.10	166.94	14.84
17H-5	150	153.60	168.44	14.84
17H-6	150	155.10	169.94	14.84
17H-7	62	156.60	171.44	14.84
17H-CC	26	157.22	172.06	14.84
18H-1	150	157.10	173.17	16.07
18H-2	150	158.60	174.67	16.07
18H-3	150	160.10	176.17	16.07
18H-4	150	161.60	177.67	16.07
18H-5	150	163.10	179.17	16.07
18H-6	150	164.60	180.67	16.07
18H-7	58	166.10	182.17	16.07
18H-CC	26	166.68	182.75	16.07
19H-1	150	166.60	183.46	16.86
19H-2	150	168.10	184.96	16.86
19H-3	150	169.60	186.46	16.86
19H-4	150	171.10	187.96	16.86
19H-5	150	172.60	189.46	16.86
19H-6	150	174.10	190.96	16.86
19H-7	60	175.60	192.46	16.86
19H-CC	26	176.20	193.06	16.86
162-984B-				
1H-1	150	0.00	0.18	0.18
1H-2	150	1.50	1.68	0.18
1H-3	150	3.00	3.18	0.18
1H-4	150	4.50	4.68	0.18
1H-5	150	6.00	6.18	0.18
1H-6	78	7.50	7.68	0.18
1H-CC	15	8.28	8.46	0.18
2H-1	150	8.50	10.24	1.74
2H-2	150	10.00	11.74	1.74
2H-3	150	11.50	13.24	1.74
2H-4	150	13.00	14.74	1.74
2H-5	150	14.50	16.24	1.74
2H-6	150	16.00	17.74	1.74
2H-7	56	17.50	19.24	1.74
2H-CC	21	18.06	19.80	1.74
3H-1	150	18.00	21.07	3.07
3H-2	150	19.50	22.57	3.07
3H-3	150	21.00	24.07	3.07
3H-4	150	22.50	25.57	3.07
3H-5	150	24.00	27.07	3.07
3H-6	150	25.50	28.57	3.07
3H-7	67	27.00	30.07	3.07
3H-CC	14	27.67	30.74	3.07
4H-1	150	27.50	31.10	3.60
4H-2	150	29.00	32.60	3.60
4H-3	150	30.50	34.10	3.60
4H-4	150	32.00	35.60	3.60
4H-5	150	33.50	37.10	3.60

Table 2 (continued).

Core, section	Length (cm)	Depth (mbsf)	Depth (mcd)	Offset (mcd – mbsf)	Core, section	Length (cm)	Depth (mbsf)	Depth (mcd)	Offset (mcd – mbsf)
4H-6	150	35.00	38.60	3.60	15H-CC	36	141.59	153.77	12.18
4H-7	72	36.50	40.10	3.60	16H-1	150	141.50	154.53	13.03
4H-CC	14	37.22	40.82	3.60	16H-2	150	143.00	156.03	13.03
5H-1	150	37.00	41.39	4.39	16H-3	150	144.50	157.53	13.03
5H-2	150	38.50	42.89	4.39	16H-4	150	146.00	159.03	13.03
5H-3	150	40.00	44.39	4.39	16H-5	150	147.50	160.53	13.03
5H-4	150	41.50	45.89	4.39	16H-6	150	149.00	162.03	13.03
5H-5	150	43.00	47.39	4.39	16H-7	60	150.50	163.53	13.03
5H-6	150	44.50	48.89	4.39	16H-CC	24	151.10	164.13	13.03
5H-7	67	46.00	50.39	4.39	17H-1	150	151.00	164.83	13.83
5H-CC	34	46.67	51.06	4.39	17H-2	150	152.50	166.33	13.83
6H-1	150	46.50	51.06	4.56	17H-3	150	154.00	167.83	13.83
6H-2	150	48.00	52.56	4.56	17H-4	150	155.50	169.33	13.83
6H-3	150	49.50	54.06	4.56	17H-5	150	157.00	170.83	13.83
6H-4	150	51.00	55.56	4.56	17H-6	150	158.50	172.33	13.83
6H-5	150	52.50	57.06	4.56	17H-7	51	160.00	173.83	13.83
6H-6	150	54.00	58.56	4.56	17H-CC	8	160.51	174.34	13.83
6H-7	66	55.50	60.06	4.56	18H-1	150	160.50	175.15	14.65
6H-CC	15	56.16	60.72	4.56	18H-2	150	162.00	176.65	14.65
7H-1	150	56.00	60.98	4.98	18H-3	150	163.50	178.15	14.65
7H-2	150	57.50	62.48	4.98	18H-4	150	165.00	179.65	14.65
7H-3	150	59.00	63.98	4.98	18H-5	150	166.50	181.15	14.65
7H-4	150	60.50	65.48	4.98	18H-6	150	168.00	182.65	14.65
7H-5	150	62.00	66.98	4.98	18H-7	56	169.50	184.15	14.65
7H-6	150	63.50	68.48	4.98	18H-CC	23	170.06	184.71	14.65
7H-7	75	65.00	69.98	4.98	19H-1	150	170.00	186.29	16.29
7H-CC	36	65.75	70.73	4.98	19H-2	150	171.50	187.79	16.29
8H-1	150	65.50	70.98	5.48	19H-3	150	173.00	189.29	16.29
8H-2	150	67.00	72.48	5.48	19H-4	150	174.50	190.79	16.29
8H-3	150	68.50	73.98	5.48	19H-5	150	176.00	192.29	16.29
8H-4	150	70.00	75.48	5.48	19H-6	150	177.50	193.79	16.29
8H-5	150	71.50	76.98	5.48	19H-7	55	179.00	195.29	16.29
8H-6	150	73.00	78.48	5.48	19H-CC	2	179.55	195.84	16.29
8H-7	56	74.50	79.98	5.48	20H-1	150	179.50	195.33	15.83
8H-CC	42	75.06	80.54	5.48	20H-2	150	181.00	196.83	15.83
9H-1	150	75.00	81.42	6.42	20H-3	150	182.50	198.33	15.83
9H-2	150	76.50	82.92	6.42	20H-4	150	184.00	199.83	15.83
9H-3	150	78.00	84.42	6.42	20H-5	150	185.50	201.33	15.83
9H-4	150	79.50	85.92	6.42	20H-6	150	187.00	202.83	15.83
9H-5	150	81.00	87.42	6.42	20H-7	57	188.50	204.33	15.83
9H-6	150	82.50	88.92	6.42	20H-CC	12	189.07	204.90	15.83
9H-7	60	84.00	90.42	6.42	21H-1	150	189.00	207.40	18.40
9H-CC	36	84.60	91.02	6.42	21H-2	150	190.50	208.90	18.40
10H-1	150	84.50	91.92	7.42	21H-3	150	192.00	210.40	18.40
10H-2	150	86.00	93.42	7.42	21H-4	150	193.50	211.90	18.40
10H-3	150	87.50	94.92	7.42	21H-5	150	195.00	213.40	18.40
10H-4	150	89.00	96.42	7.42	21H-6	150	196.50	214.90	18.40
10H-5	150	90.50	97.92	7.42	21H-7	52	198.00	216.40	18.40
10H-6	150	92.00	99.42	7.42	21H-CC	10	198.52	216.92	18.40
10H-7	25	93.50	100.92	7.42	22H-1	150	198.50	217.30	18.80
10H-CC	33	93.75	101.17	7.42	22H-2	150	200.00	218.80	18.80
11H-1	150	94.00	101.86	7.86	22H-3	150	201.50	220.30	18.80
11H-2	150	95.50	103.36	7.86	22H-4	150	203.00	221.80	18.80
11H-3	150	97.00	104.86	7.86	22H-5	150	204.50	223.30	18.80
11H-4	150	98.50	106.36	7.86	22H-6	150	206.00	224.80	18.80
11H-5	150	100.00	107.86	7.86	22H-7	50	207.50	226.30	18.80
11H-6	150	101.50	109.36	7.86	22H-CC	4	208.00	226.80	18.80
11H-7	57	103.00	110.86	7.86	23H-1	150	208.00	228.08	20.08
11H-CC	35	103.57	111.43	7.86	23H-2	150	209.50	229.58	20.08
12H-1	150	103.50	111.96	8.46	23H-3	150	211.00	231.08	20.08
12H-2	150	105.00	113.46	8.46	23H-4	150	212.50	232.58	20.08
12H-3	150	106.50	114.96	8.46	23H-5	150	214.00	234.08	20.08
12H-4	150	108.00	116.46	8.46	23H-6	150	215.50	235.58	20.08
12H-5	150	109.50	117.96	8.46	23H-7	60	217.00	237.08	20.08
12H-6	150	111.00	119.46	8.46	23H-CC	11	217.60	237.68	20.08
12H-7	61	112.50	120.96	8.46	24H-1	150	217.50	237.77	20.27
12H-CC	38	113.11	121.57	8.46	24H-2	150	219.00	239.27	20.27
13H-1	150	113.00	123.27	10.27	24H-3	150	220.50	240.77	20.27
13H-2	150	114.50	124.77	10.27	24H-4	150	222.00	242.27	20.27
13H-3	150	116.00	126.27	10.27	24H-5	150	223.50	243.77	20.27
13H-4	150	117.50	127.77	10.27	24H-6	150	225.00	245.27	20.27
13H-5	150	119.00	129.27	10.27	24H-7	44	226.50	246.77	20.27
13H-6	150	120.50	130.77	10.27	24H-CC	2	226.94	247.21	20.27
13H-7	55	122.00	132.27	10.27	25H-1	150	227.00	248.27	21.27
13H-CC	37	122.55	132.82	10.27	25H-2	150	228.50	250.22	21.72
14H-1	150	122.50	133.37	10.87	25H-3	150	230.00	251.72	21.72
14H-2	150	124.00	134.87	10.87	25H-4	150	231.50	253.22	21.72
14H-3	150	125.50	136.37	10.87	25H-5	150	233.00	254.72	21.72
14H-4	150	127.00	137.87	10.87	25H-6	150	234.50	256.22	21.72
14H-5	150	128.50	139.37	10.87	25H-7	54	236.00	257.72	21.72
14H-6	130	130.00	140.87	10.87	25H-CC	17	236.54	258.26	21.72
14H-7	49	131.30	142.17	10.87	26H-1	150	236.50	259.09	22.59
15H-1	150	132.00	144.18	12.18	26H-2	150	238.00	260.59	22.59
15H-2	150	133.50	145.68	12.18	26H-3	150	239.50	262.09	22.59
15H-3	150	135.00	147.18	12.18	26H-4	150	241.00	263.59	22.59
15H-4	150	136.50	148.68	12.18	26H-5	150	242.50	265.09	22.59
15H-5	150	138.00	150.18	12.18	26H-6	150	244.00	266.59	22.59
15H-6	150	139.50	151.68	12.18	26H-7	60	245.50	268.09	22.59
15H-7	59	141.00	153.18	12.18	26H-CC	4	246.10	268.69	22.59

Table 2 (continued).

Core, section	Length (cm)	Depth (mbsf)	Depth (mcd)	Offset (mcd – mbsf)
27H-1	150	246.00	268.50	22.50
27H-2	150	247.50	270.00	22.50
27H-3	150	249.00	271.50	22.50
27H-4	150	250.50	273.00	22.50
27H-5	150	252.00	274.50	22.50
27H-6	150	253.50	276.00	22.50
27H-7	65	255.00	277.50	22.50
27H-CC	17	255.65	278.15	22.50
28H-1	150	255.50	278.00	22.50
28H-2	150	257.00	279.50	22.50
28H-3	150	258.50	281.00	22.50
28H-4	150	260.00	282.50	22.50
28H-5	150	261.50	284.00	22.50
28H-6	148	263.00	285.50	22.50
28H-CC	40	264.48	286.98	22.50
29H-1	150	265.00	287.50	22.50
29H-2	150	266.50	289.00	22.50
29H-3	150	268.00	290.50	22.50
29H-4	150	269.50	292.00	22.50
29H-5	150	271.00	293.50	22.50
29H-6	150	272.50	295.00	22.50
29H-7	28	274.00	296.50	22.50
29H-CC	4	274.28	296.78	22.50
30H-1	150	274.50	297.00	22.50
30H-2	150	276.00	298.50	22.50
30H-3	150	277.50	300.00	22.50
30H-4	150	279.00	301.50	22.50
30H-5	150	280.50	303.00	22.50
30H-6	150	282.00	304.50	22.50
30H-CC	2	283.50	306.00	22.50
31H-1	150	284.00	306.50	22.50
31H-2	150	285.50	308.00	22.50
31H-3	155	287.00	309.50	22.50
31H-4	150	288.55	311.05	22.50
31H-5	150	290.05	312.55	22.50
31H-6	150	291.55	314.05	22.50
31H-CC	41	293.05	315.55	22.50
32X-1	150	293.50	316.00	22.50
32X-2	150	295.00	317.50	22.50
32X-3	150	296.50	319.00	22.50
32X-4	150	298.00	320.50	22.50
32X-5	150	299.50	322.00	22.50
32X-6	150	301.00	323.50	22.50
32X-7	47	302.50	325.00	22.50
32X-CC	39	302.97	325.47	22.50
33X-1	150	301.80	324.30	22.50
33X-2	150	303.30	325.80	22.50
33X-3	150	304.80	327.30	22.50
33X-4	150	306.30	328.80	22.50
33X-5	150	307.80	330.30	22.50
33X-6	150	309.30	331.80	22.50
33X-7	47	310.80	333.30	22.50
33X-CC	42	311.27	333.77	22.50
34X-1	150	311.40	333.90	22.50
34X-2	150	312.90	335.40	22.50
34X-3	150	314.40	336.90	22.50
34X-4	150	315.90	338.40	22.50
34X-5	150	317.40	339.90	22.50
34X-6	110	318.90	341.40	22.50
34X-CC	43	320.00	342.50	22.50
35X-1	150	321.00	343.50	22.50
35X-2	150	322.50	345.00	22.50
35X-3	150	324.00	346.50	22.50
35X-4	150	325.50	348.00	22.50
35X-5	150	327.00	349.50	22.50
35X-6	150	328.50	351.00	22.50
35X-7	48	330.00	352.50	22.50
35X-CC	43	330.48	352.98	22.50
36X-1	150	330.60	353.10	22.50
36X-2	150	332.10	354.60	22.50
36X-3	150	333.60	356.10	22.50
36X-4	140	335.10	357.60	22.50
36X-CC	29	336.50	359.00	22.50
37X-1	150	340.20	362.70	22.50
37X-2	150	341.70	364.20	22.50
37X-3	150	343.20	365.70	22.50
37X-4	150	344.70	367.20	22.50
37X-5	150	346.20	368.70	22.50
37X-6	150	347.70	370.20	22.50
37X-7	44	349.20	371.70	22.50
37X-CC	38	349.64	372.14	22.50
38X-1	150	349.80	372.30	22.50
38X-2	150	351.30	373.80	22.50
38X-3	150	352.80	375.30	22.50
38X-4	150	354.30	376.80	22.50
38X-5	150	355.80	378.30	22.50
38X-6	150	357.30	379.80	22.50
38X-7	55	358.80	381.30	22.50
38X-CC	42	359.35	381.85	22.50
39X-1	150	359.40	381.90	22.50
39X-2	150	360.90	383.40	22.50
39X-3	150	362.40	384.90	22.50
39X-4	150	363.90	386.40	22.50
39X-5	150	365.40	387.90	22.50
39X-6	150	366.90	389.40	22.50
39X-7	47	368.40	390.90	22.50
39X-CC	23	368.87	391.37	22.50
40X-1	150	369.10	391.60	22.50
40X-2	150	370.60	393.10	22.50
40X-3	150	372.10	394.60	22.50
40X-4	150	373.60	396.10	22.50
40X-5	150	375.10	397.60	22.50
40X-6	150	376.60	399.10	22.50
40X-7	47	378.10	400.60	22.50
40X-CC	37	378.57	401.07	22.50
41X-1	150	378.70	401.20	22.50
41X-2	150	380.20	402.70	22.50
41X-3	150	381.70	404.20	22.50
41X-4	150	383.20	405.70	22.50
41X-5	150	384.70	407.20	22.50
41X-6	132	386.20	408.70	22.50
41X-CC	37	387.52	410.02	22.50
42X-1	150	388.40	410.90	22.50
42X-2	150	389.90	412.40	22.50
42X-3	150	391.40	413.90	22.50
42X-4	150	392.90	415.40	22.50
42X-5	150	394.40	416.90	22.50
42X-6	150	395.90	418.40	22.50
42X-7	46	397.40	419.90	22.50
42X-CC	24	397.86	420.36	22.50
43X-1	150	398.00	420.50	22.50
43X-2	150	399.50	422.00	22.50
43X-3	150	401.00	423.50	22.50
43X-4	150	402.50	425.00	22.50
43X-5	150	404.00	426.50	22.50
43X-6	150	405.50	428.00	22.50
43X-7	47	407.00	429.50	22.50
43X-CC	38	407.47	429.97	22.50
44X-1	150	407.60	430.10	22.50
44X-2	150	409.10	431.60	22.50
44X-3	150	410.60	433.10	22.50
44X-4	150	412.10	434.60	22.50
44X-5	150	413.60	436.10	22.50
44X-6	150	415.10	437.60	22.50
44X-7	43	416.60	439.10	22.50
44X-CC	36	417.03	439.53	22.50
45X-1	150	417.30	439.80	22.50
45X-2	150	418.80	441.30	22.50
45X-3	150	420.30	442.80	22.50
45X-4	150	421.80	444.30	22.50
45X-5	150	423.30	445.80	22.50
45X-6	150	424.80	447.30	22.50
45X-7	44	426.30	448.80	22.50
45X-CC	36	426.74	449.24	22.50
46X-1	150	426.90	449.40	22.50
46X-2	150	428.40	450.90	22.50
46X-3	150	429.90	452.40	22.50
46X-4	150	431.40	453.90	22.50
46X-5	150	432.90	455.40	22.50
46X-6	150	434.40	456.90	22.50
46X-7	36	435.90	458.40	22.50
46X-CC	27	436.26	458.76	22.50
47X-1	150	436.50	459.00	22.50
47X-2	150	438.00	460.50	22.50
47X-3	150	439.50	462.00	22.50
47X-4	150	441.00	463.50	22.50
47X-5	150	442.50	465.00	22.50
47X-6	150	444.00	466.50	22.50
47X-7	44	445.50	468.00	22.50
47X-CC	44	445.94	468.44	22.50
53X-1	150	494.10	516.60	22.50
53X-2	150	495.60	518.10	22.50
53X-3	150	497.10	519.60	22.50
53X-4	150	498.60	521.10	22.50
53X-5	20	500.10	522.60	22.50
53X-CC	46	500.30	522.80	22.50
162-984C-				
1H-1	150	0.00	0.00	0.00
1H-2	150	1.50	1.50	0.00
1H-3	150	3.00	3.00	0.00
1H-4	150	4.50	4.50	0.00
1H-5	63	6.00	6.00	0.00
1H-CC	16	6.63	6.63	0.00
2H-1	150	6.80	9.03	2.23
2H-2	150	8.30	10.53	2.23
2H-3	150	9.81	2.03	2.23
2H-4	150	11.30	13.53	2.23

Table 2 (continued).

Core, section	Length (cm)	Depth (mbsf)	Depth (mcd)	Offset (mcd – mbsf)
2H-5	150	12.80	15.03	2.23
2H-6	150	14.30	16.53	2.23
2H-7	48	15.80	18.03	2.23
2H-CC	19	16.28	18.51	2.23
3H-1	150	16.30	19.65	3.35
3H-2	150	17.80	21.15	3.35
3H-3	150	19.30	22.65	3.35
3H-4	150	20.80	24.15	3.35
3H-5	150	22.30	25.65	3.35
3H-6	150	23.80	27.15	3.35
3H-7	59	25.30	28.65	3.35
3H-CC	23	25.89	29.24	3.35
4H-1	150	25.80	30.27	4.47
4H-2	150	27.30	31.77	4.47
4H-3	150	28.80	33.27	4.47
4H-4	150	30.30	34.77	4.47
4H-5	150	31.80	36.27	4.47
4H-6	150	33.30	37.77	4.47
4H-7	63	34.80	39.27	4.47
4H-CC	16	35.43	39.90	4.47
5H-1	150	35.30	40.17	4.87
5H-2	150	36.80	41.67	4.87
5H-3	150	38.30	43.17	4.87
5H-4	150	39.80	44.67	4.87
5H-5	150	41.30	46.17	4.87
5H-6	150	42.80	47.67	4.87
5H-7	50	44.30	49.17	4.87
5H-CC	27	44.80	49.67	4.87
6H-1	150	44.80	51.07	6.27
6H-2	150	46.30	52.57	6.27
6H-3	150	47.80	54.07	6.27
6H-4	150	49.30	55.57	6.27
6H-5	150	50.80	57.07	6.27
6H-6	150	52.30	58.57	6.27
6H-7	64	53.80	60.07	6.27
6H-CC	20	54.44	60.71	6.27
7H-1	150	54.30	61.58	7.28
7H-2	150	55.80	63.08	7.28
7H-3	150	57.30	64.58	7.28
7H-4	150	58.80	66.08	7.28
7H-5	150	60.30	67.58	7.28
7H-6	150	61.80	69.08	7.28
7H-7	77	63.30	70.58	7.28
7H-CC	26	64.07	71.35	7.28
8H-1	150	63.80	71.84	8.04
8H-2	150	65.30	73.34	8.04
8H-3	150	66.80	74.84	8.04
8H-4	150	68.30	76.34	8.04
8H-5	150	69.80	77.84	8.04
8H-6	150	71.30	79.34	8.04
8H-7	70	72.80	80.84	8.04
8H-CC	26	73.50	81.54	8.04
9H-1	150	73.30	81.64	8.34
9H-2	150	74.80	83.14	8.34
9H-3	150	76.30	84.64	8.34
9H-4	150	77.80	86.14	8.34
9H-5	150	79.30	87.64	8.34
9H-6	150	80.80	89.14	8.34
9H-7	68	82.30	90.64	8.34
9H-CC	22	82.98	91.32	8.34
10H-1	150	82.80	92.53	9.73
10H-2	150	84.30	94.03	9.73
10H-3	150	85.80	95.53	9.73
10H-4	150	87.30	97.03	9.73
10H-5	150	88.80	98.53	9.73
10H-6	150	90.30	100.03	9.73
10H-7	72	91.80	101.53	9.73
10H-CC	25	92.52	102.25	9.73
11H-1	150	92.30	103.14	10.84
11H-2	150	93.80	104.64	10.84
11H-3	150	95.30	106.14	10.84
11H-4	150	96.80	107.64	10.84
11H-5	150	98.30	109.14	10.84
11H-6	150	99.80	110.64	10.84
11H-7	80	101.30	112.14	10.84
11H-CC	24	102.10	112.94	10.84
12H-1	150	101.80	112.17	10.37
12H-2	150	103.30	113.67	10.37
12H-3	150	104.80	115.17	10.37
12H-4	150	106.30	116.67	10.37
12H-5	150	107.80	118.17	10.37
12H-6	150	109.30	119.67	10.37
12H-7	72	110.80	121.17	10.37
12H-CC	20	111.52	121.89	10.37
13H-1	150	111.30	122.32	11.02
13H-2	150	112.80	123.82	11.02
13H-3	150	114.30	125.32	11.02
13H-4	150	115.80	126.82	11.02
13H-5	150	117.30	128.32	11.02
13H-6	150	118.80	129.82	11.02
13H-7	63	120.30	131.32	11.02
13H-CC	24	120.93	131.95	11.02
14H-1	150	120.80	132.45	11.65
14H-2	150	122.30	133.95	11.65
14H-3	150	123.80	135.45	11.65
14H-4	150	125.30	136.95	11.65
14H-5	150	126.80	138.45	11.65
14H-6	150	128.30	139.95	11.65
14H-7	71	129.80	141.45	11.65
14H-CC	25	130.51	142.16	11.65
15H-1	150	130.30	142.74	12.44
15H-2	150	131.80	144.24	12.44
15H-3	150	133.30	145.74	12.44
15H-4	150	134.80	147.24	12.44
15H-5	150	136.30	148.74	12.44
15H-6	150	137.80	150.24	12.44
15H-7	73	139.30	151.74	12.44
15H-CC	21	140.03	152.47	12.44
16H-1	150	139.80	152.77	12.97
16H-2	150	141.30	154.27	12.97
16H-3	150	142.80	155.77	12.97
16H-4	150	144.30	157.27	12.97
16H-5	150	145.80	158.77	12.97
16H-6	150	147.30	160.27	12.97
16H-7	63	148.80	161.77	12.97
16H-CC	25	149.43	162.4	12.97
17H-1	150	149.30	163.04	13.74
17H-2	150	150.80	164.54	13.74
17H-3	150	152.30	166.04	13.74
17H-4	150	153.80	167.54	13.74
17H-5	150	155.30	169.04	13.74
17H-6	150	156.80	170.54	13.74
17H-7	69	158.30	172.04	13.74
17H-CC	26	158.99	172.73	13.74
18H-1	150	158.80	173.25	14.45
18H-2	150	160.30	174.75	14.45
18H-3	150	161.80	176.25	14.45
18H-4	150	163.30	177.75	14.45
18H-5	150	164.80	179.25	14.45
18H-6	150	166.30	180.75	14.45
18H-7	64	167.80	182.25	14.45
18H-CC	25	168.44	182.89	14.45
19H-1	150	168.30	183.34	15.04
19H-2	150	169.80	184.84	15.04
19H-3	150	171.30	186.34	15.04
19H-4	150	172.80	187.84	15.04
19H-5	150	174.30	189.34	15.04
19H-6	150	175.80	190.84	15.04
19H-7	70	177.30	192.34	15.04
19H-CC	13	178.00	193.04	15.04
20H-1	150	177.80	194.61	16.81
20H-2	150	179.30	196.11	16.81
20H-3	150	180.80	197.61	16.81
20H-4	150	182.30	199.11	16.81
20H-5	150	183.80	200.61	16.81
20H-6	150	185.30	202.11	16.81
20H-7	62	186.80	203.61	16.81
20H-CC	28	187.42	204.23	16.81
21H-1	150	187.30	204.30	17.00
21H-2	150	188.80	205.80	17.00
21H-3	150	190.30	207.30	17.00
21H-4	150	191.80	208.80	17.00
21H-5	150	193.30	210.30	17.00
21H-6	150	194.80	211.80	17.00
21H-7	71	196.30	213.30	17.00
21H-CC	24	197.01	214.01	17.00
22H-1	150	196.80	214.68	17.88
22H-2	150	198.30	216.18	17.88
22H-3	150	199.80	217.68	17.88
22H-4	150	201.30	219.18	17.88
22H-5	150	202.80	220.68	17.88
22H-6	150	204.30	222.18	17.88
22H-7	58	205.80	223.68	17.88
23H-1	150	206.30	225.25	18.95
23H-2	150	207.80	226.75	18.95
23H-3	150	209.30	228.25	18.95
23H-4	150	210.80	229.75	18.95
23H-5	150	212.30	231.25	18.95
23H-6	150	213.80	232.75	18.95
23H-7	62	215.30	234.25	18.95
23H-CC	18	215.92	234.87	18.95
24H-1	150	215.80	235.64	19.84
24H-2	150	217.30	237.14	19.84
24H-3	150	218.80	238.64	19.84
24H-4	150	220.30	240.14	19.84
24H-5	150	221.80	241.64	19.84
24H-6	150	223.30	243.14	19.84
24H-7	57	224.80	244.64	19.84

Table 2 (continued).

Core, section	Length (cm)	Depth (mbsf)	Depth (mcd)	Offset (mcd – mbsf)
24H-CC	24	225.37	245.21	19.84
25H-1	150	225.30	246.83	21.53
25H-2	150	226.80	248.33	21.53
25H-3	150	228.30	249.83	21.53
25H-4	150	229.80	251.33	21.53
25H-5	150	231.30	252.83	21.53
25H-6	150	232.80	254.33	21.53
25H-7	51	234.30	255.83	21.53
25H-CC	21	234.81	256.34	21.53
26H-1	150	234.80	257.83	23.03
26H-2	150	236.30	259.33	23.03
26H-3	150	237.80	260.83	23.03
26H-4	150	239.30	262.33	23.03
26H-5	150	240.80	263.83	23.03
26H-6	150	242.30	265.33	23.03
26H-7	56	243.80	266.83	23.03
26H-CC	18	244.36	267.39	23.03
27H-1	150	244.30	267.33	23.03
27H-2	150	245.80	268.83	23.03
27H-3	150	247.30	270.33	23.03
27H-4	150	248.80	271.83	23.03
27H-5	150	250.30	273.33	23.03
27H-6	150	251.80	274.83	23.03
27H-7	43	253.30	276.33	23.03
27H-CC	16	253.73	276.76	23.03
28H-1	150	253.80	277.60	23.80
28H-2	150	255.30	279.10	23.80
28H-3	150	256.80	280.60	23.80
28H-4	150	258.30	282.10	23.80
28H-5	88	259.80	283.60	23.80
28H-6	150	260.68	284.48	23.80
28H-7	83	262.18	285.98	23.80
29H-1	150	263.30	287.53	24.23
29H-2	150	264.80	289.03	24.23
29H-3	150	266.30	290.53	24.23
29H-4	150	267.80	292.03	24.23
29H-5	150	269.30	293.53	24.23
29H-6	150	270.80	295.03	24.23
29H-7	45	272.30	296.53	24.23
29H-CC	20	272.75	296.98	24.23
30H-1	150	272.80	297.70	24.90
30H-2	82	274.30	299.20	24.90
30H-3	45	275.12	300.02	24.90
30H-4	150	275.57	300.47	24.90
30H-5	150	277.07	301.97	24.90
30H-6	38	278.57	303.47	24.90
31H-1	44	282.30	307.20	24.90
31H-2	150	282.74	307.64	24.90
31H-3	150	284.24	309.14	24.90
31H-4	87	285.74	310.64	24.90
31H-5	150	286.61	311.51	24.90
31H-6	150	288.11	313.01	24.90
31H-7	64	289.61	314.51	24.90
31H-CC	13	290.25	315.15	24.90
162-984D-				
1H-1	150	0.00	0.12	0.12
1H-2	150	1.50	1.62	0.12
1H-3	150	3.00	3.12	0.12
1H-4	150	4.50	4.62	0.12
1H-5	150	6.00	6.12	0.12
1H-6	71	7.50	7.62	0.12
1H-CC	16	8.21	8.33	0.12
2H-1	150	166.20	180.96	14.76
2H-2	150	167.70	182.46	14.76
2H-3	150	169.20	183.96	14.76
2H-4	150	170.70	185.46	14.76
2H-5	150	172.20	186.96	14.76
2H-6	150	173.70	188.46	14.76
2H-7	65	175.20	189.96	14.76
2H-CC	23	175.85	190.61	14.76
3H-1	145	175.70	191.52	15.82
3H-2	150	177.15	192.97	15.82
3H-3	150	178.65	194.47	15.82
3H-4	150	180.15	195.97	15.82
3H-5	150	181.65	197.47	15.82
3H-6	150	183.15	198.97	15.82
3H-7	67	184.65	200.47	15.82
3H-CC	32	185.32	201.14	15.82
4H-1	150	185.20	202.03	16.83
4H-2	150	186.70	203.53	16.83
4H-3	150	188.20	205.03	16.83
4H-4	150	189.70	206.53	16.83
4H-5	150	191.20	208.03	16.83
4H-6	150	192.70	209.53	16.83
4H-7	62	194.20	211.03	16.83
5H-1	150	194.70	212.05	17.35
5H-2	150	196.20	213.55	17.35
5H-3	150	197.70	215.05	17.35
5H-4	150	199.20	216.55	17.35
5H-5	150	200.70	218.05	17.35
5H-6	150	202.20	219.55	17.35
5H-7	59	203.70	221.05	17.35
5H-CC	21	204.29	221.64	17.35
6H-1	150	204.20	223.53	19.33
6H-2	150	205.70	225.03	19.33
6H-3	150	207.20	226.53	19.33
6H-4	150	208.70	228.03	19.33
6H-5	150	210.20	229.53	19.33
6H-6	150	211.70	231.03	19.33
6H-7	55	213.20	232.53	19.33
6H-CC	12	213.75	233.08	19.33
7H-1	150	213.70	234.17	20.47
7H-2	150	215.20	235.67	20.47
7H-3	150	216.70	237.17	20.47
7H-4	150	218.20	238.67	20.47
7H-5	150	219.70	240.17	20.47
7H-6	150	221.20	241.67	20.47
7H-7	59	222.70	243.17	20.47
8H-1	150	223.20	244.86	21.66
8H-2	150	224.70	246.36	21.66
8H-3	150	226.20	247.86	21.66
8H-4	150	227.70	249.36	21.66
8H-5	150	229.20	250.86	21.66
8H-6	150	230.70	252.36	21.66
8H-7	51	232.20	253.86	21.66
8H-CC	31	232.71	254.37	21.66
9H-1	150	232.70	256.12	23.42
9H-2	150	234.20	257.62	23.42
9H-3	150	235.70	259.12	23.42
9H-4	150	237.20	260.62	23.42
9H-5	150	238.70	262.12	23.42
9H-6	150	240.20	263.62	23.42
9H-7	68	241.70	265.12	23.42
10H-1	150	242.20	266.13	23.93
10H-2	150	243.70	267.63	23.93
10H-3	150	245.20	269.13	23.93
10H-4	150	246.70	270.63	23.93
10H-5	150	248.20	272.13	23.93
10H-6	150	249.70	273.63	23.93
10H-7	47	251.20	275.13	23.93
10H-CC	21	251.67	275.60	23.93
11H-1	150	251.70	275.90	24.20
11H-2	150	253.20	277.40	24.20
11H-3	150	254.70	278.90	24.20
11H-4	150	256.20	280.40	24.20
11H-5	150	257.70	281.90	24.20
11H-6	150	259.20	283.40	24.20
11H-7	53	260.70	284.90	24.20
12H-1	150	261.20	285.83	24.63
12H-2	150	262.70	287.33	24.63
12H-3	150	264.20	288.83	24.63
12H-4	150	265.70	290.33	24.63
12H-5	150	267.20	291.83	24.63
12H-6	130	268.70	293.33	24.63
12H-7	84	270.00	294.63	24.63

Note: Depths are from the top of each section.

crease in the wavelength of oscillations in the magnetic susceptibility signal.

Description of Lithostratigraphic Unit

Unit I

Intervals:
Cores 162-984A-1H through 19H
Cores 162 984B-1H through 53X
Cores 162 984C-1H through 31H
Cores 162 984D-1H through 12H
Age: Holocene to late Pliocene
Depth: 0 to 504 mbsf

Unit I consists of four 40- to 250-m-thick subunits. Subunit IA occupies the uppermost 120 mbsf of Unit I, Subunit IB extends from 120 to 165 mbsf, Subunit IC extends from 165 to 279 mbsf, and Subunit ID includes the lowermost sediments recovered, 279 to 504 mbsf

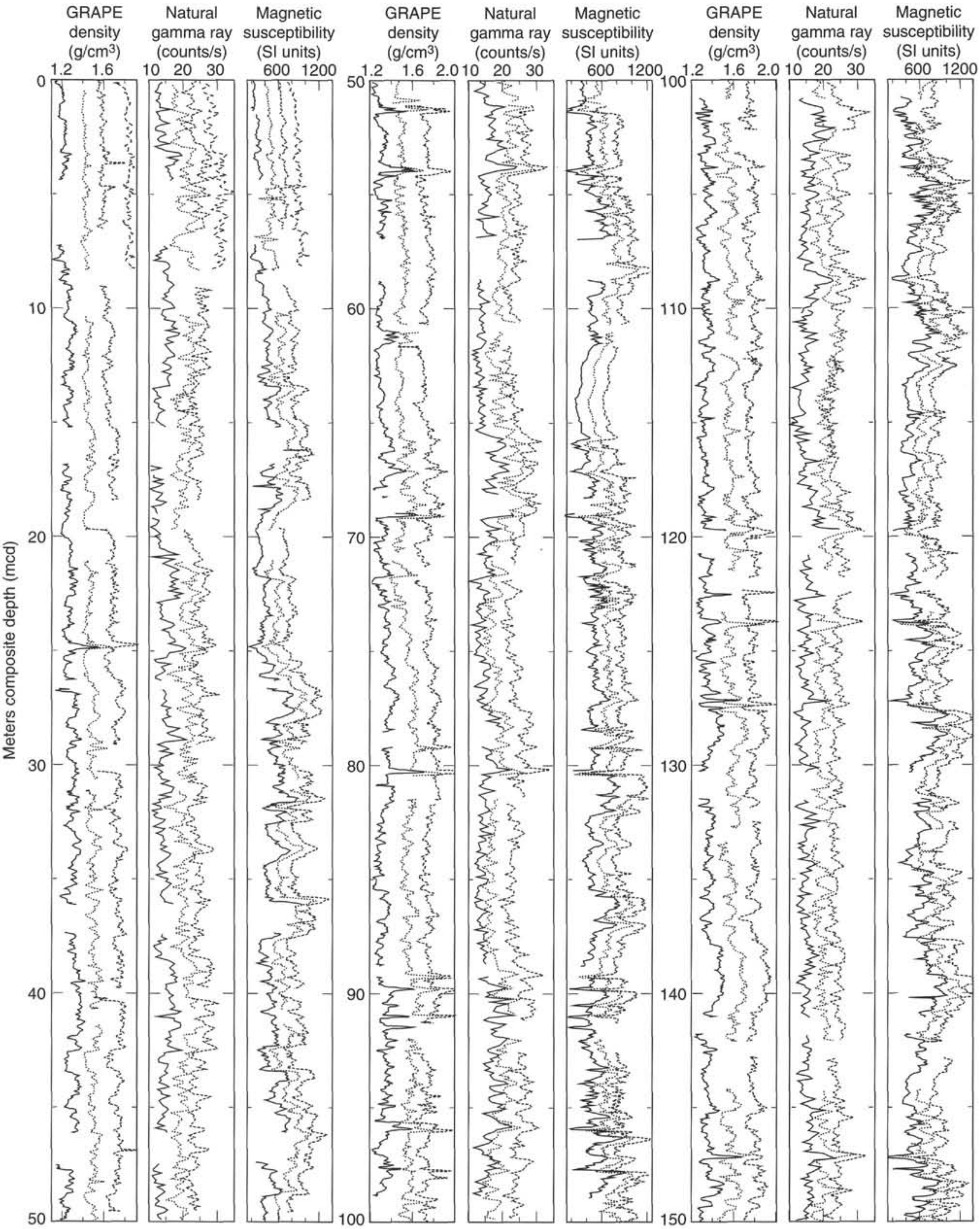

Figure 2. GRAPE density, natural gamma radiation, and magnetic susceptibility data from Site 984 on the mcd (meters composite depth) scale. Lines for Holes 984B (dotted), 984C (dashed), and 984D (long dashed) have been horizontally offset from line for Hole 984A (solid) for better display; therefore, values given on horizontal scale are the true values only for Hole 984A. (See also back pocket.)

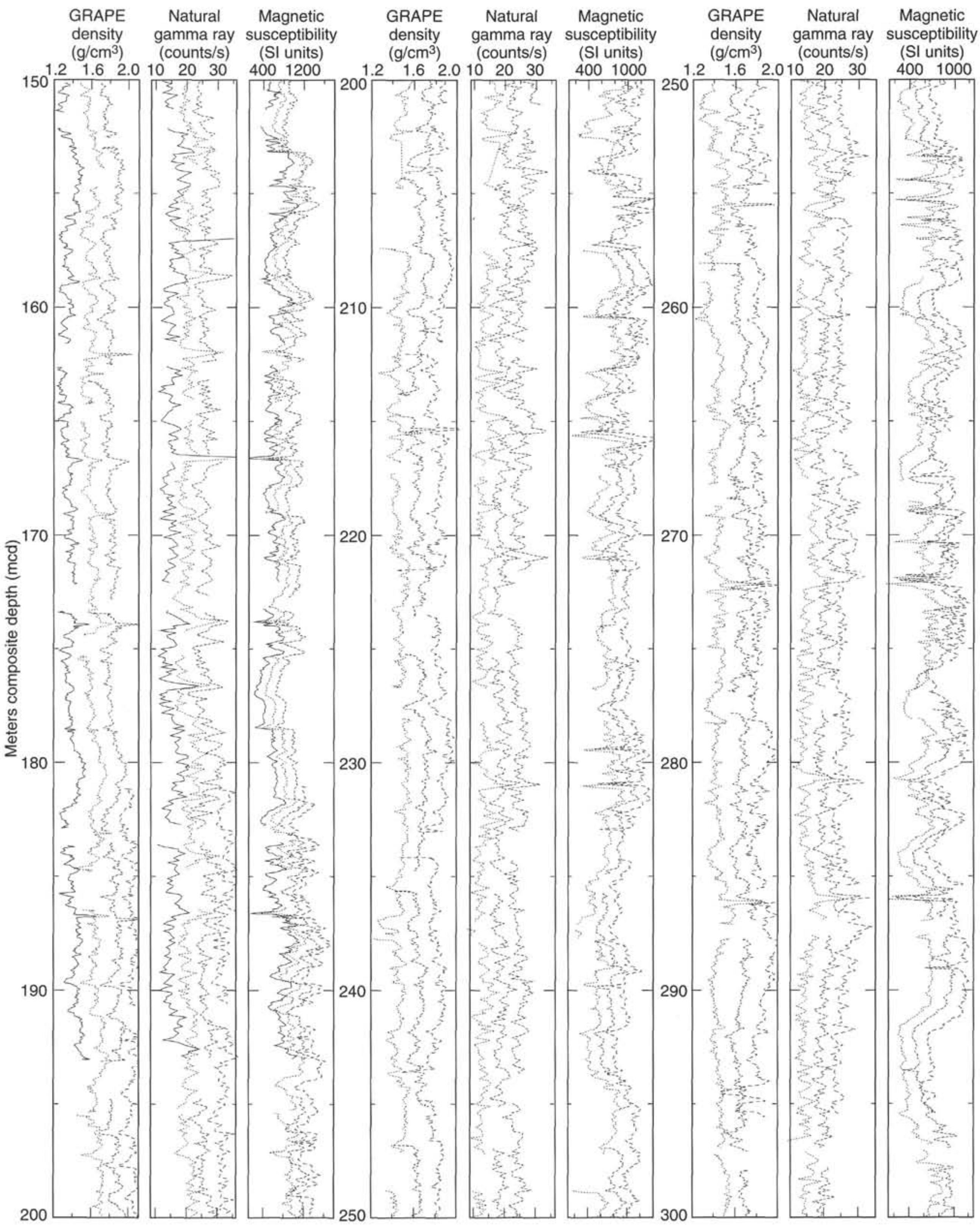

Figure 2 (continued).

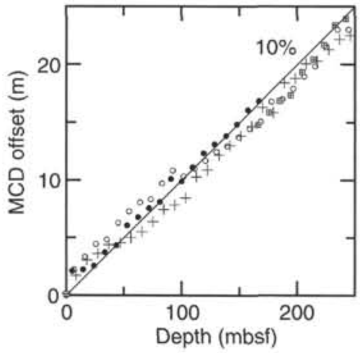

Figure 3. Depth offsets of the Site 984 meters composite depth scale relative to meters below seafloor depth, indicating the "growth" of the composite depth scale. Solid circles = Hole 984A, crosses = Hole 984B, open circles = Hole 984C, squares with crosses = Hole 984D.

Table 3. Site 984 splice tie points.

Hole, core, section (cm)	Depth (mbsf)	Depth (mcd)		Hole, core, section (cm)	Depth (mbsf)	Depth (mcd)
162-984-				162-984-		
C-1H-4, 41	4.91	4.91	tie to	D-1H-4, 29	4.79	4.91
D-1H-6, 62	8.12	8.24	tie to	A-2H-1, 101	6.11	8.24
A-2H-3, 4	8.14	10.27	tie to	C-2H-1, 124	8.04	10.27
C-2H-6, 95	15.24	17.47	tie to	A-3H-1, 64	15.24	17.47
A-3H-4, 43	19.53	21.76	tie to	C-3H-2, 61	18.41	21.76
C-3H-7, 11	25.40	28.75	tie to	A-4H-2, 61	26.21	28.75
A-4H-4, 14	28.74	31.28	tie to	C-4H-1, 101	26.81	31.28
C-4H-3, 46	29.26	33.73	tie to	B-4H-2, 113	30.13	33.73
B-4H-6, 53	35.53	39.13	tie to	A-5H-2, 29	35.38	39.13
A-5H-3, 52	37.12	40.87	tie to	C-5H-1, 70	36.00	40.87
C-5H-6, 71	43.51	48.38	tie to	A-6H-1, 95	44.04	48.38
A-6H-3, 134	47.44	51.78	tie to	C-6H-1, 71	45.51	51.78
C-6H-6, 119	53.49	59.76	tie to	A-7H-1, 110	53.69	59.76
A-7H-5, 98	59.57	65.64	tie to	C-7H-3, 107	58.36	65.64
C-7H-6, 145	63.25	70.53	tie to	A-8H-2, 13	63.73	70.53
A-8H-7, 50	71.60	78.40	tie to	C-8H-5, 56	70.36	78.40
C-8H-6, 79	72.09	80.13	tie to	A-9H-1, 98	72.58	80.13
A-9H-3, 26	74.85	82.40	tie to	C-9H-1, 76	74.06	82.40
C-9H-7, 11	82.41	90.75	tie to	A-10H-2, 5	82.64	90.75
A-10H-3, 110	85.19	93.30	tie to	C-10H-1, 77	83.57	93.30
C-10H-7, 4	91.84	101.57	tie to	A-11H-1, 85	91.45	101.57
A-11H-3, 19	93.79	103.91	tie to	C-11H-1, 77	93.07	103.91
C-11H-7, 14	101.44	112.28	tie to	A-12H-2, 79	102.39	112.28
A-12H-3, 37	103.47	113.36	tie to	C-12H-1, 119	102.99	113.36
C-12H-6, 146	110.76	121.13	tie to	A-13H-1, 44	110.03	121.13
A-13H-3, 23	112.82	123.92	tie to	C-13H-2, 10	112.90	123.92
C-13H-6, 58	119.38	130.40	tie to	B-13H-5, 113	120.13	130.40
B-13H-6, 122	121.72	131.99	tie to	A-14H-1, 55	119.65	131.99
A-14H-2, 82	121.42	133.76	tie to	C-14H-1, 131	122.11	133.76
C-14H-6, 88	129.18	140.83	tie to	B-14H-5, 146	129.96	140.83
B-14H-6, 121	131.21	142.08	tie to	A-15H-1, 35	128.95	142.08
A-15H-2, 19	130.29	143.42	tie to	C-15H-1, 68	130.98	143.42
C-15H-6, 76	138.56	151.00	tie to	B-15H-5, 82	138.82	151.00
B-15H-6, 143	140.93	153.11	tie to	C-16H-1, 34	140.14	153.11
C-16H-7, 23	149.03	162.00	tie to	B-16H-5, 146	148.96	161.99
B-16H-6, 122	150.21	163.24	tie to	A-17H-1, 80	148.40	163.24
A-17H-3, 83	151.43	166.27	tie to	C-17H-3, 23	152.53	166.27
C-17H-7, 16	158.46	172.20	tie to	B-17H-5, 137	158.37	172.20
B-17H-6, 118	159.68	173.51	tie to	C-18H-1, 26	159.06	173.51
C-18H-7, 43	168.23	182.68	tie to	D-2H-2, 22	167.92	182.68
D-2H-6, 101	174.71	189.47	tie to	C-19H-5, 14	174.43	189.47
C-19H-7, 34	177.64	192.68	tie to	D-3H-1, 116	176.86	192.68
D-3H-5, 65	182.29	198.11	tie to	C-20H-3, 50	181.30	198.11
C-20H-7, 5	186.85	203.66	tie to	D-4H-2, 14	186.83	203.66
D-4H-6, 82	193.52	210.35	tie to	C-21H-5, 5	193.35	210.35
C-21H-7, 32	196.62	213.62	tie to	D-5H-2, 7	196.27	213.62
D-5H-6, 122	203.41	220.76	tie to	B-22H-3, 46	201.96	220.76
B-22H-6, 70	206.70	225.50	tie to	D-6H-2, 47	206.17	225.50
D-6H-6, 113	212.82	232.15	tie to	B-23H-3, 107	212.07	232.15
B-23H-5, 118	215.18	235.26	tie to	D-7H-1, 110	214.79	235.26
D-7H-6, 43	221.63	242.10	tie to	B-24H-3, 133	221.83	242.10
B-24H-6, 35	225.35	245.62	tie to	D-8H-1, 76	223.96	245.62
D-8H-6, 67	231.37	253.03	tie to	B-25H-3, 131	231.31	253.03
B-25H-6, 89	235.38	257.10	tie to	D-9H-1, 98	233.68	257.10
D-9H-6, 52	240.72	264.14	tie to	C-26H-5, 31	241.11	264.14
C-26H-6, 110	243.40	266.43	tie to	B-26H-5, 134	243.80	266.40
B-53X-4, 143	500.02	522.52				

(Table 4; Fig. 5). Unit I sediments are dominated by variable amounts of clay, silt, and calcareous nannofossils. Specifically, the unit consists of alternating intervals of two primary sets of lithofacies: (1) dark gray, dark greenish gray, very dark gray, and very dark greenish gray clay, silty clay, clayey silt, nannofossil clay and clay with nannofossils, and (2) dark gray to very dark gray nannofossil clay mixed sediment, clayey nannofossil mixed sediment, and clayey mixed sediment with nannofossils. A third, more nannofossil-rich set of lithofacies is present but rare in Subunits IA, IB, and ID, and is absent from Subunit IC. It consists of light greenish gray, greenish gray, gray, dark gray, and dark greenish gray nannofossil ooze, nannofossil ooze with clay, nannofossil ooze with spicules, clayey nannofossil ooze, and clayey nannofossil ooze with spicules. XRD and smear slide analyses reveal that quartz and feldspar dominate the detrital silt component found in the silty dark gray clay layers, while tachylyte, rhyolitic ash, opaques, amphiboles, pyroxenes, micas, and inorganic calcite are lesser constituents.

The mean carbonate content of Unit I is 8.0%, as measured in Hole 984A. Values fluctuate from 0.4%, at 252.5 and 379.6 mbsf, to 32.2% at 107.8 mbsf. The relatively high-amplitude variations in carbonate content, which are at an approximately 10-m-scale, are superimposed on a longer trend of diminishing values downcore, which is most noticeable in Subunit IA (see "Organic Geochemistry" section, this chapter).

As was the case at Site 983, the spectral reflectance signal in Site 984 sediments is significantly diminished compared to previous sites, with few peaks above 20% (see "Lithostratigraphy" sections, "Sites 980/981" and "Site 982" chapters). Values for reflectance within the red band (650–700 nm) in Subunit IA decrease from an average of above 10% in the uppermost portion to an average near 5% at the base of the subunit, varying 2%–5% above and below the average reflectance. Within Subunit IB, the values remain near an average of 5% with few departures (e.g., 152–154 mbsf and 159–163 mbsf). Downcore through Subunit IC, the reflectance increases slightly and is variable from 4% to 8%. Uneven split surfaces due to induration within Subunit ID and the disturbance caused by XCB coring below Core 984B-31H precluded further measurements.

Dropstones are more common at Site 984 than at Site 983, averaging twice the number per hole. Twenty-eight dropstones greater than 1 cm and up to 5 cm in size were identified throughout Subunits IA and IB (Table 5). Several dropstones found in the uppermost portion of cores within Subunit IC were interpreted as fall-in. A single dropstone occurs in Section 984B-26H-5 of Subunit IC, and none occur in Subunit ID (see Fig. 5). As at previous sites, the dropstones typically occur in the darker colored clay-rich intervals. The distribution, texture, and composition of all dropstones greater than 1 cm in size are summarized in Table 5.

A number of thin to medium thickness ash layers (2–10 cm) and ash pods occur throughout Subunits IA and IB (see Figs. 5–7). They exhibit a range of shades from pale gray through brown to nearly black. Typically, the abundance of these ash beds decreases within Subunit IB and remains low throughout Subunits IC and ID.

There is no evidence of significant sediment disturbance by natural processes at Site 984. Visible bedding planes and color contacts are horizontal and parallel, with no erosional relief, although most are mottled by bioturbation (see Fig. 8). Bioturbation is ubiquitous throughout the cores from all four holes, and is characterized by discrete burrows, blurred transitions, and fine-scale mottling.

Interpretation

Sediments accumulating at Sites 983 and 984 represent two depocenters (Gardar and Bjorn drifts) associated with abyssal currents

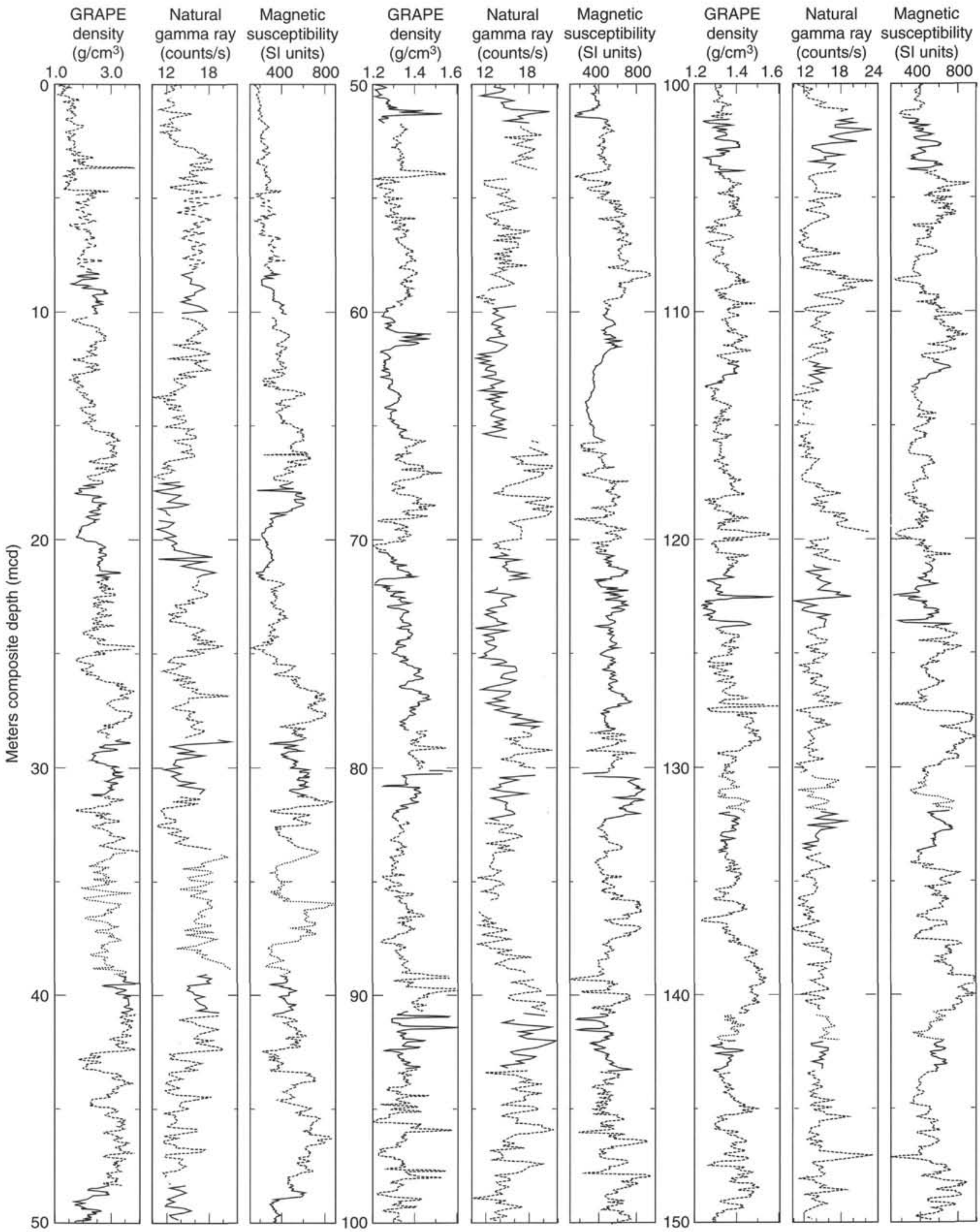

Figure 4. Spliced records of GRAPE density, natural gamma radiation, and magnetic susceptibility from Site 984. Tie points for forming the splice are given in Table 3. Holes are 984A (solid), 984B (dotted), 984C (dashed), and 984D (long dashed).

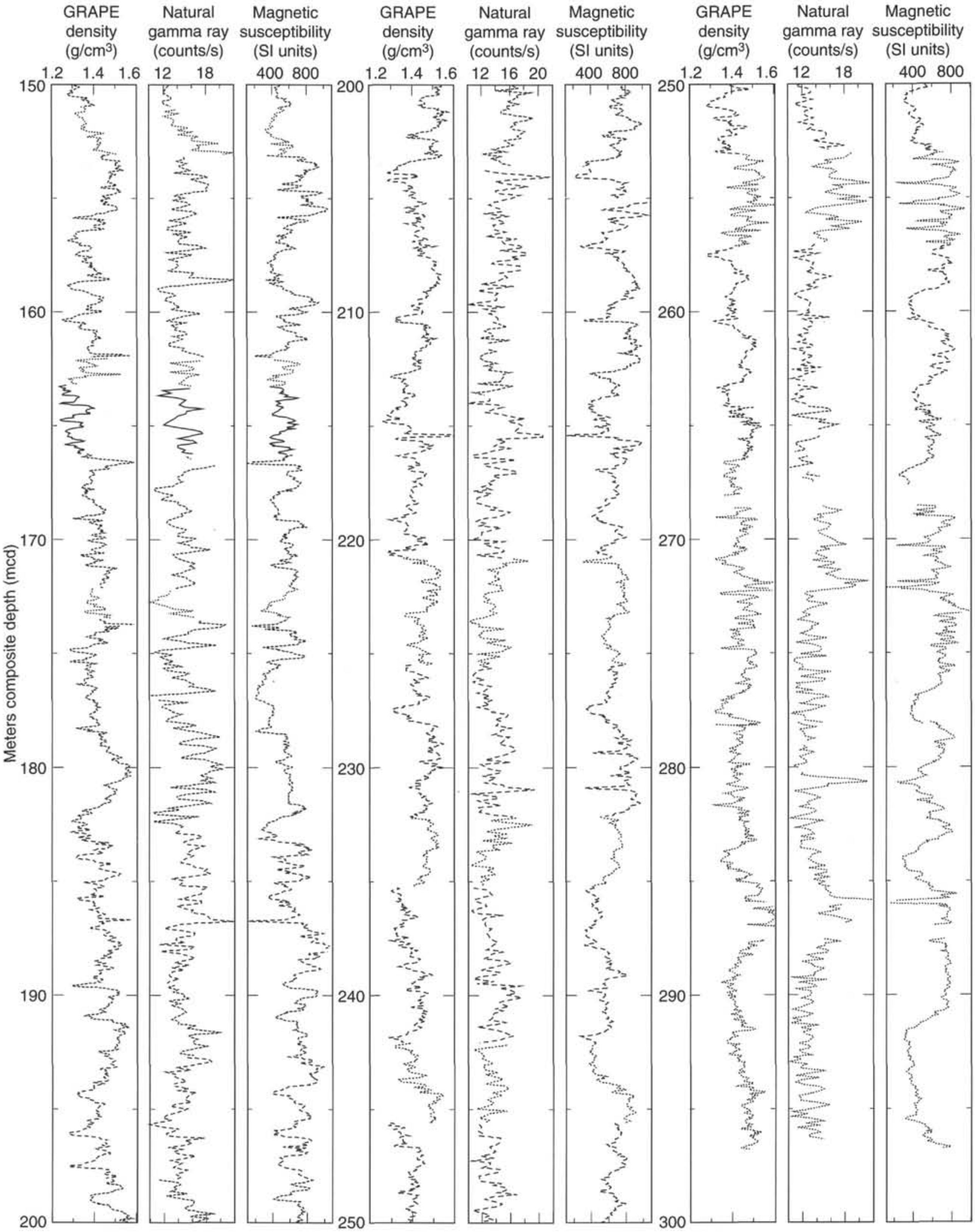

Figure 4 (continued).

Table 4. Summary table of sediment characteristics found in lithostratigraphic Unit I at Site 984.

Unit	Subunit	Depth (mbsf)	Thickness (m)	Age	Dominant lithologies/criteria
I		0–260.2	260.2	Pleist.–late Plio.	Cyclic (0.5 to 10 m) lithologic changes
	IA	0–120.0	120.0	Pleistocene	Clay, silty clay, clayey silt, clayey nannofossil mixed sediment nannofossil ooze, nannofossil clay/cyclic lithologic changes, terrigenous and biogenic components often nearly equal, variable color, abundant ash layers, dropstones
	IB	120.0–165.0	45.0	Pleistocene	Clay, silty clay, clayey silt, clayey nannofossil mixed sediment, nannofossil ooze, nannofossil clay/cyclic lithologic changes, terrigenous and biogenic components often nearly equal, invariant color, less common ash layers, dropstones
	IC	165.0–279.0	114.0	Pleist.–late Plio.	Clay, silty clay, clayey silt/cyclic lithologic changes, terrigenous components dominant, invariant color, rare ash layers, one dropstone
	ID	279.0–504.0	225.0	late Pliocene	Clay, silty clay, nannofossil clay/cyclic lithologic changes, terrigeneous and biogenic components sometimes nearly equal, invariant color, rare ash layers, no dropstones, indurated sediment, high-amplitude low-frequency magnetic susceptibility signal

flowing southwest along the eastern flank of Reykjanes Ridge (Davies and Laughton, 1972). There are, consequently, many similarities between the sediments recovered at the two sites. These include the predominance of fine-grained terrigenous particles, high sedimentation rates, cyclical interbedding of silty clay with layers containing calcareous microfossils, dark greenish gray color, low spectral reflectance, and both the strength and cyclicity of the magnetic susceptibility and natural gamma-ray signals.

Microfossil abundances at Site 984, as at Site 983, are apparently controlled by depositional processes rather than dissolution, and terrigenous sediment accumulation at both sites appears to be influenced more by deep-current sediment focusing than by ice rafting (see "Lithostratigraphy" section, "Site 983" chapter). Based on the lower carbonate content and the somewhat higher sedimentation rate during the last 1 Ma compared to Site 983 (see "Sedimentation Rates" section, this chapter), it appears that the accumulation rate of fine terrigenous material was enhanced at this site. Prior to 1 Ma the situation was reversed, and fine terrigenous accumulation was greater at Site 983 (see "Sedimentation Rates" section, this chapter).

The biogenic component of sediments at Site 984 consists primarily of calcareous nannofossils. Bulk carbonate values reach peaks near 30%, lower than the peak values for the same time interval at Sites 980, 981, 982, and 983. Higher sedimentation rates during the interval of peak carbonate deposition appear to account for the diminution relative to Site 983, thus implying similar productivity in the overlying waters and spatial variability in deep deposition. Carbonate content at Site 984 varies by an order of magnitude, yet the overall sedimentation rates do not appear to vary over such a range. This implies that variable carbonate input (productivity?) accounts for some, if not all, of the variation in carbonate content.

Spectral reflectance appears linked to the carbonate content even at low values, although values observed at this site fall on the portion of the curvilinear reflectance/carbonate relationship where spectral reflectance seems less sensitive to carbonate content (see Fig. 9). Measurements from the five North Atlantic sites (980–984) define a systematic relationship between spectral reflectance and sediment carbonate content. This relationship holds over a wide range of carbonate and reflectance values, which opens the possibility of using spectral reflectance as a carbonate proxy in similar sedimentary regimes. The curvilinear relationship between carbonate and reflectance indicates a nonlinear relationship between the two and/or the influence of other sediment components on the overall reflectance, particularly at the extremes of carbonate content.

While the sediments recovered at Sites 983 and 984 share the aforementioned similarities, there are notable differences. The more common occurrence of dropstones at Site 984 implies greater ice-rafted deposition due to iceberg trajectories and/or increased melting. The former explanation is likely, as Site 984 is farther north and closer to potential sources (e.g., Iceland) for the predominant basaltic dropstones.

Another difference between the two sites is the abundance of discrete ash layers in Subunits IA and IB at Site 984. The strong depositional gradient between the two sites implies that the ash was delivered by a mechanism other than the abyssal currents that greatly influence the terrigenous sediments. Direct air fall to the sea from discrete eruptions is one possibility, as is ice rafting by glacial or sea ice. Although both mechanisms might account for more abundant layers at the more proximal Site 984, direct air fall is the more likely explanation, as ice rafting would not easily explain the sharp basal contacts and normal grading observed within many of the beds.

BIOSTRATIGRAPHY

A continuous sequence of sediments ranging in age from middle Pliocene to Holocene (3.0 to 0 Ma) was recovered at Site 984, located on the eastern flank of the Reykjanes Ridge, at a shallower depth than Site 983. Calcareous nannofossils are the dominant fossil group at this site. However, all fossil groups exhibit variable abundance and preservation, possibly correlated to glacial/interglacial cyclicity. Biostratigraphic zonations for all microfossil groups are summarized in Figure 10.

Age information is consistent between all microfossil groups and indicates that the Site 984 sedimentary sequence is continuous, without significant hiatuses. Sedimentation rates were determined using magnetic polarity data combined with the biostratigraphic datums that are presented in Table 6. For a detailed discussion of sedimentation rates at Site 984, see the "Sedimentation Rates" section (this chapter).

Calcareous Nannofossils

Calcareous nannofossils are generally abundant and well preserved in the upper 200 m. Both the abundance and preservation deteriorate in the lower sequence. As at previous sites, all the standard Pleistocene nannofossil zones are recognizable at Site 984 (Table 6; Fig. 10). However, *Calcidiscus macintyrei* is rare and sporadic at Site 984. Its last occurrence in Sample 162-984B-22H-CC is significantly older than the first occurrence of *Gephyrocapsa* spp. A/B. Data available to date suggest that the northern boundary for the biostratigraphic application of the last occurrence of *C. macintyrei* lies south of Site 984.

The first occurrence of *Gephyrocapsa* spp. A/B between Samples 162-984B-20H-6, 35 cm, and 20H-7, 35 cm, can be used to approximate the Pliocene/Pleistocene boundary. This placement agrees with that suggested by the planktonic foraminiferal biostratigraphy (Fig. 10). No lower Pliocene nannofossils (e.g., *Reticulofenestra pseudoumbilicus* and *Sphenolithus* spp.) were found at Site 984, and *Pseudoemiliania lacunosa* is present down to the last core (162-984B-

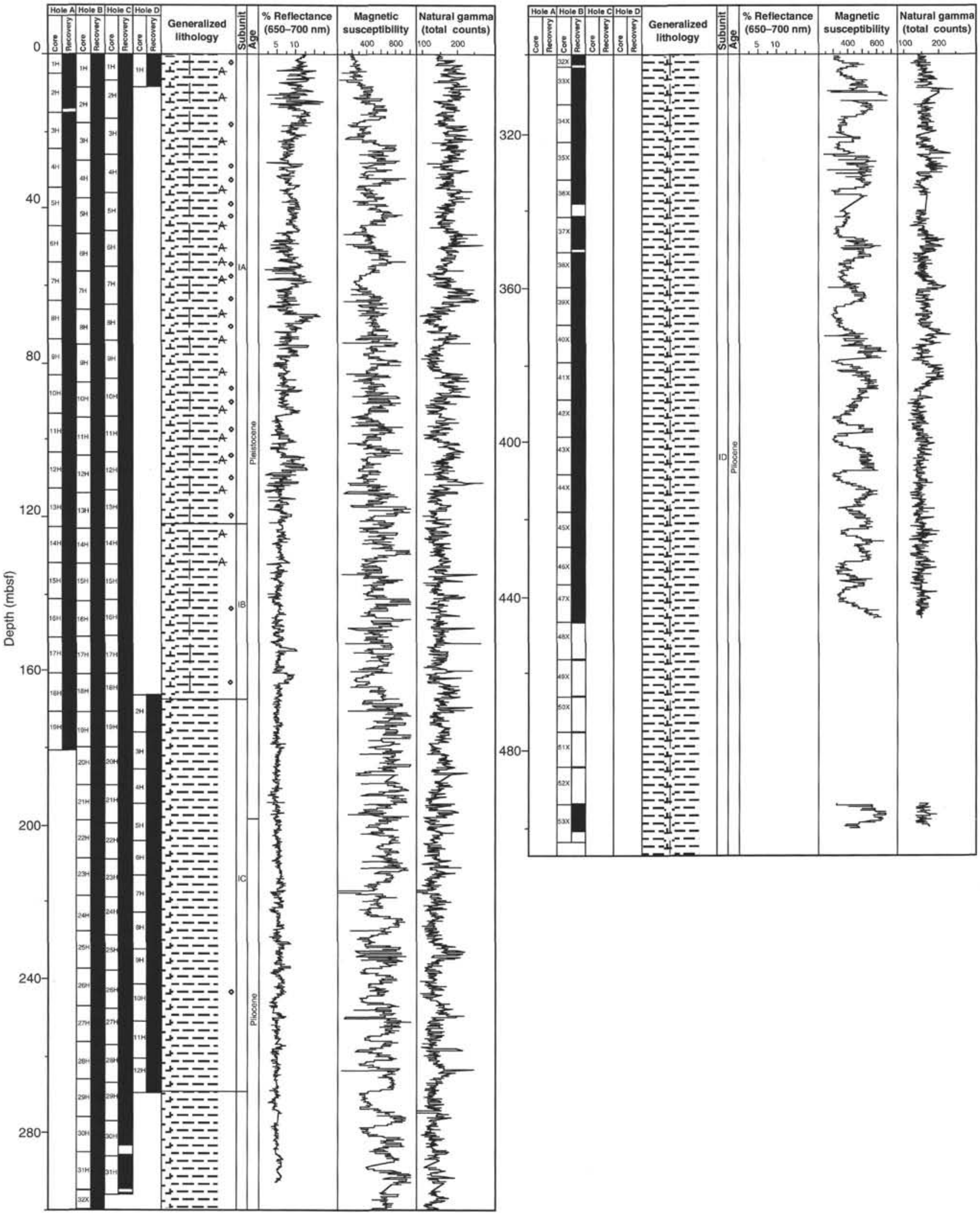

Figure 5. Core recovery, lithostratigraphy, age, spectral reflectance (red band), magnetic susceptibility, and natural gamma radiation of sediments recovered in Holes 984A through 984D. Locations of discrete ash layers (crossed A's) and dropstones (open diamonds) are shown in the column adjacent to the lithostratigraphy. Percentage reflectance, magnetic susceptibility, and natural gamma radiation records are from Hole 984B. (Key to symbols used in the "Generalized Lithology" column can be found in fig. 4, "Explanatory Notes" chapter, this volume.)

Table 5. Summary table of dropstones greater than 1 cm in length found in lithostratigraphic Unit I at Site 984.

Core, section	Top (cm)	Depth (mbsf)	Size (cm)	Composition	Shape
162-984B-					
2H-5	97	15.5	1.3	Basalt	Subrounded
7H-5	35	62.4	2.0	Quartzite	Angular
5H-3	40	40.4	1.1	Basalt	Angular
6H-1	10	46.6	1.5	Basalt	Subangular
7H-4	31	60.8	1.3	Sandstone	Subangular
7H-4	60	61.1	1.3	Basalt	Subrounded
7H-5	37	62.4	1.0	Basalt	Subangular
10H-1	50	85.0	3.0	Granite	Subrounded
10H-4	99	90.0	1.7	Vuggy granite (gray)	Subrounded
11H-3	38	97.4	2.7	Mudstone	Subrounded
11H-6	145	103.0	1.3	Basalt	Angular
12H-3	38	106.9	4.5	Crystalline	Subangular
12H-6	21	111.2	4.0	Scoria	Subrounded
13H-1	55	113.6	2.5	Crystalline	Subangular
13H-3	117	117.2	1.0	Basalt	Subangular
16H-4	137	147.4	2.8	Igneous	Subangular
18H-1	9	160.6	2.1	Black basalt	Subrounded
18H-6	31	168.3	4.5	Basalt	Subangular
19H-6	42.5	177.9	1.7	Light igneous (granite)	Rounded
162-984C-					
1H-3	68	3.7	4.4	Basalt	Rounded
3H-6	117	25.0	1.7	Sedimentary	Subrounded
4H-7	33	35.1	1.1	Basalt	Subrounded
5H-1	44	35.7	1.8	Black basalt	Rounded
5H-5	48	41.8	1.1	Basalt	Sunangular
5H-5	74	42.0	5.0	Gabbro	Subangular
7H-6	112	62.9	1.7	Sedimentary	Subangular
8H-6	90	72.2	1.0	Basalt	Subrounded

53X). This suggests an age younger than 3.7 Ma (late Pliocene) for the oldest sediment cored at Site 984.

Planktonic Foraminifers

Site 984 planktonic foraminifers are generally common from the top of the sequence to Sample 162-984B-23-CC, and rare to barren from Sample 162-984B-24H-CC to the bottom of the sequence (Sample 162-984B-53X-CC). Planktonic foraminifers are well preserved throughout the late Pliocene to Holocene. Assemblages in the upper part of the sequence include *Neogloboquadrina pachyderma* (sinistrally and dextrally coiling varieties), *Globigerina bulloides, Globorotalia inflata, Globorotalia scitula, Globigerinita glutinata,* and *Globigerina quinqueloba.* Assemblages in the lower part of the sequence include *Neogloboquadrina pachyderma* (dextrally coiling variety), *Globigerina bulloides, Globorotalia scitula,* and *Globigerina quinqueloba,* plus *Neogloboquadrina atlantica* in Sample 162-984B-36X-CC and below. Subpolar paleoenvironmental conditions are indicated throughout the sequence. The start of the acme zone of *N. pachyderma* (sinistrally coiling), between Samples 984B-21H-2, 35 cm, and 21H-4, 35 cm, falls just below the base of the Pleistocene (Fig. 10).

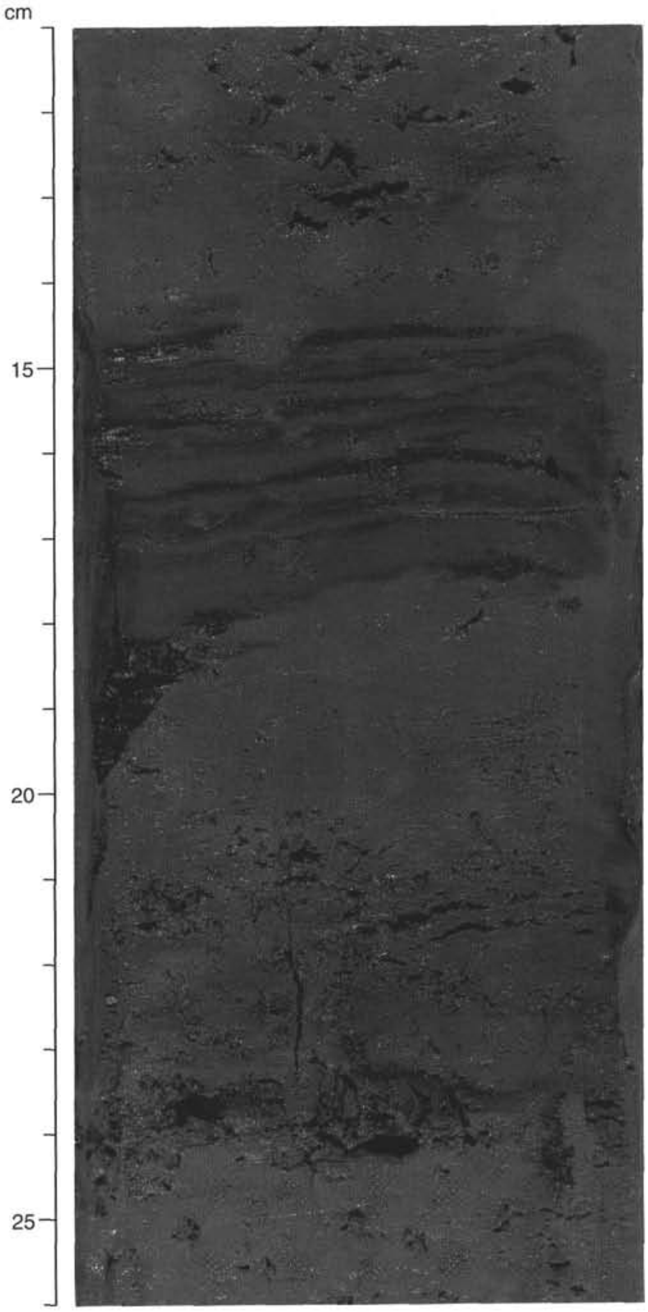

Figure 6. Photograph of a thinly bedded ash layer found in Section 162-984A-1H-4, 11–26 cm.

Benthic Foraminifers

Benthic foraminifers exhibit variable abundance and diversity at Site 984. Below about 200 m abundance decreases markedly, with occasional barren intervals throughout the upper Pliocene. Preservation is generally good throughout.

The mudline sample (162-984D-1H-1, 0–1 cm) was collected and stained with Rose Bengal solution for 8 hr. The sample contains a diverse, well-preserved fauna, with a number of stained specimens. These "live" specimens account for about 5% of the total benthic assemblage and include *Bolivina* spp., *Cassidulina teretis, Epistominella exigua, Nonionella* sp., *Reophax* sp., and *Uvigerina* sp.

The Pleistocene sequence at Site 984 is characterized by diverse assemblages dominated by *Cassidulina reniforme, Cassidulina teretis, Cibicidoides wuellerstorfi, Elphidium excavatum, Epistominella exigua, Melonis* spp., *Nonionella* spp., and *Pullenia* spp. Sporadic occurrence of *Elphidium excavatum* through the Pleistocene sequence (first occurrence in Sample 162-984A-11H-CC) may relate to downslope transportation and sediment reworking, since this is an ubiquitous and often highly abundant species on the upper slope and shelf. The last occurrence of *Stilostomella lepidula* in Sample 162-984A-12H-CC, at an interpolated age of about 0.9 Ma, is consistent with its last occurrence at Sites 980, 981, and 982. The late Pliocene assemblages at this site do not differ significantly from the overlying Pleistocene sequence, except that *Elphidium excavatum* is absent and

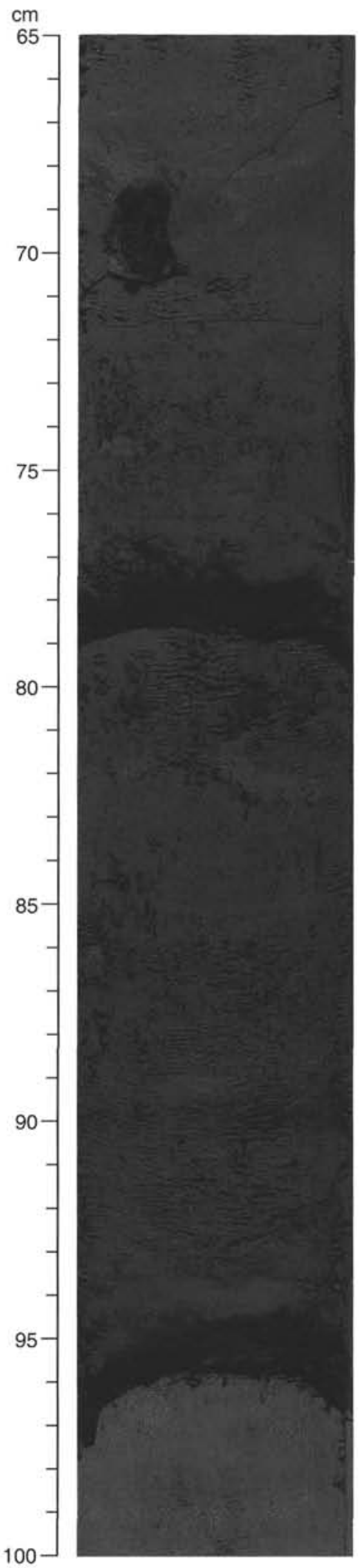

Figure 7. Photograph of two volcanic ash layers found in Section 162-984A-4H-4, 65–100 cm. Each layer is approximately 5 cm thick, has a sharp basal contact, and grades upward into the overlying sediment. The presumably horizontal bedding has been disturbed slightly to bow downward along the core liner.

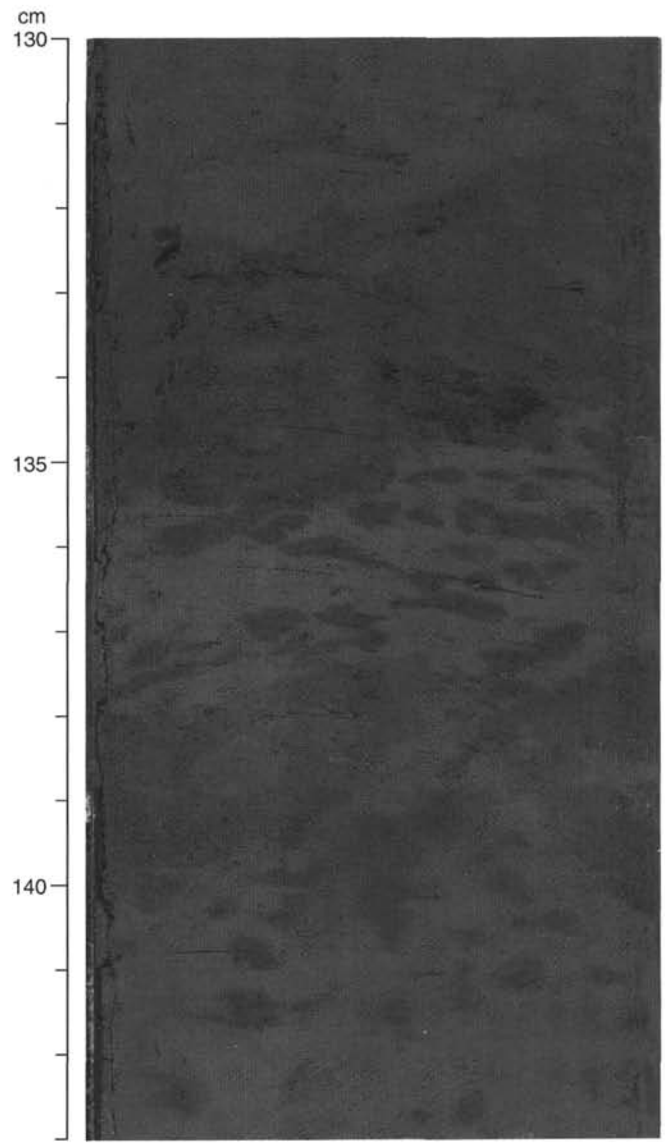

Figure 8. Photograph showing a typical bioturbated color contact in Site 984 sediments (Section 162-984A-12H-5, 130–143 cm).

infaunal taxa such as *Bolivina* spp. and *Globobulimina* spp. are more frequent. Lower abundances through this sequence may, in part, be due to carbonate dissolution, as evidenced by the occasional barren intervals below 200 m. In addition, higher sedimentation rates than the overlying Pleistocene (see "Sedimentation Rates" section, this chapter) may lead to sediment dilution of the benthic assemblages and also explain the increase in the relative abundance of infaunal taxa, particularly if higher sedimentation rates are associated with a higher flux of organic matter.

Diatoms

Diatoms at Site 984 vary in preservation and abundance. Diatom abundance in Samples 162-984A-1H-CC to 19H-CC ranges from barren to abundant, while preservation during this interval varies from poor to moderate. A barren interval of relatively long duration occurs between Samples 162-984B-24H-CC and 29H-CC. This interval encompasses the first occurrence of *Pseudoeunotia doliolus,* in the late Pliocene. Stratigraphically below this barren interval, diatom

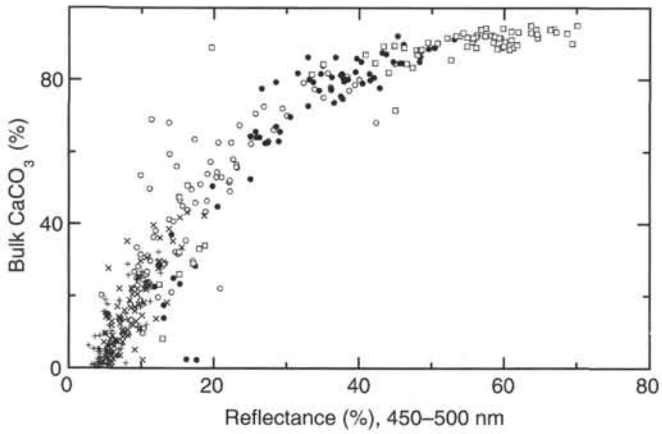

Figure 9. Bulk carbonate content and spectral reflectance (blue band, 450–500 nm) of sediments recovered at Sites 980 through 984. Open circles = Hole 980A; solid circles = Hole 981A; open squares = Hole 982B; × symbols = Hole 983A; and plus signs = Hole 984B.

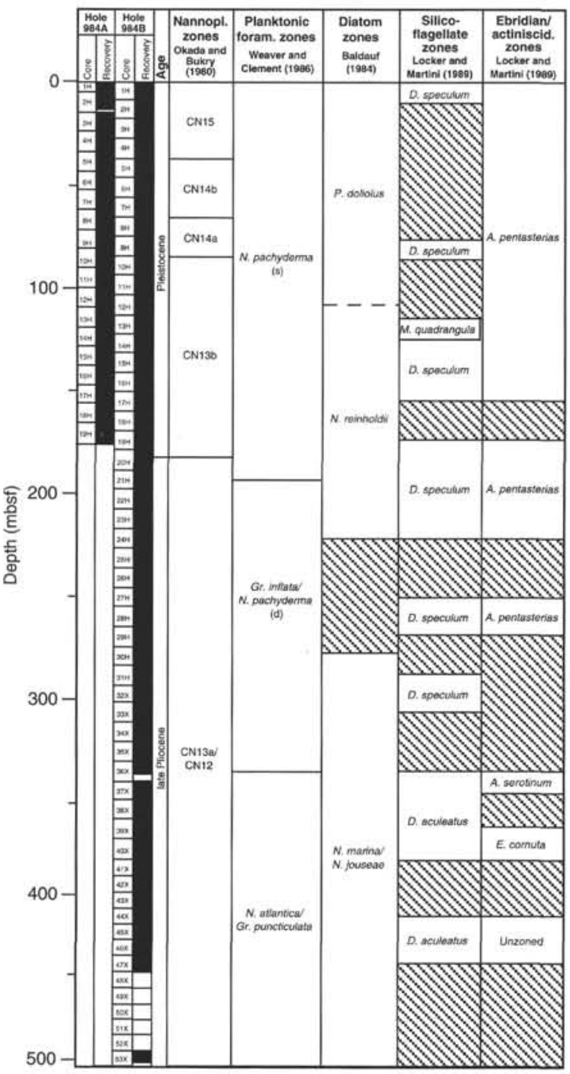

Figure 10. Biostratigraphic summary, Site 984. Hatched intervals indicate absence of fossils. The location of the Pliocene/Pleistocene boundary is based on nannofossil data.

Table 6. Depth range of biostratigraphic datums, Site 984.

Datum	Age (Ma)	Core, section, interval (cm)	Depth (mbsf)	Depth (mcd)
FO *E. huxleyi* (N)	0.26	984B-5H-1, 35–37 984B-5H-2, 35–37	37.35 38.85	41.74 43.24
LO *R. curvirostris* (D)	0.30	984A-5H-CC, 19–22 984A-6H-CC, 22–25	42.66 52.83	46.41 57.17
LO *P. lacunosa* (N)	0.46	984B- 7H-7, 35–37 8H-1, 35–37	65.35 65.85	70.33 71.33
FO *Gephyrocapsa* spp. C/D (N)	0.78	10H-3, 35–37 10H-4, 35–37	87.85 89.35	95.27 96.77
LO *Mesocena quadrangula* (S)	0.90	984A-12H-CC, 13–16 984A-13H-CC, 17–22	110.03 119.41	119.92 130.51
LO *Gephyrocapsa* spp. A/B (N)	1.23	984B-16H-5, 35–37 984B-16H-6, 35–37	147.85 149.35	160.88 162.38
FO *R. curvirostris* (D)	1.58	984A-17H-CC, 21–26 984A-18H-CC, 21–26	157.43 166.89	172.27 182.96
FO *R. curvirostris* (D)	1.58	984B- 18H-CC, 20–23 19H-CC, 0–2	170.26 179.55	184.91 195.84
FO *Gephyrocapsa* spp. A/B (N)	1.70	20H-6, 35–37 20H-7, 35–37	187.35 188.85	203.18 204.68
S, acme *N. pachyderma* s. (F)	1.80	21H-2, 35–37 21H-CC, 8–10	190.85 198.60	209.25 217.00
LO *N. atlantica* (F)	2.41	33X-1, 35–37 33X-2, 35–37	302.15 303.65	324.65 326.15
LO *E. cornuta* (E)	2.61	38X-CC, 39–42 39X-CC, 19–23	359.74 369.06	382.24 391.56

Notes: FO = first occurrence; LO = last occurrence; S = start. In parentheses: N = calcareous nannofossil, F = planktonic foraminifer, D = diatom, S = silicoflagellate, and E = ebridian.

abundances vary from few to barren, and samples contain only rare occurrences of species such as *Rhizosolenia praebergonii* and *Thalassiosira convexa.* Based on the occurrence of these species, the sediments below the barren interval are assigned to the *N. marina/N. jouseae* zones.

While samples below the barren interval are of indeterminate age, samples above belong to the *Nitzschia reinholdii* and *Pseudoeunotia doliolus* zones. Due to possible cold-water influences, as well as the variable abundance of diatoms, the species *Nitzschia reinholdii* is sporadic in occurrence. This makes the exact location of the boundary between the *Pseudoeunotia doliolus* and *Nitzschia reinholdii* zones impossible to place.

Siliceous Flagellates

Siliceous flagellates (including silicoflagellates, ebridians, and actiniscidians) display scattered occurrences downsection in Holes 984A and 984B. The abundance of these microfossils range from trace to common, the preservation from good to poor.

Silicoflagellates

Samples 162-984A-1H-CC to 984B-32X-CC are assigned to the *Distephanus speculum* Zone. Also in this high northern site, the upper lower Pleistocene *Mesocena quadrangula* Subzone was identified in Sample 162-984A-13H-CC. Relatively warm surface water is marked by *M. quadrangula* and by several *Dictyocha* species, such as *D. hessii, D.* cf. *lingi,* and *D. perlaevis.* In Samples 162-984B-36X-CC to 47X-CC the *Distephanus aculeatus* Zone is indicated by scattered occurrences of *Distephanus lingi* and *D. aculeatus.*

Ebridians and Actiniscidians

Between Samples 162-984A-2H-CC and 984B-28H-CC the *Actiniscus pentasterias* Zone is present. Below a long barren interval, the *Ammodochium serotinum* Zone is found in Sample 162-984B-36X-CC and the *Ebriopsis cornuta* Zone in Samples 162-984B-39X-CC and 40X-CC. The upper boundaries of both zones, 2.00 and 2.61 Ma, respectively, are obscured by barren intervals. Samples 162-984B-44X-CC to 47X-CC remain unzoned, since no diagnostic ebridian/actiniscidian species are present. Below, an interval follows that has no recovery or is barren.

PALEOMAGNETISM

At Site 984, archive halves of Holes 984A, 984B, 984C, and 984D were measured using the pass-through cryogenic magnetometer with a 5-cm measurement interval. Below about 250 mbsf in Holes 984B, 984C, and 984D, the magnetic measurements became incoherent in conjunction with an abrupt increase in visible drilling disturbance close to the base of the APC section. Demagnetization was carried out at peak alternating fields of 25 mT for all core sections. Additional demagnetization steps at 30 mT were carried out on some core sections, as time allowed (Table 7). The ubiquitous drilling-induced remanence is steeply inclined downward, and therefore mimics a normal-polarity geomagnetic field which may mask reversed-polarity intervals. This magnetic overprint can have relatively high coercivity and is not always fully removed at peak demagnetization fields of 30 mT (Fig. 11), the largest demagnetization field available in conjunction with the pass-through cryogenic magnetometer. The upper 25%–50% of Section 1 of most cores appears particularly susceptible to the high coercivity (drill-string) remagnetization, which is not always removed at peak alternating fields of 25 or 30 mT.

At the 25 mT demagnetization level, magnetization intensities fluctuate around 175 mA/m. Large variations in magnetic intensity are observed close to polarity reversals, where intensities often decrease to about 10 mA/m, and in the numerous ash layers, where intensities can reach 700 mA/m.

The Brunhes/Matuyama boundary and the Jaramillo, Olduvai, and Reunion Subchrons are well defined in Holes 984A, 984B, and 984C. The Olduvai and Reunion Subchrons are well defined in Hole 984D (Fig. 12). Sub-bottom depths of polarity chron boundaries are given in Table 8. A thin interval within the Brunhes Chron of low negative inclinations, close to 25 mbsf (Fig. 12), occurs in Holes 984A, 984B, and 984C, and may represent a magnetic excursion within the Brunhes Chron. Thin intervals of low positive inclination within the Matuyama Chron, some of which are present in all three holes (for example, close to 140 mbsf and near 165 mbsf), may represent magnetic events within the Matuyama Chron or intervals in which the steep downward drill-string remagnetization has not been completely removed.

As for Site 983, the high fidelity of the magnetic polarity stratigraphy and the high sedimentation rates bode well for the possibility of obtaining high-resolution polarity transition records. Transitional directions are recorded over 50–200 cm of core at most polarity zone boundaries, although some may be artifacts of the NRM acquisition process.

Table 7. Summary of pass-through cryogenic magnetometer measurements at Site 984.

Measurement	Core sections
	162-984A-
25 mT	1H-1 through 19H-7
30 mT	11H-3, 11H-5, 18H-5, 19H-7
	162-984B-
25 mT	1H-1 through 31H-6
30 mT	3H-6
	162-984C-
25 mT	1H-1 through 29H-4
30 mT	24H-5, 25H-4, 25H-6, 26H-1, 26H-4, 26H-6, 26H-7, 27H-2, 28H-5, 29H-1
	162-984D-
25 mT	1H-2 through 11H-6
30 mT	3H-1, 4H-1, 5H-1, 7H-3, 7H-4, 7H-6, 8H-5, 10H-3

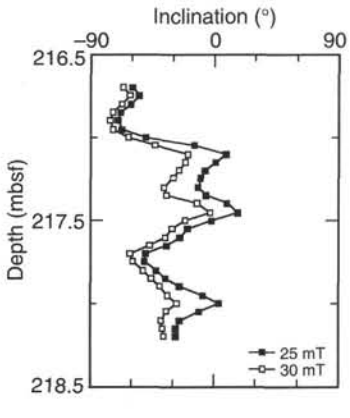

Figure 11. Inclination of the magnetization vector vs. depth (mbsf) for Section 984D-7H-3 after AF demagnetization at peak fields of 25 and 30 mT. The section lies in a reversed-polarity zone and is affected by a steeply inclined downward magnetic overprint.

SEDIMENTATION RATES

A sedimentary section 504 m thick was recovered at Site 984, extending from the Pliocene to the Holocene. Sedimentation rate reconstructions were based on magnetic polarity events from all four holes and calcareous nannofossil datums from Hole 984B (see "Paleomagnetism" and "Biostratigraphy" sections, this chapter). The Site 984 composite depth section (see "Composite Depths" section, this chapter) was used to relate events recorded in multiple holes to a common depth scale. To facilitate comparison between sites, sedimentation rates were estimated from age vs. depth plots (Fig. 13) by drawing straight-line segments (uniform sedimentation rate) between selected datums.

Sedimentation rates, calculated for both the meters below seafloor (mbsf) depth scale and the meters composite depth (mcd) depth scale, were relatively high, as expected. Figure 14 presents sedimentation rates as a function of age and composite depth. Magnetic polarity age control points included are the Brunhes/Matuyama Chron boundary and the Jaramillo, Olduvai, and Reunion Subchrons. Although sedimentation rates in the Jaramillo Subchron are very high relative to surrounding time intervals (145 mbsf/m.y., 163 mcd/m.y.), the depth of this event is well constrained in all three holes, implying that this is not a time scale artifact. The Matuyama/Gauss Chron boundary could not be reliably determined owing to disturbed intervals. Calcareous nannofossil datums are the FO of *Emilianii huxleyi* at 0.26 Ma, the LO of *Pseudoemilianii lacunosa* at 0.46 Ma, and the LO of *Gephyrocapsa* spp. A/B at 1.23 Ma. These datums are considered synchronous from tropical through temperate zones (see "Biostratigraphy" section, "Explanatory Notes" chapter, this volume). The age of the base of the section is unknown, although it is younger than the FO of *Pseudoemilianii lacunosa* at 3.70 Ma. Thus, sedimentation rates below the top of the Reunion Subchron at 241.40 mbsf (264.17 mcd) are at least 168 m/m.y. (Fig. 14).

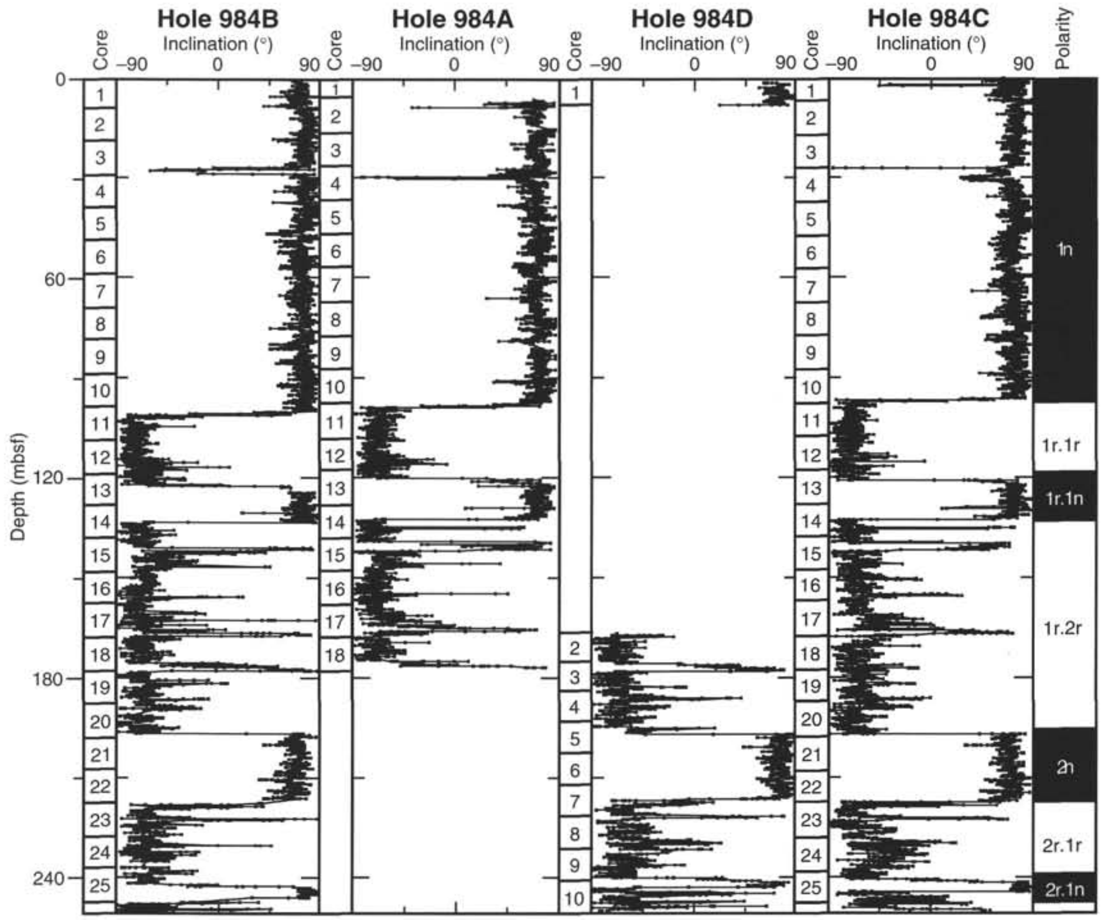

Figure 12. Inclination of the magnetization vector vs. depth (mbsf) for Holes 984A through 984D after AF demagnetization at peak fields of 25 mT.

Table 8. Preliminary positions of polarity chron boundaries at Site 984.

Core, section, interval (cm)	Depth (mbsf)	Interpreted boundary	Age (Ma)	Comments
162-984A-				
11H-5, 120	97.80	Brunhes/Matuyama	0.78	
14H-1, 15	119.25	Jaramillo (top)	0.99	
15H-3, 5	131.65	Jaramillo (bottom)	1.07	
162-984B-				
11H-5, 20	100.20	Brunhes/Matuyama	0.78	
13H-6, 120	121.70	Jaramillo (top)	0.99	
15H-1, 50	132.50	Jaramillo (bottom)	1.07	
21H-5, 90	195.90	Olduvai (top)	1.77	
24H-4, 25	222.25	Olduvai (bottom)	1.95	
26H-4, 85	241.85	Reunion (top)	2.14	
27H-1, 45	246.45	Reunion (bottom)	2.15	
162-984C-				
11H-3, 140	96.70	Brunhes/Matuyama	0.78	
13H-7, 40	120.70	Jaramillo (top)	0.99	
15H-2, 60	132.40	Jaramillo (bottom)	1.07	
22H-1, 0	196.80	Olduvai (top)	1.77	Core break
24H-1, 145	217.25	Olduvai (bottom)	1.95	
26H-5, 15	240.95	Reunion (top)	2.14	
27H-1, 0	244.30	Reunion (bottom)	2.15	Core break
162-984D-				
5H-2, 60	196.80	Olduvai (top)	1.77	
7H-2, 140	216.60	Olduvai (bottom)	1.95	
9H-5, 150	240.20	Reunion (top)	2.14	Section break
10H-1, 70	244.90	Reunion (bottom)	2.15	

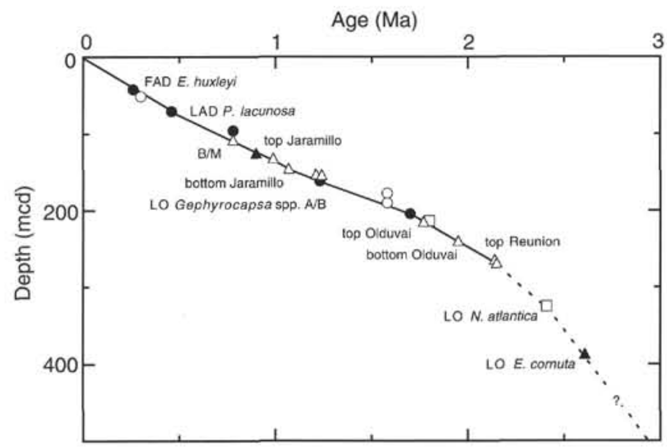

Figure 13. Site 984 age vs. depth (mcd) curve based on integrated magnetostratigraphic and biostratigraphic datums. Solid circles = nannofossils; open circles = diatoms; open squares = foraminifers; solid triangles = siliceous flagellates; open triangles = magnetostratigraphic datums. B/M = Brunhes/Matuyama Chron boundary.

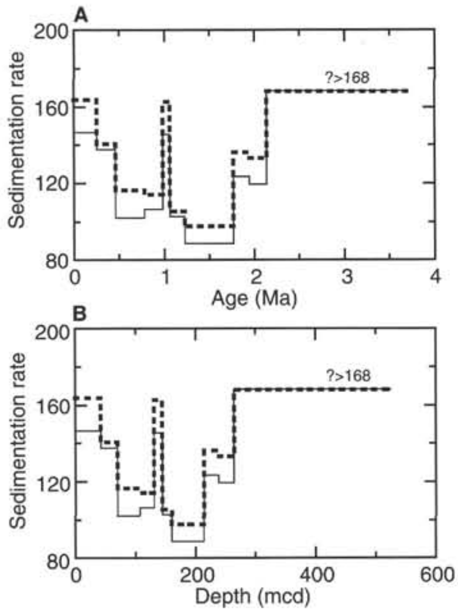

Figure 14. Site 984 sedimentation rates vs. age (**A**) and vs. composite depth (**B**). Solid lines indicate rates in mbsf/m.y.; dashed lines indicate rates in mcd/m.y.

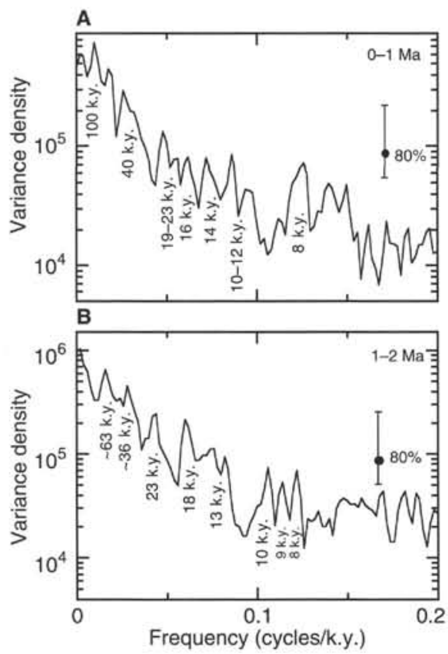

Figure 15. Power spectra of Site 984 magnetic susceptibility using the age control points given in Table 9. **A.** 0–1 Ma. **B.** 1–2 Ma. The susceptibility record was interpolated to an average sampling interval of 1 k.y. and linearly detrended. The spectra were calculated using the Blackman-Tukey lagged autocovariance method, and were smoothed using 300 lags of the autocovariance function, for a frequency resolution (bandwidth) of approximately 0.004 $k.y.^{-1}$

Although detailed post-cruise stratigraphic studies incorporating oxygen isotopes will refine the Site 984 chronostratigraphy, time series of MST data using the age model presented here have well-defined orbital-band oscillations through the base of the Olduvai Subchron. Figure 15 shows power spectra of the Site 984 magnetic susceptibility spliced record (see "Composite Depths" section, this chapter) using the age control points in Table 9. Over the interval from 0 to 1 Ma, variance is concentrated at frequencies corresponding to 100-k.y., ~40-k.y., 23-k.y., and 19-k.y. periods. From 1 to 2 Ma, 100-k.y. variance is reduced and variance is concentrated at ~63 k.y., ~36 k.y., 23 k.y., and 18 k.y. Further study should help to determine if the significant concentration of variance at sub-Milankovitch frequencies is climatically driven.

ORGANIC GEOCHEMISTRY

The shipboard organic geochemistry program at Site 984 consisted of analyses of volatile hydrocarbons, determinations of inorganic carbon, total nitrogen, total carbon, and total sulfur, and pyrolysis measurements (for methods, see "Explanatory Notes" chapter, this volume).

Volatile Hydrocarbon

As part of the shipboard safety and pollution monitoring program, concentrations of methane (C_1), ethane (C_2), and propane (C_3) gases were measured in every core using standard ODP headspace-sampling technique. The results are presented in Table 10 and displayed in Figure 16. Forty-eight sediment samples were collected from Holes 984A (3.0–172.6 mbsf) and 984B (185.5–498.6 mbsf). The profile of headspace gases from Site 984 is similar to that at Site 983 (data from both sites are plotted on the methane profile in Fig. 16). As at Site 983, methane concentrations in sediments are very low above 110 mbsf (from Sample 162-984A-1H, 0–5 cm, to 162-984A-12H, 0–5 cm). At about 110 mbsf, CH_4 starts to increase to maximum value of about 10,500 ppm between 250 and 280 mbsf, then decreases to about 3500 ppm at the bottom of Hole 984B (Fig. 16). The methane distribution shown in Figure 16 resembles the methane curve of Site 983. Ethane and propane occur in detectable amounts below 163.1 mbsf (Fig. 16; Table 10). A spike-like decrease in methane concentration (307.8 mbsf; Sample 162-984B-33X-5, 0–5 cm) is caused by the deficiency of sample volume in this particular sample.

In general, the C_1/C_2 (methane/ethane) ratios decrease consistently with burial depth due to the increasing influence of early diagenetic generation of hydrocarbons. At Site 984, the C_1/C_2 ratios show maximum at about 250 mbsf, and then a general decrease with increasing depth, to values of 687 at bottom of Hole 984B (Fig. 16). These data suggest that the methane at Site 984 most likely derived from in situ bacterial methanogenesis, resulting from decomposition of organic matter in the sediments. This also leads to the inverse relationship between methane concentration and sulfate content of interstitial waters (see "Inorganic Geochemistry" section, this chapter).

Carbon, Nitrogen, and Sulfur Concentration

Determinations of inorganic carbon, carbonate, total carbon, total nitrogen, and total sulfur in Hole 984B are summarized in Table 11. Calcium carbonate content in the sediment sequence of Hole 984B fluctuated between 0.4% and 32.2%, with an average value of 8.0% (Fig. 16; Table 11). These data show that the $CaCO_3$ content is gradually decreasing downhole and fluctuates with a lower amplitude with increasing depth. As at Site 983, the carbonate cycles of Hole 984B reflect glacial/interglacial fluctuations.

Total organic carbon (TOC) contents vary between 0% and 0.55%, with an average value of 0.21% (Fig. 16; Table 11). High

Table 9. Age control points, Site 984.

Event	Age (Ma)	984A (mbsf)	984A (mcd)	984B (mbsf)	984B (mcd)	984C (mbsf)	984C (mcd)	984D (mbsf)	984D (mcd)	Avg. depth (mbsf)	Avg. depth (mcd)	Rate (mbsf/m.y.)	Rate (mcd/m.y.)
Core top	0.00	0.00	0.00	0.00	0.00	0.00	0.00	0.00	0.00	0.00	0.00		
FO *E. huxleyi* (N)	0.26			38.10	42.49					38.10	42.49	146.54	163.42
LO *P. lacunosa* (N)	0.46			65.60	70.58					65.60	70.58	137.50	140.45
Brunhes/Matuyama	0.78	97.80	107.92	100.20	108.06	96.70	107.54			98.23	107.84	101.98	116.44
Jaramillo top	0.99	119.25	131.59	121.70	131.97	120.70	131.72			120.55	131.76	106.27	113.90
Jaramillo bottom	1.07	131.65	144.78	132.50	144.68	132.40	144.84			132.18	144.77	145.42	162.58
LO *Gephyrocapsa* spp. A/B (N)	1.23			148.60	161.63					148.60	161.63	102.60	105.40
Olduvai top	1.77			195.90	214.30	196.80	214.68	196.80	214.15	196.50	214.38	88.70	97.68
Olduvai bottom	1.95			222.25	242.52	217.25	237.09	216.60	237.07	218.70	238.89	123.33	136.20
Reunion II top	2.14			241.85	264.35	240.95	263.98			241.40	264.17	119.47	133.01
FO *P. lacunosa* (N)	3.70			>503.70	>526.20					>503.70	>526.20	>168.14	>167.97

Notes: Ages are from Berggren et al. (1995). N = calcareous nannofossil.

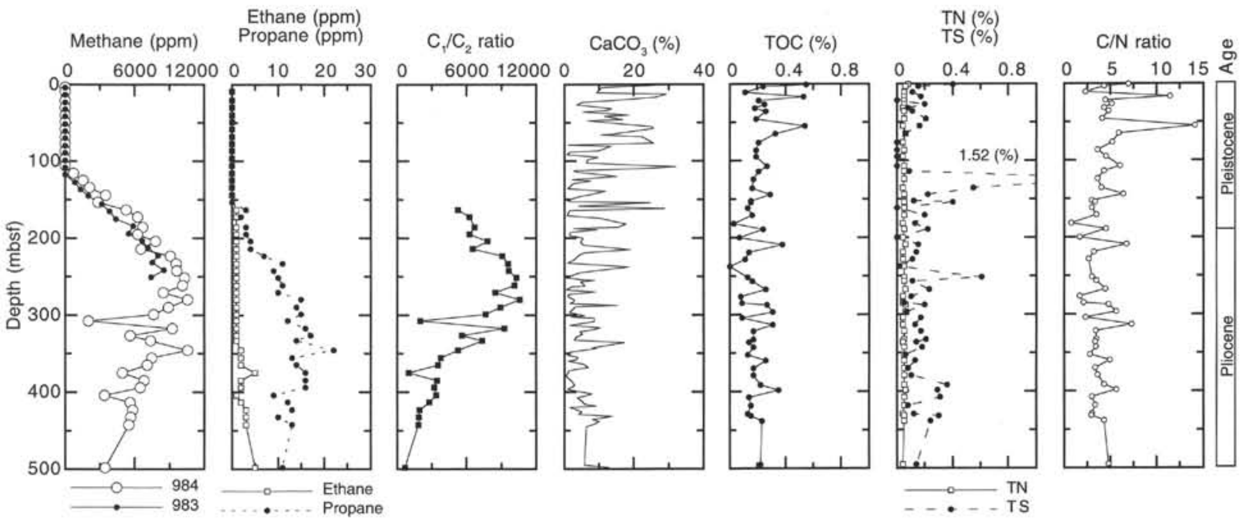

Figure 16. Methane, ethane, and propane concentrations, methane/ethane (C_1/C_2) ratio, calcium carbonate ($CaCO_3$), total organic carbon (TOC), total nitrogen (TN), and total sulfur (TS) contents, and TOC/TN (C/N) ratio and sediment age in Hole 984B.

TOC values (>0.5%) occur in the upper part of the sedimentary record of Hole 984B, Samples 162-984B-1H-1, 90–91 cm, 2H-6, 118–119 cm, and 6H-6, 83–84 cm). These samples have relatively high $CaCO_3$ content and high C/N ratios. Total nitrogen contents are generally very low (0.04%–0.08%; Fig. 16; Table 11). Total sulfur values vary between 0% and 0.61% throughout, with an average of 0.18% (Fig. 16; Table 11). A single peak of high total sulfur (1.52%) occurs in the upper part of Hole 984B (Sample 162-984B-14H-1, 139–140 cm; 123.89 mbsf). Pyrite grains are not visually observed in the sediments, but may occur as disseminated grains in this interval of high total sulfur content.

Composition of Organic Matter

Due to the organic carbon-poor nature of the sediments, pyrolysis analyses were not made. C/N ratios varied between 0.8 and 14.1 (Fig. 16; Table 11), indicating a predominance of marine organic material (Fig. 17). The relatively high C/N ratio of two samples (162-984B-2H-6, 118–119 cm, 17.18 mbsf, and 162-984B-6H-6, 83–84 cm, 54.83 mbsf) suggest a mixture of marine and terrigenous organic matter in the upper sedimentary section.

INORGANIC GEOCHEMISTRY

Interstitial Water

The pore-water profiles from Site 984 on the Bjorn Drift are very similar to those analyzed from Site 983 on the Gardar Drift to the south. Drilling at Site 984 penetrated considerably deeper than at Site 983, extending the profiles to 500 mbsf. For comparison, data from Site 983 are also plotted on the interstitial water profiles from Site 984 (Fig. 18). As at Site 983, sulfate reduction and methanogenesis control the pore-water gradients of dissolved sulfate, ammonia, alkalinity, salinity, and phosphate. Sulfate decreases from near seawater values at the top of the section to zero at 120 mbsf (Fig. 18A; Table 12). At this level, methane in headspace samples begins to increase,

Table 10. Results of headspace gas analysis of Hole 984A and 984B samples.

Core, section, interval (cm)	Depth (mbsf)	C_1 (ppm)	C_2 (ppm)	$C_{2=}$ (ppm)	C_3 (ppm)	C_1/C_2	C_1/C_3	$C_1/C_{2=}$
162-984A-								
1H-3, 0–5	3.03	2						
2H-4, 0–5	9.63	3						
3H-5, 0–5	20.63	4						
4H-5, 0–5	30.13	4						
5H-5, 0–5	39.63	5						
6H-5, 0–5	49.13	5						
7H-5, 0–5	58.63	4						
8H-5, 0–5	68.13	4						
9H-5, 0–5	77.63	3						
10H-5, 0–5	87.13	4						
11H-5, 0–5	96.63	6						
12H-5, 0–5	106.13	19						
13H-5, 0–5	115.63	700						
14H-5, 0–5	125.13	1,563						
15H-5, 0–5	134.63	2,090						
16H-5, 0–5	144.13	3,464						
17H-5, 0–5	153.63	2,818						
18H-5, 0–5	163.13	5,244	1		3	5,244	1748	1311
19H-5, 0–5	172.63	6,237	1		2	6,237	3119	2079
162-984B-								
20H-5, 0–5	185.53	6,711	1		3	6,711	2237	1678
21H-5, 0–5	195.03	6,265	1		3	6,265	2088	1566
22H-5, 0–5	204.53	7,818	1		4	7,818	1955	1564
23H-5, 0–5	214.03	6,517	1		4	6,517	1629	1303
24H-5, 0–5	223.53	9,109	1		7	9,109	1301	1139
25H-5, 0–5	233.03	9,594	1		11	9,594	872	800
26H-5, 0–5	242.53	9,669	1		9	9,669	1074	967
27H-5, 0–5	252.03	10,335	1		10	10,335	1034	940
28H-5, 0–5	261.53	10,156	1		11	10,156	923	846
29H-5, 0–5	271.03	8,496	1		10	8,496	850	772
30H-5, 0–5	280.53	10,606	1		15	10,606	707	663
31H-5, 0–5	290.08	8,910	1		14	8,910	636	594
32X-5, 0–5	299.53	7,644	1		15	7,644	510	478
33X-5, 0–5	307.83	2,017	1	0.5	12	2,017	168	149
34X-5, 0–5	317.43	9,256	1	0.3	16	9,256	579	535
35X-5, 0–5	327.03	5,617	1	0.2	17	5,617	330	309
36X-3, 0–5	333.63	7,365	1	0.2	14	7,365	526	485
37X-5, 0–5	346.23	10,558	2	0.0	22	5,279	480	440
38X-5, 0–5	355.83	7,498	2	0.0	13	3,749	577	499
39X-5, 0–5	365.43	7,098	2	0.1	14	3,549	507	441
40X-5, 0–5	375.13	4,945	5	0.2	16	989	309	233
41X-5, 0–5	384.73	6,838	2	0.1	16	3,419	427	378
42X-5, 0–5	394.43	6,475	2	0.1	16	3,238	405	359
43X-5, 0–5	404.03	3,415	1	0.3	9	3,415	379	332
44X-5, 0–5	413.63	5,591	2	0.3	12	2,796	466	391
45X-5, 0–5	423.33	5,826	3	0.2	13	1,942	448	360
46X-5, 0–5	432.93	5,662	3	0.1	10	1,887	566	432
47X-5, 0–5	442.53	5,500	3	0.0	13	1,833	423	344
53X-4, 0–5	498.63	3,436	5	0.2	11	687	312	212

reaching a maximum between 260 and 280 mbsf, and then generally declines toward the base of the hole (Fig. 18B). As a product of both sulfate reduction and methanogenesis, ammonia increases downhole from 150 µM at the top of the hole to a maximum of about 3100 µM at 290 mbsf, and then decreases to 2200 µM at the bottom of the hole (Fig. 18C; Table 12). As a product of sulfate reduction, alkalinity increases downhole from a surface value of 4 mM to a broad maximum between 49 and 144 mbsf, followed by decreasing values to the base of the hole (Fig. 18D; Table 12). The alkalinity maximum in Site 983 appears to be several millimolar higher than that measured in Site 984.

Salinity decreases abruptly in the top 100 m from 35 to 32, reflecting removal of dissolved sulfate, and then values remain constant to the bottom of the hole (Fig. 18E; Table 12). Phosphate values are relatively high in the top 100 m of the section and then decrease quickly between 100 and 200 mbsf, after which values remain relatively constant at 4 to 5 µM (Fig. 18F; Table 12). Similar to alkalinity, peak phosphate values at Site 984 are lower than those measured at Site 983.

Magnesium concentrations decrease steadily downcore from 51 mM at the surface to 5.3 mM at the bottom of the hole (Fig. 18G; Table 12), reflecting uptake by clay minerals during in situ alteration of volcanic material and chemical interaction with basaltic basement below. Calcium concentrations decrease from about 10 to 4 mM in the top 50 m of the hole, the zone of sulfate reduction, and then slowly increase to a depth of about 300 m (Fig. 18H; Table 12). Below 300 m, calcium increases abruptly in two steps, reaching a maximum of 39 mM at the base of the hole. The relationship between calcium and magnesium is curvilinear (Fig. 18I). Calcium and magnesium are positively correlated in the upper 50 m, reflecting calcite precipitation in the zone of sulfate reduction. Below 50 m, calcium increases and magnesium decreases downhole, indicating in situ alteration of volcanic material in the sediment and interaction with oceanic basement below.

Chloride and sodium concentrations increase downcore at both Sites 983 and 984, with a slope of approximately 2:1 (Na:Cl) for the upper 260 m (Fig. 18J, -K, -L; Table 12). This increase probably reflects the uptake of water by clay mineral formation during hydration reactions of volcanogenic sediments; however, sodium increases at twice the rate of chloride, indicating another source for this element.

Silica concentrations increase from the top of the hole to 270 mbsf and then display considerable variability to the base of the hole (Fig. 18M; Table 12). This is consistent with similar trends seen in the preservation of siliceous microfossils at this site (see "Biostratigraphy" section, this chapter).

Potassium varies between 10 and 13 mM in the top 300 m. Potassium decreases below 300 mbsf, reaching a minimum value of 7 mM (Fig. 18N). This decrease may reflect uptake of potassium during

Table 11. Summary of organic geochemical analyses of Hole 984B samples.

Core, section, interval (cm)	Depth (mbsf)	IC (%)	$CaCO_3$ (%)	TC (%)	TOC (%)	TN (%)	TS (%)	C/N
162-984B-								
1H-1, 90–91	0.90	3.21	26.7	3.76	0.55	0.08	0.40	6.9
1H-3, 60–61	3.60	1.62	13.5	1.86	0.24	0.06	0.15	4.3
1H-3, 90–91	3.90	1.30	10.8					
2H-2, 118–119	11.18	1.12	9.3	1.23	0.11	0.05	0.11	2.3
2H-3, 118–119	12.68	3.53	29.4					
2H-6, 118–119	17.18	3.16	26.3	3.69	0.53	0.05	0.17	11.4
3H-3, 41–42	21.41	1.39	11.6	1.60	0.21	0.05	0.00	4.4
3H-4, 82–83	23.32	0.62	5.2					
3H-6, 122–123	26.72	0.42	3.5	0.67	0.25	0.05	0.20	5.1
4H-3, 118–119	31.68	1.64	13.7	1.82	0.18	0.04	0.08	4.3
4H-5, 118–119	34.68	1.46	12.2					
4H-6, 118–119	36.18	0.65	5.4	0.91	0.26	0.05	0.11	4.8
5H-2, 121–122	39.71	2.23	18.6					
5H-4, 38–39	41.88	1.40	11.7					
5H-6, 121–122	45.71	2.03	16.9	2.22	0.19	0.05	0.21	4.1
6H-1, 99–100	47.49	0.79	6.6					
6H-6, 83–84	54.83	2.99	24.9	3.53	0.54	0.04	0.16	14.1
7H-1, 136–137	57.36	3.09	25.7					
7H-6, 139–140	64.89	1.61	13.4	1.94	0.33	0.06	0.06	5.9
8H-1, 54–55	66.04	1.26	10.5					
8H-2, 132–133	68.32	2.69	22.4					
9H-2, 57–58	77.07	3.07	25.6	3.28	0.21	0.04	0.00	5.2
9H-3, 119–120	79.19	0.13	1.1					
9H-4, 132–133	80.82	1.60	13.3					
10H-2, 107–108	87.07	1.16	9.7	1.35	0.19	0.05	0.00	3.6
10H-3, 85–86	88.35	0.18	1.5					
10H-5, 108–109	91.58	0.09	0.7					
11H-1, 91–92	94.91	1.16	9.7	1.35	0.19	0.04	0.00	4.5
11H-3, 135–136	98.35	0.80	6.7					
11H-6, 81–82	102.31	0.75	6.2					
12H-3, 130–131	107.80	3.87	32.2	4.14	0.27	0.05	0.00	6.0
12H-4, 136–137	109.36	3.11	25.9					
12H-6, 136–137	112.36	0.30	2.5					
13H-1, 134–135	114.34	0.42	3.5	0.63	0.21	0.05	0.09	4.3
13H-5, 136–137	120.36	1.83	15.2					
14H-1, 139–140	123.89	0.26	2.2	0.43	0.17	0.05	1.52	3.6
14H-3, 42–43	125.92	0.91	7.6					
14H-5, 35–36	128.85	0.30	2.5					
15H-3, 118–119	136.18	0.12	1.0	0.28	0.16	0.04	0.55	4.0
15H-5, 118–119	139.18	1.42	11.8					
16H-2, 118–119	144.18	0.83	6.9	1.12	0.29	0.05	0.22	6.4
16H-3, 118–119	145.68	0.53	4.4					
16H-6, 118–119	150.18	0.19	1.6					
17H-1, 118–119	152.18	0.15	1.2	0.30	0.15	0.05	0.12	3.0
17H-3, 42–43	154.42	2.96	24.7	3.11	0.15	0.05	0.40	3.3
17H-5, 118–119	158.18	0.48	4.0					
18H-1, 100–101	161.50	3.46	28.8	3.59	0.13	0.05	0.00	3.0
18H-3, 100–101	164.50	0.17	1.4					
19H-1, 100–101	171.00	0.09	0.7	0.25	0.16	0.05	0.20	3.5
19H-3, 100–101	174.00	1.24	10.3					
20H-2, 38–39	185.88	1.87	15.6					
20H-6, 38–39	187.38	0.30	2.5					
21H-1, 37–38	189.37	1.14	9.5	1.38	0.24	0.05	0.22	4.5
21H-3, 38–39	192.38	0.20	1.7					
21H-6, 38–39	196.88	0.17	1.4					
22H-1, 138–139	199.88	0.64	5.3	0.71	0.07	0.04	0.00	1.7
22H-5, 140–141	205.90	0.56	4.7					
23H-1, 138–139	209.38	0.66	5.5	1.04	0.38	0.06	0.15	6.7
23H-5, 140–141	215.40	2.28	19.0					
24H-1, 144–145	218.94	0.66	5.5	0.80	0.14	0.04	0.14	3.2
24H-4, 135–136	223.35	0.47	3.9					
25H-1, 101–102	228.01	0.34	2.8	0.45	0.11	0.04	0.11	2.6
25H-4, 114–115	232.64	0.12	1.0					
26H-1, 87–88	237.37	2.25	18.7	1.32	0.00	0.05	0.02	
26H-6, 123–124	245.23	0.54	4.5					
27H-4, 128–129	251.78	0.05	0.4	0.18	0.13	0.05	0.61	3.0
27H-6, 96–97	254.46	0.62	5.2					
27H-6, 123–124	254.73	1.05	8.7					
28H-1, 143–144	256.93	0.57	4.7	0.73	0.16	0.05	0.11	3.5
28H-5, 105–106	262.55	0.71	5.9					
28H-6, 44–45	263.44	0.24	2.0					
29H-2, 115–116	267.65	0.06	0.5	0.32	0.26	0.06	0.23	4.4
29H-4, 47–48	269.97	1.07	8.9					
29H-6, 96–97	273.46	0.14	1.2					
30H-2, 107–108	277.07	0.13	1.1	0.21	0.08	0.04	0.10	1.7
30H-4, 101–102	280.01	0.32	2.7					
30H-6, 100–101	283.00	0.30	2.5					
31H-1, 91–92	284.91	0.18	1.5	0.27	0.09	0.04	0.05	2.1
31H-3, 91–92	287.91	1.84	15.3	2.11	0.27	0.06	0.20	4.8
31H-4, 91–92	289.46	0.37	3.1					
32X-3, 42–43	296.92	0.17	1.4	0.48	0.31	0.06	0.07	5.6
32X-5, 110–111	300.60	0.69	5.7					
32X-7, 42–43	302.92	0.23	1.9					
33X-2, 119–120	304.49	1.05	8.7	1.14	0.09	0.04	0.17	2.3
33X-5, 70–71	308.50	1.05	8.7					
34X-2, 60–61	313.50	0.20	1.7	0.51	0.31	0.04	0.13	7.3
34X-4, 60–61	316.50	1.24	10.3					
34X-6, 60–61	319.50	1.00	8.3					

Table 11 (continued).

Core, section, interval (cm)	Depth (mbsf)	IC (%)	$CaCO_3$ (%)	TC (%)	TOC (%)	TN (%)	TS (%)	C/N
35X-1, 100–101	322.00	0.53	4.4	0.70	0.17	0.05	0.17	3.4
35X-3, 100–101	325.00	0.61	5.1					
35X-5, 100–101	328.00	0.42	3.5					
36X-2, 41–42	332.51	0.33	2.7	0.50	0.17	0.05	0.21	3.5
36X-4, 60–61	335.70	2.06	17.2	2.20	0.14	0.04	0.14	3.3
37X-2, 80–81	342.50	0.98	8.2	1.15	0.17	0.05	0.18	3.4
37X-3, 50–51	343.70	1.10	9.2					
37X-6, 100–101	348.70	0.21	1.7					
38X-2, 80–81	352.10	0.11	0.9	0.24	0.13	0.05	0.06	2.8
38X-4, 50–51	354.80	0.47	3.9					
38X-6, 100–101	358.30	0.41	3.4					
39X-1, 87–88	360.27	0.13	1.1	0.39	0.26	0.05	0.13	4.9
39X-4, 11–12	364.01	0.67	5.6					
39X-7, 18–19	368.58	0.82	6.8					
40X-1, 96–97	370.06	0.48	4.0	0.65	0.17	0.05	0.08	3.3
40X-3, 50–51	372.60	0.16	1.3					
40X-6, 57–58	377.17	0.09	0.7					
41X-1, 78–79	379.48	0.05	0.4	0.22	0.17	0.05	0.10	3.6
41X-6, 64–65	386.84	0.27	2.2					
42X-3, 52–53	391.92	0.35	2.9	0.57	0.22	0.05	0.36	4.3
42X-6, 103–104	396.93	0.12	1.0					
43X-1, 23–24	398.23	0.34	2.8	0.69	0.35	0.06	0.29	5.6
43X-3, 128–129	402.28	0.96	8.0					
43X-6, 63–64	406.13	0.65	5.4					
44X-1, 9–10	407.69	0.46	3.8	0.60	0.14	0.05	0.31	3.0
44X-4, 79–80	412.89	0.63	5.2					
44X-6, 79–80	415.89	0.68	5.7					
45X-1, 128–129	418.58	1.08	9.0	1.23	0.15	0.05	0.08	3.3
45X-2, 127–128	420.07	0.19	1.6					
45X-6, 98–99	425.78	0.60	5.0					
46X-2, 102–103	429.42	0.48	4.0	0.61	0.13	0.04	0.12	3.0
46X-4, 68–69	432.08	1.66	13.8	1.81	0.15	0.05	0.30	2.9
46X-6, 130–131	435.70	0.98	8.2					
47X-2, 85–86	438.85	1.20	10.0	1.43	0.23	0.05	0.24	4.3
47X-4, 104–105	442.04	1.05	8.7					
47X-6, 120–121	445.20	0.76	6.3					
53X-1, 130–131	495.40	0.70	5.8	0.92	0.22	0.04	0.14	4.8
53X-3, 95–96	498.05	1.54	12.8					
53X-4, 135–136	499.95	1.51	12.6					
	Average:	0.96	8.0	1.29	0.21	0.05	0.18	4.3
	Maximum:	3.87	32.2	4.14	0.55	0.08	1.52	14.1
	Minimum:	0.05	0.4	0.18	0.00	0.04	0.00	0.8

Notes: IC = inorganic carbon, $CaCO_3$ = calcium carbonate, TC = total carbon, TOC = total organic carbon, TN = total nitrogen, TS = total sulfur, and C/N = total organic carbon/total nitrogen ratio.

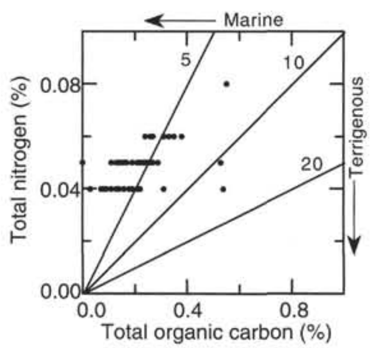

Figure 17. Total organic carbon vs. total nitrogen in Hole 984B. Lines show C/N ratios of 5, 10, and 20.

clay mineral formation or alteration, in situ alteration of basalt, or interactions with oceanic basement. Lithium concentrations are relatively constant in the upper 100 m of section and then increase toward the base of the core, from values of 20 μM at 100 mbsf to 99 μM at the base of the hole (Fig. 18O; Table 12). The linear increase of lithium with depth correlates well with dissolved magnesium, reflecting similar exchanges with volcanic material in the sediments and/or with oceanic basement below.

Pore-water strontium concentrations are about 100 μM at the surface and decrease slightly in the top 50 mbsf, and then begin to increase downcore at a slow, constant rate (Fig. 18P; Table 12). An abrupt increase occurs in the deepest sample, reaching a value of 250 μM at the bottom of the hole. Increasing strontium values downhole most likely reflect dissolution of biogenic calcite and secondary precipitation of inorganic calcite, although small contributions of strontium can be derived from alteration of volcanic material (Gieskes, 1981).

PHYSICAL PROPERTIES

Index property measurements were generally made on one (10-cm^3) sample per working-half section in all cores (see "Explanatory Notes" section, this volume) and are presented in Table 13. Solid-core compressional velocity and undrained shear strength measurements were made at a resolution of about one measurement per section on the working half from Hole 984B (Tables 14, 15). The motorized vane was used to 253 mbsf and the pocket penetrometer was used from 124 to 263 mbsf. The T1 transducers of the digital sound velocimeter (DSV) were used to a depth of about 29 mbsf. Below this depth the sediment became too consolidated to use the DSV, and the Hamilton Frame was used to make sonic measurements through the core liner to 298 mbsf, and on pieces removed from the liner below 299 mbsf. Thermal conductivity measurements are pre-

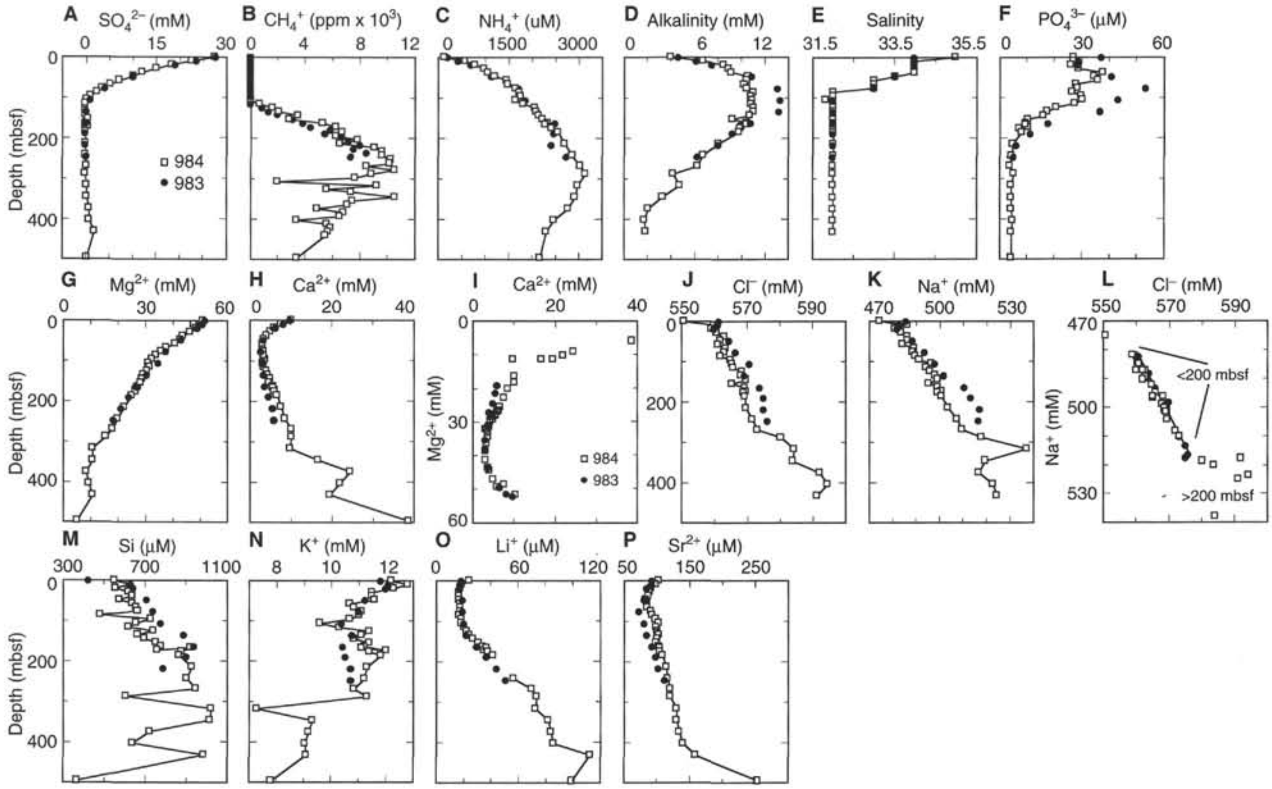

Figure 18. Vertical profiles of sulfate (**A**), headspace methane (**B**), ammonium (**C**), alkalinity (**D**), salinity (**E**), phosphate (**F**), magnesium (**G**), calcium (**H**), calcium vs. magnesium (**I**), chloride (**J**), sodium (**K**), chloride vs. sodium (**L**), silica (**M**), potassium (**N**), lithium (**O**), and strontium (**P**) at Sites 983 (solid circles) and 984 (open squares).

Table 12. Composition of interstitial waters in Holes 984A and 984B.

Core, section, interval (cm)	Depth (mbsf)	pH	Alkalinity (mM)	Salinity	Cl (mM)	Na (mM)	SO_4 (mM)	NH_4 (µM)	Si (µM)	PO_4 (µM)	K (µM)	Mg (mM)	Ca (mM)	Sr (µM)	Li (µM)
162-984A-															
1H-1, 145–150	1.45	7.75	3.978	35.0	550	474	27.5	147	555	27.0	12.2	51.1	10.2	103	24.5
2H-3, 145–150	9.55	7.78	6.671	34.0	560	486	22.5	579	632	26.9	12.8	47.9	7.6	100	19.3
3H-4, 145–150	20.55	7.78	8.481	34.0	559	481	18.4	809	564	26.0	12.3	48.7	6.1	91	17.7
4H-4, 145–150	30.05	7.78	8.894	34.0	560	483	15.0	986	622	28.8	11.5	46.3	4.9	89	16.8
5H-4, 145–150	39.55	7.86	9.175	34.0	562	486	11.9	1083	643	37.6	11.5	43.9	4.2	88	17.0
6H-4, 145–150	49.05	7.95	10.545	33.5	562	486	10.2	1212	581	34.6	11.6	43.0	3.6	84	17.3
7H-4, 145–150	58.55	7.69	10.489	33.0	561	484	7.0	1446	641	35.7	10.7	40.9	3.2	86	17.6
8H-4, 145–150	68.05	7.74	10.287	33.0	563	489	5.2	1498	662	27.8	10.8	37.8	3.1	86	17.7
9H-4, 145–150	77.55	7.97	10.457	33.0	562	488	3.5	1652	671	28.5	11.1	35.7	3.4	91	17.6
10H-4, 145–150	87.05	8.11	11.067	32.0	562	489	2.3	1740	486	26.6	11.0	33.8	3.6	94	16.9
11H-4, 145–150	96.55	7.72	10.811	32.0	564	491	1.0	1757	729	29.8	10.7	32.7	3.7	100	18.5
12H-4, 145–150	106.05	7.70	10.895	31.8	565	496	0.3	1648	663	30.1	9.6	31.4	3.0	104	19.1
13H-4, 145–150	115.55	7.83	10.823	32.0	565	494	0.0	1825	625	27.6	10.3	31.5	3.5	99	20.5
14H-4, 145–150	125.05	7.88	11.047	32.0	568	495	0.0	2051	742	20.6	11.4	30.6	4.1	101	22.9
15H-4, 145–150	134.55	7.88	11.040	32.0	567	498	0.0	2083	669	17.5	11.1	29.1	4.4	103	24.9
16H-4, 145–150	144.05	7.86	10.661	32.0	569	499	0.0	2140	698	15.9	10.8	28.8	5.0	101	27.5
17H-4, 145–150	153.55	7.86	9.282	32.0	565	495	0.5	2241	756	10.5	11.4	28.2	4.7	100	30.8
162-984B-															
18H-4, 145–150	163.05	7.86	10.447	32.0	569	499	0.2	2329	783	9.5	11.2	27.6	5.7	106	33.8
19H-4, 145–150	172.55	8.01	10.067	32.0	569	500	0.4	2422	765	10.2	12.0	26.3	6.0	106	35.0
18H-4, 145–150	166.45	7.67	10.514	32.0			0.0	2293	928	9.2	11.1	27.1	5.7	107	36.8
19H-4, 145–150	175.95	7.81	9.959	32.0	568	499	0.0	2410	879	7.3	11.4	26.2	6.1	107	37.8
20H-4, 145–150	185.45	7.85	9.830	32.0	569	500	0.0	2555	869	8.1	11.8	24.9	6.6	109	41.1
23H-4, 145–150	213.95	7.76	8.020	32.0	569	503	0.0	2693	932	4.7	11.3	22.1	7.5	114	
26H-4, 145–150	242.45	7.78	6.733	32.0	571	507	0.0	2858	909	4.5	11.2	19.6	8.4	117	57.1
29H-4, 145–150	270.95	7.65	6.274	32.0	573	509	0.2	3023	951	3.9	10.8	17.7	10.1	120	69.5
31H-4, 145–150	290.00	8.03	4.237	32.0	580	517	0.0	3128	610	5.0	11.3	15.8	10.0	121	73.6
34X-4, 145–150	317.35	7.65	4.722	32.0	584	537	0.2	2293	1027	4.5	7.3	10.6	9.8	131	73.1
37X-4, 145–150	346.15	7.73	3.281	32.0	583	519	0.3	2931	1023	4.2	9.3	10.8	16.7	131	81.8
40X-4, 145–150	375.05	7.91	2.101	32.0	592	516	0.9	2777	725	4.3	9.2	8.6	24.5	134	84.4
43X-4, 140–150	403.95	7.93	1.776	32.0	594	522	0.8	2471	644	4.7	9.0	9.5	21.9	141	85.8
46X-4, 145–150	432.85	7.79	1.922	32.0	591	524	1.9	2321	990	4.3	9.1	10.6	19.4	159	111.9
53X-4, 140–150	498.50						0.2	2184	371	4.5	7.8	5.3	38.6	254	99.4

Table 13. Index properties of samples from Holes 984B.

Core, section, interval (cm)	Depth (mbsf)	Water content (wet %)	Bulk density Method C (g/cm³)	Grain density Method C (g/cm³)	Dry density Method C (g/cm³)	Porosity Method C (%)	Void ratio Method C
162-984B-							
1H-1, 52–54	0.52	63.0	1.34	2.76	0.49	82.1	4.59
1H-1, 105–107	1.05	61.5	1.35	2.70	0.52	80.8	4.22
1H-2, 57–59	2.07	62.1	1.36	2.91	0.52	82.3	4.65
1H-3, 69–71	3.69	60.8	1.36	2.77	0.53	80.7	4.19
1H-4, 79–81	5.29	59.5	1.38	2.81	0.56	80.1	4.03
1H-5, 50–52	6.50	57.8	1.39	2.71	0.59	78.4	3.63
1H-6, 33–35	7.83	58.8	1.38	2.78	0.57	79.5	3.87
2H-1, 72–74	9.22	53.8	1.46	2.87	0.67	76.5	3.25
2H-2, 101–103	11.01	51.4	1.47	2.74	0.72	73.9	2.84

Only part of this table is reproduced here. The entire table appears on the CD-ROM (back pocket).

Table 14. Compressional-wave velocity measurements from Hole 984B.

Core, section, interval (cm)	Depth (mbsf)	Velocity (m/s)	Temperature (°C)	Direction
162-984B-				
1H-1, 40–47	0.44	1510	21.1	z
1H-1, 102–109	1.05	1514	21.0	z
1H-2, 53–60	2.07	1513	20.9	z
1H-3, 65–72	3.69	1510	20.8	z
1H-4, 75–82	5.29	1519	20.7	z
1H-5, 46–53	6.50	1493	20.6	z
1H-6, 28–35	7.82	1491	19.6	z
2H-1, 97–104	9.50	1502	20.9	z
2H-2, 69–76	10.73	1493	20.8	z
2H-3, 51–58	12.05	1496	20.7	z

Note: For explanation of measurement directions, see "Explanatory Notes" chapter (this volume).

Only part of this table is reproduced here. The entire table appears on the CD-ROM (back pocket).

Table 15. Undrained shear strength measurements from Hole 984B.

Core, section, interval (cm)	Depth (mbsf)	Undrained shear strength (kPa)	Spring no.	Penetrometer (kPa)
162-984B-				
1H-1, 106	1.06	12.3	1	
1H-2, 58	2.08	3.2	1	
1H-3, 69	3.69	7.1	1	
1H-4, 80	5.30	11.1	1	
1H-5, 51	6.51	7.0	1	
1H-6, 32	7.82	5.2	1	
2H-1, 102	9.52	18.9	1	
2H-2, 72	10.72	11.3	1	
2H-3, 55	12.05	11.5	1	

Only part of this table is reproduced here. The entire table appears on the CD-ROM (back pocket).

sented in Table 16. Thirteen downhole temperature measurements were made using the APC temperature tool.

Geotechnical Units

Three geotechnical units are defined at Site 984 (Fig. 19). Geotechnical Unit G1 extends from the seafloor to 170 mbsf and is divided into three subunits. Subunit G1A is defined in the first 23 mbsf and is characterized by a rapid decrease in porosity and an increase in magnetic susceptibility and density values. Subunit G1B (23 to 64 mbsf) is defined by a general leveling off in most physical property values. A more gradual decrease in density with depth occurs, with mean GRAPE and gravimetric wet bulk values of 1.25 and 1.51 g/cm³, respectively. Magnetic susceptibility and natural gamma radiation begin to show cyclic patterns with fairly long periods. At the base of Subunit G1B (in the interval from 60 to 64 mbsf) there are increases in density and strength values, and decreases in natural gamma radiation and porosity values. Natural gamma radiation exhibits fluctuations that are similar in character to those observed in the magnetic susceptibility record; these fluctuations, however, are not in phase. Subunit G1C (64 to 170 mbsf) exhibits less pronounced amplitude variations in magnetic susceptibility which visually mask the more obvious fluctuations seen in Subunit G1B. Porosity values show less of a decrease with depth than in Subunits G1A and G1B, while strength has a larger gradient of increase with depth than in Subunits G1A and G1B. Density values in Subunit G1C show more variation, with higher means (mean GRAPE is 1.29 g/cm³; mean gravimetric wet bulk density is 1.51 g/cm³). The natural gamma radiation record continues to show long frequency fluctuations but with a lower mean value, averaging more than 17.7 counts/s above 64 mbsf, but averaging only 15.8 counts/s within Subunit G1C. From 150 to 170 mbsf, Unit G1C also shows a distinct decrease in porosity and increases in strength and density.

Geotechnical Unit G2 (170 to 385 mbsf) differs from Unit G1 by having higher amplitude variations in magnetic susceptibility values and lower amplitude cycles in the natural gamma radiation values with a lower mean (from an average of 16.5 counts/s in Unit G1 to 13.9 counts/s in Unit G2), retaining the long period cyclicity. Mean porosity values drop to 62.0%, and in Unit G2 these values show a gradual decrease with depth. There is a gradual increase in density with depth, retaining the same gradient into geotechnical Unit G3. There is a change in the character of the sediments with a transition into more indurated sediments, eventually requiring a switch from APC to XCB coring at 295 mbsf (see "Operations" and "Lithostratig-

Table 16. Thermal conductivity measurements (corrected for drift) from Holes 984A and 984B.

Core, section, interval (cm)	Depth (mbsf)	Thermal conductivity (W/[m·K])	Standard error (W/[m·K])
162-984A-			
1H-2, 100	2.50	0.869	0.00260
1H-3, 100	4.00	0.851	0.00347
2H-1, 100	6.10	0.751	0.03775
2H-3, 100	9.10	0.938	0.00261
2H-5, 100	12.10	0.989	0.00466
3H-1, 50	15.10	0.878	0.00323
3H-3, 100	18.60	0.853	0.00290
3H-5, 100	21.60	0.927	0.00312
3H-7, 10	23.70	0.922	0.00400

Only part of this table is reproduced here. The entire table appears on the CD-ROM (back pocket).

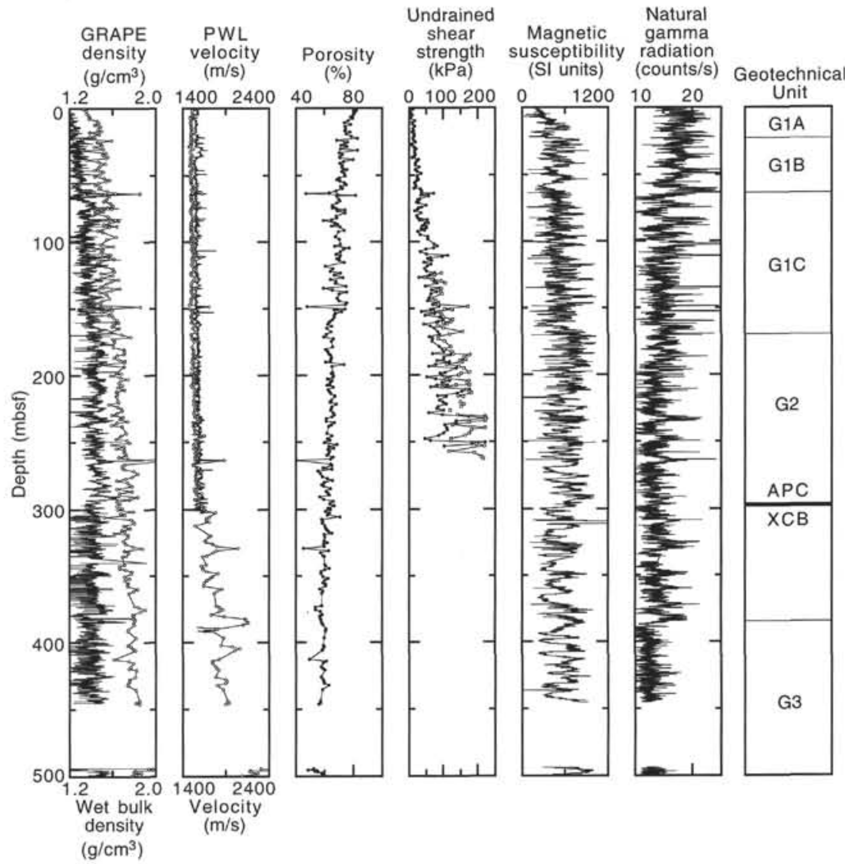

Figure 19. Plots of GRAPE bulk density (fine line) superimposed with gravimetric bulk density measurements (Method C; line with open circles), PWL velocity (fine line) superimposed with split-core velocity measurements (line with open circles), porosity, undrained shear strength measured with the vane (solid circles) or the pocket penetrometer (open squares), magnetic susceptibility, and natural gamma radiation, vs. sub-bottom depth in Hole 984B. Also shown are the boundaries of geotechnical units.

raphy" sections, this chapter). The magnetic susceptibility shows less frequent fluctuations starting from 260 mbsf and continuing down to the terminal depth, while natural gamma radiation amplitudes decrease. Below 295 mbsf, average magnetic susceptibility values drop from 627 SI units (268–295 mbsf) to an average of 518 SI units (295–385 mbsf), velocity values show more variability in amplitude, and GRAPE density shows greater variability. However, these changes probably reflect drilling disturbance caused by the XCB coring.

Geotechnical Unit G3 (385 mbsf to total depth in Hole 984B) marks a change in character of the natural gamma radiation record. The average natural gamma radiation value drops and remains fairly constant, averaging 12.6 counts/s. Velocities become higher at and just below the top of this unit, and a large velocity increase occurs in the last core.

Correlation with Lithostratigraphy, Seismic Stratigraphy, and Downhole Logs

Several of the seismic reflectors and lithostratigraphic unit boundaries correspond to geotechnical unit boundaries (see Fig. 32 in the "Seismic Stratigraphy" section, this chapter). The lower 4 m of geotechnical Subunit G1B (60–64 mbsf) contain jumps in density, velocity, and strength, and decreases in natural gamma radiation and porosity, which most likely generate seismic Reflector R1 (see "Seismic Stratigraphy" section, this chapter). In Subunit G1C, at approximately 100 mbsf, there are peaks in velocity and strength which most likely give rise to seismic Reflector R2, while the base of Subunit G1C (112 to 170 mbsf) coincides with lithostratigraphic Subunit IB (see "Lithostratigraphy" section, this chapter). The upper part of geotechnical Unit G2 (170 to 268 mbsf) coincides with lithostratigraphic Subunit IC. The depth at which coring operations were switched from APC to XCB roughly coincides with seismic Reflector R3 and the change into lithostratigraphic Subunit ID. A concentration of peaks in velocity and density at 395 mbsf most likely gives rise to seismic Reflector R4.

Discussion

Geotechnical Subunits G1A and G1B at Site 984 correlate with a similarly defined subunit at Site 983 (see "Physical Properties" section, "Site 983" chapter, this volume). In particular, Subunit G1B corresponds to the base of Subunit G1A at Site 983. Natural-gamma-radiation cyclicity is out of phase with the magnetic susceptibility record to the base of Unit G1 (Fig. 19), as at Site 983, and so is not necessarily driven by the same depositional factors (see "Lithostratigraphy" section, this chapter).

Figure 20A shows the difference between *P*-wave velocities measured downhole and in the laboratory: velocities measured downhole are generally higher than those measured in cores, probably due to core expansion during recovery (see "Wireline Logging" section, this chapter). In particular, above ~300 mbsf, in situ velocities are approximately 10% higher than those measured shipboard, whereas below this depth, the gradually more indurated sediments that required XCB coring from 300 mbsf, are exemplified by the two curves gradually merging between 300 and 400 mbsf. The noise in the shipboard results is caused by drilling disturbance. The velocity trend from 200 to ~450 mbsf shows a fairly constant increasing gradient with depth through Units G2 to G3. However, below the zone of no recovery (446–495 mbsf), the measured velocities are significantly higher than the extrapolated 200–450-mbsf trend. This would indicate a change in geotechnical properties somewhere within 446–495 mbsf.

Figure 20B shows downhole logging density measurements plotted alongside the shipboard discrete density measurements. The downhole tool was able to obtain measurements in the zone where no core was recovered, to a depth of 489.75 mbsf. The density data show a continuation of the gradual increase with depth; no significant

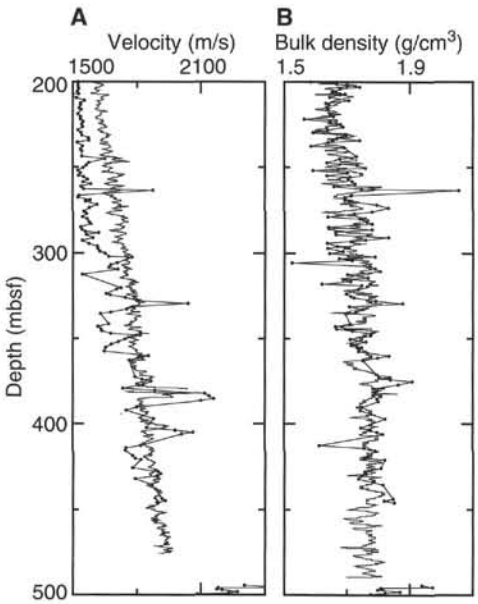

Figure 20. **A.** Downhole logging velocity measurements (fine line) alongside shipboard discrete velocities measurements (line with solid circles) from 200 mbsf to total depth in Hole 984B. **B.** Downhole logging density measurements (fine line) alongside shipboard wet bulk density measurements (line with solid circles) from 200 mbsf to total depth in Hole 984B.

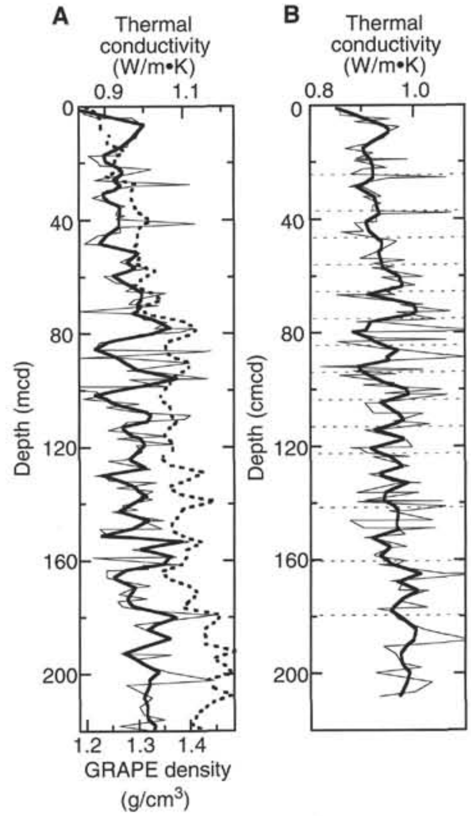

Figure 21. Thermal conductivity results combined from Holes 984A and 984B: (**A**) plotted with GRAPE bulk density data (dashed line) at meters composite depth (mcd) scale to illustrate the controlling density component, and (**B**) plotted at corrected meters composite depth (cmcd) to illustrate relationship to drilling depth and temperature measurement stations (dashed horizontal lines). GRAPE density (bold dashed line) and bold thermal conductivity lines are locally weighted least-squares fits to original data to emphasize general trends.

jumps in values are obvious. However, significantly higher values in both density and velocity were measured in the last core recovered which would suggest a significant change within this interval. These high velocity and density values may, however, be from a thin bed rather than from a new lithostratigraphic unit. Unfortunately, we have no core or log information from below 489.75 mbsf.

Heat Flow

Thirteen downhole temperature measurements were taken successfully with the APC temperature tool in Hole 984B between 27 and 180 mbsf. We also measured thermal conductivity in the sediment cores of Holes 984A and 984B over this interval at a frequency of about one per 2 m in each hole. The objective was to investigate the potential geothermal response to Holocene changes in bottom-water temperature and to establish the local heat flow in sediments resting on young ocean crust close to a hotspot region.

The thermal conductivity measurements from Holes 984A and 984B were normalized for the five different needle probes, using the control measurements taken in a red rubber standard for each run (see "Explanatory Notes" chapter, this volume). The data from both holes were then spliced using the meters composite depth (mcd) scale to provide a data set for Hole 984B supplemented by data from Hole 984A. Comparing the spliced data with GRAPE bulk density data from Hole 984B at the same mcd depth scale illustrates that thermal conductivity variations are related to bulk density variations (Fig. 21). However, the gradual, average increase in bulk density is not reflected in the average downhole trend of thermal conductivity data over the measured interval.

The spliced thermal conductivity data were depth-corrected to match the drilled interval for each core (see "Explanatory Notes" chapter, this volume). This ensured that the correct thermal conductivity values were used to calculate equilibrium temperatures at each temperature measurement station (Fig. 21B).

APC temperature measurements were carried out using tool numbers 12 and 18. The temperature measurements from above 90 mbsf were useful but of limited quality, with estimated errors of ±0.3° to ±0.5°C. Parts of Cores 162-984B-3H, 5H, and 9H records were strongly affected by frictional heating, while Cores 162-984B-4H, 7H, and 8H records were very noisy (Fig. 22). However, the shallow sediments were clearly firmer here than at Site 981, where no useful results were obtained above 70 mbsf. Below 90 mbsf, the measurements were of good quality, with estimated errors of ±0.1° to ±0.2°C, that is, the calculated curve fits matched the data well over the entire measurement period of about 10 min (Fig. 22). The calculated equilibrium temperatures of all measurements yielded a thermal gradient of 10.5°C/100 m (Fig. 23), twice the gradient measured at Site 981. Using an average thermal conductivity of 0.96 W/(m·K), this amounts to an average heat flow of 0.101 W/m^2.

We measured the bottom-water temperature on the first five successful runs (Cores 162-984B-3H to 8H) as follows: the recording tool was held at about 20 m above seafloor (within the drill pipe) for 10 min before being lowered to shooting depth. After the core had been retrieved, the temperature tool was again held 20 m above seafloor for 10 min. All bottom-water records displayed an equilibrium curve, and the calculated equilibration temperatures (using a thermal conductivity for water of 0.68 W/[m·K]) ranged between 2.28° and 2.88°C (Table 17). The measurements taken before the coring were smoother, that is, less noisy, than those taken after coring and are illustrated in Figure 22N. It is not quite clear why the temperatures did not equilibrate more rapidly and reach a constant temperature. We

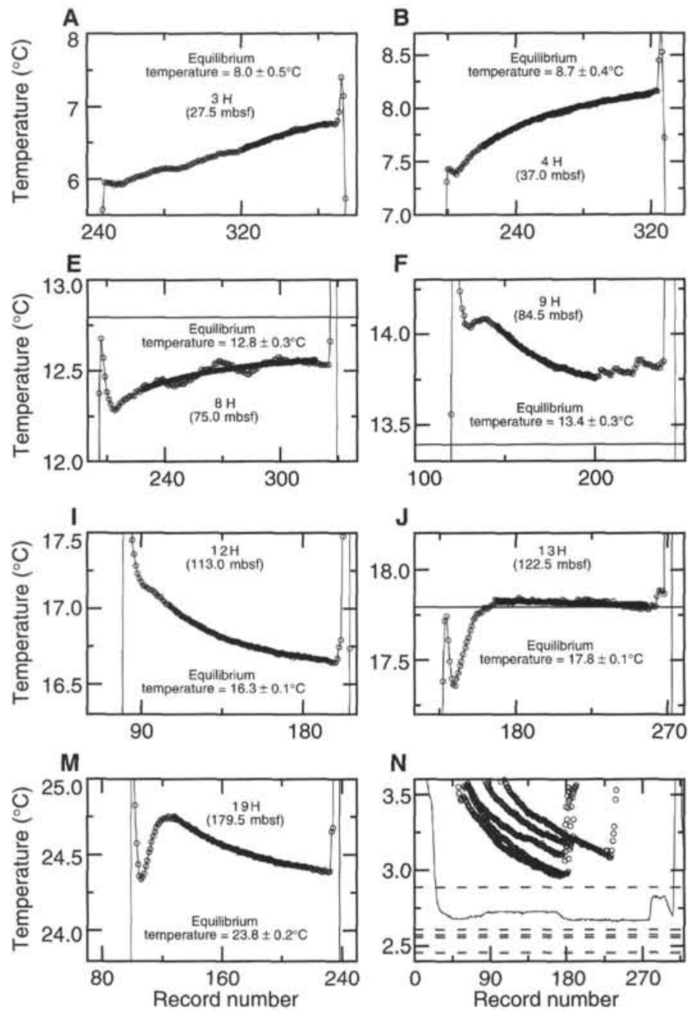

Figure 22. Hole 984B temperature measurements. Open circles are original temperature measurements. Solid circles are calculated temperatures based on least-squares fits for the time interval (record numbers) chosen by the data analyst. Horizontal lines are calculated equilibrium temperatures based on least-squares fits. **A–M.** Downhole sediment temperature records and calculated equilibrium temperatures. **N.** Six bottom-water measurement records: five taken before Cores 162-984B-3H, 4H, and 6H through 8H were shot, and one taken before Hole 984D was spudded (thin continuous line). Horizontal dashed lines are calculated equilibration temperatures.

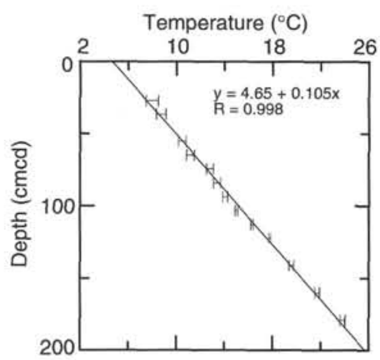

Figure 23. Downhole temperature gradient in Hole 984B.

Table 17. Calculated equilibration temperatures for bottom-water measurements from Hole 984B.

Core	Before coring (°C)	After coring (°C)
162-984B-		
3H	2.46	2.28
4H	2.60	2.67
6H	2.57	2.81
7H	2.88	2.70
8H	2.56	2.75

suspect that the combination of relatively warm water convecting up through the pipe and relatively cold bottom-water temperatures maintains a heat flux that retards temperature equilibration near the tool above the mudline.

In order to evaluate the potential effect of the borehole on bottom-water temperature measurements, we decided to take a 20-min bottom-water measurement before spudding Hole 984D (continuous line on Fig. 22N). There was no equilibration curve as seen with the equilibration records where the pipe was in the mud. Instead, the tool appeared to equilibrate immediately. During the first 10 min, a temperature of 2.72° ± 0.01°C was recorded, at which point a sudden drop to 2.67° ± 0.01°C occurred, which remained constant for another 10 min.

The lower temperatures calculated from the equilibration curves may be related to the lack of environmental corrections to the thermal conductivity values, or to inadequate geometrical parameters used to calculate equilibration temperatures. Our estimate of the bottom-water temperature is based on the dedicated measurement before spudding Hole 984D, with an error based on the range of calculated equilibrium temperatures, that is, 2.7° ± 0.1°C. This is in significant disequilibrium with the linearly extrapolated mudline temperature from the sediment of 4.65°C.

The preliminary results of this "high-resolution" heat-flow exercise do not indicate any significant anomaly in the sediment section between 28 and 180 mbsf, which could be related to Holocene bottom-water temperature changes. There are various potential reasons for this: the shallowest 28 m of sediment may contain an anomaly, given the steep gradient between the shallowest measurement and the bottom-water temperature, or there may not be an anomaly due to the oceanographic setting or relatively high heat-flow regime.

WIRELINE LOGGING

Operations

At Site 984, in Hole 984B, all three standard downhole logging tool strings were used. In addition, the Geological High-resolution Magnetometer (GHMT) tool was deployed (Table 18). The GHMT contains two sondes, one a nuclear resonance magnetometer (NRM) tool that measures Earth's total magnetic field strength, from which the remanent and induced components of the magnetic field can be extracted. The second sonde is the susceptibility magnetic tool (SUMT), which records the sediment magnetic susceptibility. Hole 984B was completed at ~503 mbsf (2163 mbrf) and the hole was conditioned by a "wiper trip" to remove drilling debris prior to logging. See the "Explanatory Notes" chapter (this volume) for a complete description of all tool strings and associated acronyms.

Hole conditions during logging were very good. No obstacles were encountered and ~0.5 to 3.5 m of drilling debris remained at the bottom of the hole during the wiper trip. All tools appeared to be operating properly except for the NRM tool of the GHMT tool string. The voltage control on the NRM tool seemed to be fluctuating abnor-

Table 18. Logged depth intervals in Hole 984B for Quad combo, FMS, GHMT, and GLT runs.

String	Run	Depth interval logged (mbsf)	Depth interval logged (mbrf)	Tools
Quad combo:	Down	100.0–500.0	1760.0–2160.0	NGT/SDT/CNT-G/HLDT/DIT/TLT
	Up	500.0–86.0	2160.0–1746.0	NGT/SDT/CNT-G/HLDT/DIT/TLT
	Up*	190.0–83.0	1850.0–1743.0	NGT/SDT/CNT-G/HLDT/DIT/TLT
Start time:	1200 hr			
Stop time:	1530 hr			
Logging speeds:	375 m/hr down log			
	275 m/hr up log			
(Mudline measured at 1660.4 mbrf with NGT)				
FMS:	Up	503.0–80.0	2163.0–1740.0	NGT/FMS/GPIT
	Up	500.0–83.0	2160.0–1743.0	NGT/FMS/GPIT
Start time:	1630 hr			
Stop time:	2030 hr			
Logging speed:	460 m/hr			
GHMT:	Up	501.0–81.0	2163.0–1740.0	NGT/GHMT
	Up*	240.0–140.0	1900.0–1800.0	NGT/GHMT
Start time:	2130 hr			
Stop time:	2345 hr			
Logging speed:	550 m/hr			
GLT:	Up	501.0–81.0	2161.0–1741.0	NGT/ACT/GST/TLT
	Up*	140.0–101.0	1800.0–1761.0	NGT/ACT/GST/TLT
Start time:	0105 hr			
Stop time:	0700 hr (included complete downrigging)			
Logging speed:	185 m/hr			
Wiper trip:	Hole conditioning prior to logging			
Start time:	0400 hr			
Stop time:	1130 hr			
Total logging time: 27 hr				
Estimated time: ~28–30 hr				

Notes: Depths are in meters below seafloor (mbsf) and meters below rig floor (mbrf). * = repeat section for quality control. NGT = Natural Gamma-ray Tool, SDT = Sonic Digital Tool (Array), CNT-G = Dual Porosity Compensated Neutron Tool, HLDT = High-temperature Litho-Density Tool, DIT = Phasor Dual Induction Tool, TLT = Lamont Temperature Tool, FMS = Formation MicroScanner, GPIT = General Purpose Inclinometry Tool, GHMT = Geological High-sensitivity Magnetic Tool, ACT = Aluminum Activation Tool, GLT = Geochemical Logging Tool.

mally but the repeat section of measurements was very consistent with the initial run. So, it may have had more to do with strong magnetic field readings obtained in this hole. Caliper data from both the Quad combo and FMS tool strings indicated that hole diameter varied between 30 and 35 cm over most of the hole. A few "washed out" zones in excess of 40 cm were limited to the interval between 100 to 150 mbsf. The bottom of the drilling pipe was set at 101 mbsf (1761 mbrf) and was raised 20 m to ~80 m during the uphole logging of all tools to allow for additional log measurements. The natural gamma-ray tool (NGT) was used to determine the mudline through the drill pipe during the last run with the geochemical tool string. The mudline was measured at ~1660.4 mbrf by running the NGT very slowly near estimated driller's depth and recording where a spike occurs when seawater was encountered. This mudline value was used to depth-shift all raw data from all four tool strings to mbsf from mbrf. The difference between driller's estimated depth (1660.6 mbrf) and mudline measurement (1660.4 mbrf) was only 0.2 m. Table 18 provides a complete summary of logging operations conducted at this site.

Core-to-Log Comparisons

Magnetic Susceptibility

The magnetic susceptibility log data obtained by the GHMT at this site correlates remarkably well with the magnetic susceptibility measured on the cores (Fig. 24). Every major event can be observed in both core and log data from Hole 984B, with the log data appearing as a smoothed version of core data due to its lower average sampling resolution (~20 cm). The magnetic susceptibility data sets apparently reflect Milankovitch-scale cycles (see "Sedimentation Rates" section, this chapter). They can also be used to calculate the amount of core expansion throughout the interval of log coverage (~90–503 mbsf). Depth offsets derived from comparisons of downhole and core magnetic data can be cross-checked with the downhole and core natural gamma-ray data. The downhole resistivity (SFLU) logs, which show a pattern mimicking the magnetic susceptibility log data, can also be used for this purpose.

Preliminary spectral analyses on both the core and downhole magnetic data were done using an age-vs.-depth curve derived from paleomagnetic and biostratigraphic datums (see "Paleomagnetism," "Sedimentation Rates," and "Biostratigraphy" sections, this chapter). The core and log magnetic data records were correlated with log depth as reference using the "Analys Series" software package and the output was used for the spectral analyses. Only the interval where both core and log data exist is discussed here. The analyses were separated into three sections where it appeared as sedimentation rates varied linearly across each section (see "Sedimentation Rates" section, this chapter). The results show cycles corresponding to precession and obliquity periods over interval from 90 to ~220 mbsf, followed by an interval (230–440 mbsf) where obliquity cycles are the dominant feature observed. Below 440 mbsf, in a mostly unrecovered interval, the precession cycles return along with the obliquity cycles. A significant change in the geochemical log data obtained by the geochemical logging tool (GLT) also shows the most variation in this 440–500-m interval, with less Ca and Fe and more Si, Al, and Th, possibly in response to different type of clay input.

Velocity

Sonic log data were collected over the interval of 87–478 mbsf using the longer 8-, 10-, and 12-ft transmitter-receiver spacings. In order to obtain continuous downhole estimates of seismic velocities for correlation with seismic reflection data, for comparison with core velocity measurements, and for computation of a synthetic seismogram, a provisional attempt was made to correct problems in data from source-receiver spacings. First, the raw borehole-compensated transit-time-series data were edited from the 12-ft and the two 10-ft source-receiver spacings to remove cycle skips and other unreason-

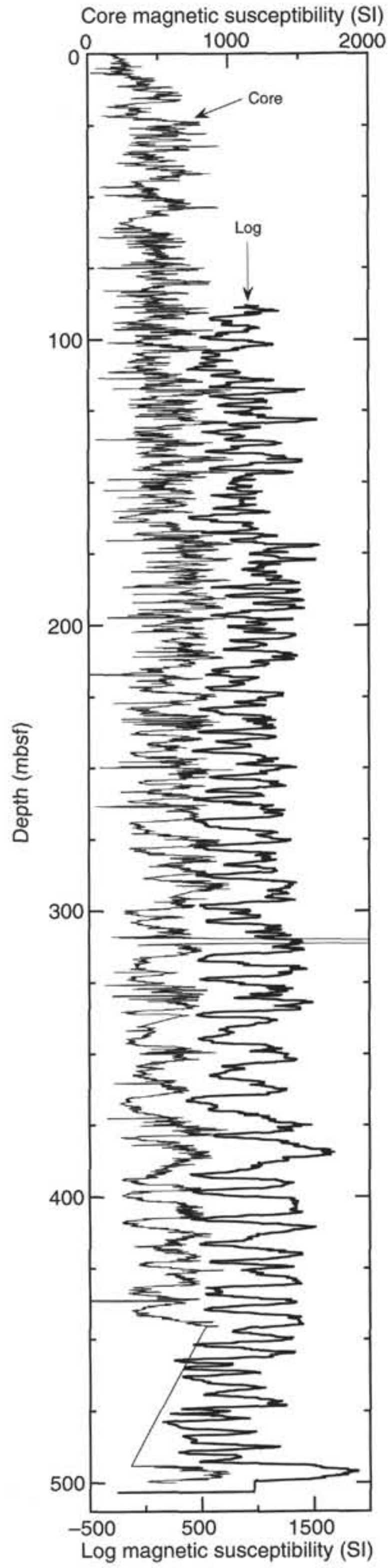

Figure 24. Comparison of log magnetic susceptibility data with MST magnetic susceptibility core measurements from Hole 984B. Depth scales for both data sets are given in meters below seafloor (mbsf). Seafloor depth measurements from both logs and drillers were within 0.5 m, so only a small depth correction had to be made in order to compare the data. No other downhole depth shifts were applied.

able abrupt offsets. Then, after these corrections were made, a new transit time series was calculated. Figure 25A shows a comparison of the recalculated log with the original DTLF, which is the transit-time data computed automatically during logging from the 10- and 12-ft spaced receivers. Eight different transit times are computed from differently spaced transmitter-receiver pairs.

The recalculated log shows a general steady decrease in transit time with depth, which is expected for such a uniform sedimentary succession. The transit times were converted into velocities and are shown in Figure 25B, together with laboratory velocity measurements from the same hole and an empirical velocity-vs.-depth function for deep-sea siliceous and turbidite sediments. The velocities on the recalculated sonic log are close to those predicted for siliceous sediments by the empirical function of Hamilton (1979), and at depths <300 m, they are considerably higher than the laboratory measurements. Below 300 m, both the laboratory and downhole velocity measurements show a marked increase, especially the laboratory data, and a much better cross-correlation. This 300-m boundary is also near the change from APC/XCB coring which indicates increased sediment induration. The *P*-wave logger and split-core velocities are very similar in cores down to 265 mbsf, where measurements taken by the *P*-wave logger were discontinued (see "Physical Properties" section, this chapter). It is expected that the seismic velocity measured in situ by logging should be significantly higher than laboratory measurements because of core expansion. Indeed, the velocity derived from the sonic log is approximately 5%–10% greater than that from core laboratory measurements at most depths <300 m.

There is a sharp velocity peak on the recalculated sonic log at 380–385 mbsf, reaching a peak velocity of greater than 2000 m/s in logs and almost 2200 m/s in the split core measurements. This peak occurs within the interval covered by Core 162-984B-41X, from which there was 94% recovery. The layer containing this velocity peak is interpreted as the source of Reflector R4 (see "Seismic Stratigraphy" section, this chapter). The cause of these high velocities observed in the core which correlate with the more highly resistive zones observed in FMS images is uncertain. The log shows velocities that are higher than background values over an interval of 4 to 5 m from 378 to 383 mbsf.

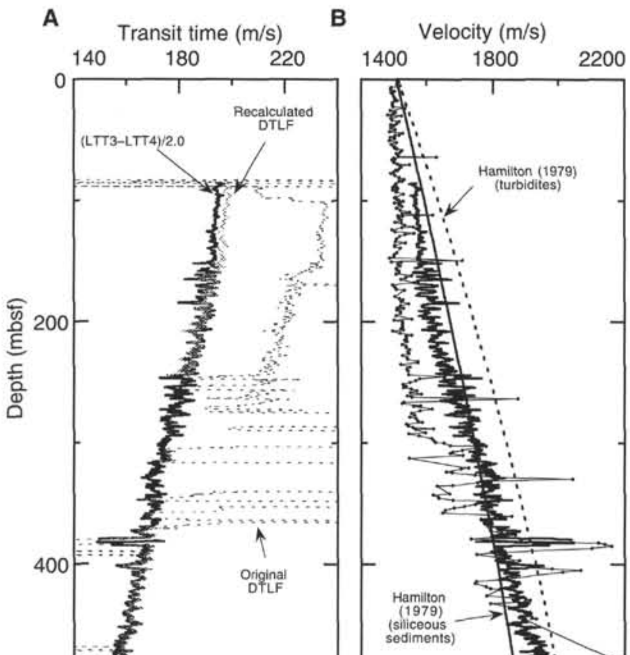

Figure 25. **A.** Comparison of original depth-derived, borehole-compensated sonic log (DTLF), computed during logging based on data from just the two most reliable source-receiver spacings (LTT3 and LTT4), with the same log recalculated after removal of spikes from the original transit-time data and provisional corrections for cycle skipping. Black line is LTT3 and LTT4 data, gray line is the recalculated log, and dashed line is the original log. **B.** Comparison of seismic velocities from recalculated sonic log with PWL velocity measurements on core samples (line with solid circles) and the empirical velocity-vs.-depth function for siliceous and turbidite deep-sea sediments from Hamilton (1979).

Density and Porosity

Bulk density and porosity data were collected by the Hostile-environment Litho-Density Tool (HLDT) and Compensated Neutron Tool (CNT), respectively, which are both run as part of the standard Quad combo. Measurements from the HLDT tool were collected in high-resolution mode at 2.5-cm spacing, which allows a vertical resolution of ~15–20 cm. The wireline log bulk density data are shown with laboratory GRAPE and gravimetric wet bulk density measurements (Fig. 26A). The downhole data show bulk densities mainly between 1.6 and 1.8 g/cm^3, increasing gradually with depth. The density log levels off to values averaging 1.8 g/cm^3 below 300 m. The high-velocity layer at 378–384 mbsf shows a modest increase (0.1 g/cm^3) in density up to ~1.9 g/cm^3.

The bulk density values on the wireline log are on average about 10% greater than the main trend of GRAPE bulk density measurements, whereas gravimetric wet bulk density measurements track the downhole data throughout the hole. Because we suspect an error in the absolute GRAPE density values (see "Explanatory Notes" chapter, this volume) and because we are more confident in the accuracy of the gravimetric data, we do not see a significant difference between laboratory and downhole measurements.

The compensated neutron tool (CNT) provides one estimate of downhole porosity (high-resolution thermal neutron porosity, or HTNP) by measuring the formation hydrogen-ion content. Downhole HTNP data are typically ~10% lower than porosity values calculated

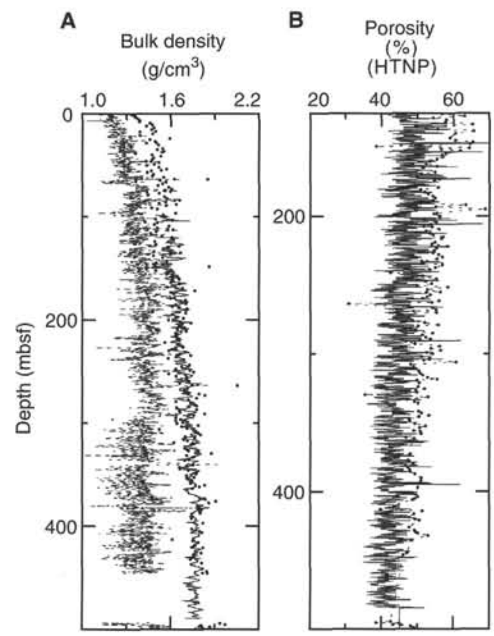

Figure 26. **A.** Comparison of downhole bulk density measurements (solid line) with GRAPE (dashed line) and gravimetric (solid circles) wet bulk density measurements. **B.** Comparison of wireline log porosity (solid line) and laboratory porosity from core sample measurements (solid circles) porosity measurements. HTNP = High-resolution thermal neutron porosity.

from moisture content measurements on core samples (Fig. 26B). Porosity values from cores may be too high due to core expansion but the magnitude of error, if any, is uncertain. The downhole log data from CNT, however, must also be corrected for chlorinity interferences that can reduce accuracy of hydrogen-ion measurement by a minimum estimate of ~5%. Another measurement of both hydrogen and chlorine is made with the geochemical tool which will help in evaluating accuracy of CNT data. Additional estimates of porosity from logging data can be made using a combination of sonic, resistivity, and lithodensity tool logs. As expected, the laboratory porosity in this fairly homogenous sequences decreases gradually with depth from 55%–64% at the top to 45%–50% at the bottom of the hole.

FMS Imaging

FMS imaging in Hole 984B revealed a finely layered, mostly homogenous sedimentary sequence with interspersed resistive layers. These layers could sometimes be related directly to ash layers observed in the core while others may be related to varying components within clays. One interval that stood out in both the log velocity and natural gamma-ray data and laboratory velocity measurements and FMS imaging in this hole was near seismic Reflector R4 (~380 mbsf) (see "Seismic Stratigraphy" section, this chapter). The FMS data from this interval, 378–385 mbsf, show a fairly thick layer, massive in appearance, and containing a number of large resistive zones (Fig. 27) (possibly clasts, 5–15 cm in diameter, and poorly defined layers, possibly cemented). The argument against clast interpretation is that no large clasts were recovered in the core covering this interval. High velocities were recorded on sediments in this section by both sonic logs and split-core measurements. A large thorium increase recorded by the natural gamma-ray log (Fig. 27) may indicate a change to a different clay type and source. This interval has been preliminarily interpreted as possibly (1) a zone of silica diagenesis, (2) an interval of varying clay-type deposition, and/or (3) some type of mass flow deposit. This deposit exhibits no obvious sedimentary structures. Layering within surrounding sediment can be observed above and below. Another prominent resistive layer observed in the FMS log at 368–372 mbsf corresponds to an increase in density and natural gamma-ray downhole logs. The interval near 380 mbsf also shows small but significant changes in density and photoelectric effect logs (Fig. 27), across this interval point to possibly due to varying degrees of silicification, cementation, and clay content across individual layers. The photoelectric log value was cross-plotted with a calculated Th (ppm)/K (wt%) ratio from the natural gamma-ray tool data. The Th/K ratio in this layer is >25 and, combined with a photoelectric value of 4–4.5, falls in the rather undiagnostic range of heavy thorium-bearing minerals.

Downhole Temperature Measurements

Borehole fluid temperature measurements were recorded in Hole 984B using the Lamont temperature logging tool (TLT). The TLT was run at the base of the Quad combo and GLT tool strings, which were the first and last logging runs, respectively. A downhole and an uphole profile were acquired during both runs. Figure 28 shows temperatures for the downhole and the uphole runs. A significant increase in bottom-hole temperature at 503 mbsf was observed during the ~14 hr between runs as the borehole equilibrated with the surrounding formation. The maximum recorded temperatures were 20.8°C (Quad combo run) and 36.5°C (GLT run), respectively. Extrapolation from APC temperature measurements, collected during coring of the upper portion of this hole, suggests that bottom-hole temperatures should be closer to ~50°C at this depth. Therefore, these values should be considered a minimum estimate and all temperature estimates should be interpreted with caution. No thermal anomalies were noted.

SEISMIC STRATIGRAPHY

As for Site 983 (GARDAR-1), the drilling proposal for the BJORN-1 site was based on a multichannel seismic line shot in 1993, EW-9302 Line 6b (Oppo et al., unpubl. data). The site survey was designed to duplicate this line and make a crossing line over BJORN-1 or another relevant site along the line. The 80-in.[3] water gun was used as a source and both the 3.5-kHz and 12-kHz PDR systems were run

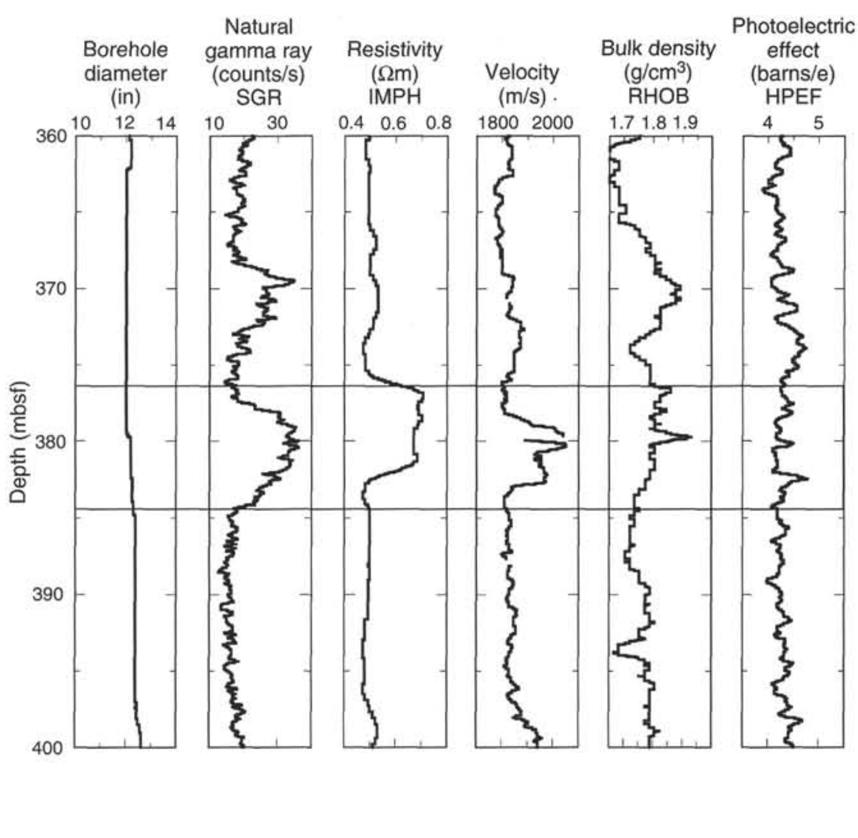

Figure 27. Wireline log physical property responses across highlighted zone encompassing interpreted Reflector R4 at depth of 377–385 mbsf. Note the lack of borehole deviation from original borehole size as exhibited by caliper data across this layer. SGR = spectroscopy gamma ray; IMPH = phasor medium induction; RHOB = standard bulk density; HPEF = high-resolution photoelectric effect.

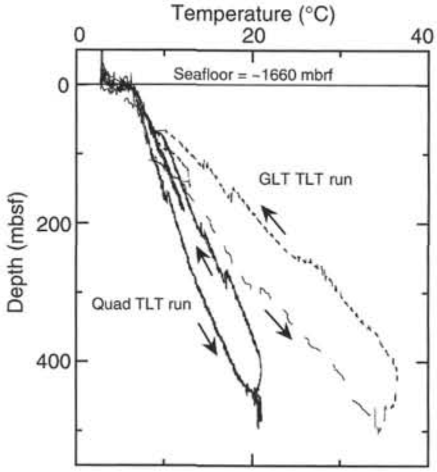

Figure 28. Borehole fluid temperature profiles recorded in Hole 984B using the Lamont temperature logging tool (TLT) on the first (Quad combo) and the last (GLT) logging runs separated by ~14 hr.

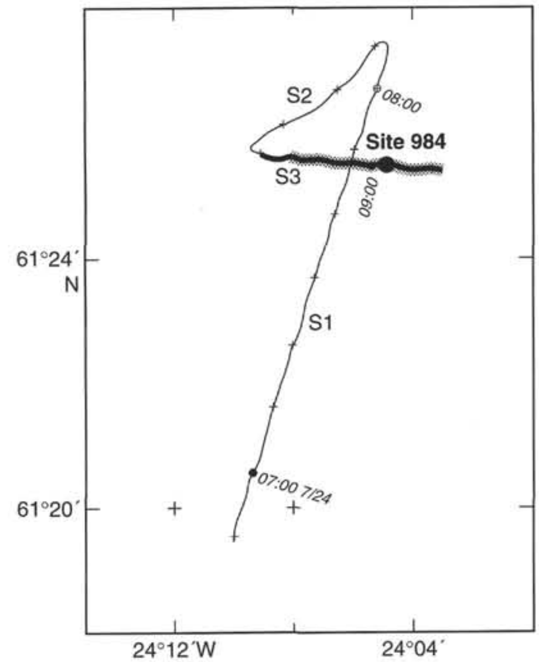

Figure 29. Map showing the site survey near Site 984. Bold black line and thick gray line mark the positions of the profiles shown in Figures 30 and 31, respectively.

during the survey (see "Explanatory Notes" section, chapter, this volume). Total survey length was 14 nmi (Fig. 29). After evaluation of the survey data, Site 984 was moved approximately 0.6 nmi to the east-northeast relative to proposed site BJORN-1. This was mainly based on the 3.5-kHz PDR data, which showed the upper 100 sediment layers to be thicker and less disturbed by small faults than at proposed site BJORN-1. Site 984 was drilled at a location corresponding to shotpoint 1000 of site survey Line S3 (Fig. 29). Interval velocities are estimated from the downhole logging velocities (see "Wireline Logging" section, this chapter).

Description of Seismic Stratigraphic Units

The seismic data acquired during the survey showed the area adjacent to Site 984 to have a sedimentary section of an approximate thickness of 0.8–0.9 seconds two-way traveltime (s TWT) above acoustic basement. Acoustic stratification is subconformable with the seafloor, and with the exception of an angular unconformity near the seafloor to the south of Site 984, no indications of major erosion are observed in the seismic sections (Fig. 30). As at Site 983, high-resolution 3.5-kHz PDR data were recovered to a depth of 0.11 s TWT below seafloor at the site (Fig. 31). Five seismic units (BJ-I to BJ-V) were defined, based on the combination of PDR and seismic data.

Seismic Unit BJ-I extends from the seafloor at 2.31 s TWT to Reflector R1 at 2.4 s TWT. Using an interval velocity of 1.54 km/s, this is equivalent to 69 mbsf. This unit is resolved in the 3.5-kHz PDR records, which show conformable internal stratification over the length of the site survey. More than 20 reflectors can be identified, some of which appear densely spaced (Fig. 31). The strata are disrupted by steep normal faults with a maximum observed displacement of 8 m (10 ms). Reflector R1 forms a strong reflector, and the closely spaced overlying reflectors appear to onlap or downlap onto it (Fig. 30).

Unit BJ-II is defined between Reflectors R1 and R3, the latter of which is at 2.65 s TWT at Site 984. Using an interval velocity of 1.6 km/s, the thickness of this unit is 203 m, with Reflector R3 at 272 mbsf (Fig. 32). This unit is characterized by acoustic stratification of relatively low amplitude, with some reflectors within the upper 0.1 s TWT of the unit being stronger and more densely spaced than those in the lower part of the unit. Reflector R2, the first clearly resolvable reflector below Reflector R1, is particularly prominent, but as it neither marks a change in seismic character nor an unconformity, it does not define a unit boundary.

Unit BJ-III extends from Reflector R3 to R4, at 2.79 s TWT. The average velocity within this unit is 1.76 km/s. Consequently, the thickness of the unit is 123 m and the depth of Reflector R4 is 395 mbsf. Unit BJ-III displays slightly more closely spaced, low-amplitude acoustic stratification than the unit above. A band of reflectors in the uppermost part of the unit at Site 984 is erosionally truncated by Reflector R3 approximately 2.5 km west of the site, along Line S3 (Fig. 30). However, no truncation can be observed at the site.

Seismic Unit BJ-IV differs from the unit above in having less densely spaced internal reflectors. Furthermore, Unit BJ-IV thins from approximately 120 m at Site 984, to 75 m in the western end of Line S3, using an interval velocity of 1.86 km/s. At Site 984, the base of the unit, Reflector R5, is estimated to be at 517 mbsf, that is, just below the bottom of Hole 984B at 504 mbsf. Furthermore, a somewhat more gradual, but still noticeable northward thinning of Unit BJ-IV is seen along Line S1. Hence, the unit seems to thin in a roughly northwestward direction through gradual thinning of individual strata, as no erosion is apparent in the unit.

Seismic Unit BJ-V, between Reflectors R5 and R6, is characterized by fewer distinct internal reflectors than the units above. The relief of the underlying Reflector R6, here defined as acoustic basement, is reflected in the wavy shape of the internal reflectors of Unit BJ-V. As this is below the drilled depth, there is no velocity information. Assuming a velocity of 2.2 km/s, based on the measured velocities in the lowermost core (162-984B-53X) (see "Physical Properties" section, this chapter), the thickness of the unit is approximately 280 m and Reflector R6 is at 790 mbsf. Weak, reflecting horizons are observed below Reflector R6, which may indicate the existence of volcanic extrusives within the acoustic basement of the area (Fig. 30).

Synthetic Seismogram

A synthetic seismogram was generated to facilitate correlation between seismic and lithostratigraphic units. The recalculated sonic log and edited density log from Hole 984B (see "Wireline Logging" sec-

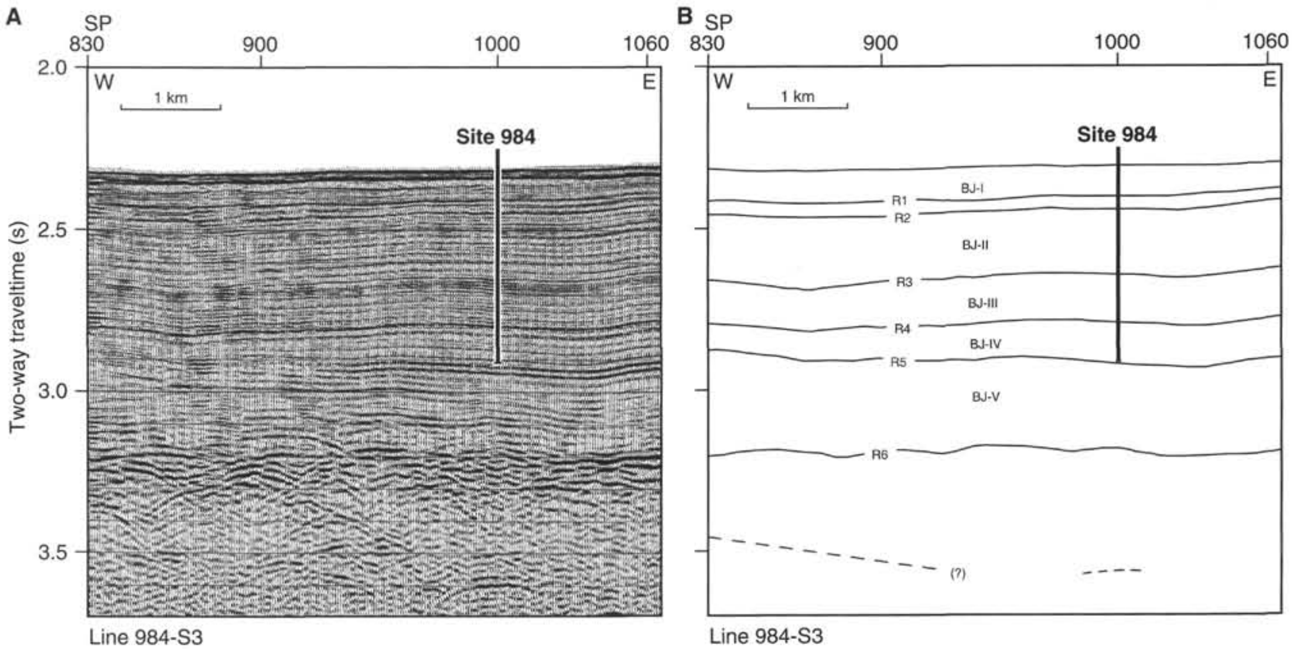

Figure 30. **A.** Seismic Line 984-S3. **B.** Interpretation of Line 984-S3, with seismic units and reflectors shown. See Figure 29 for location.

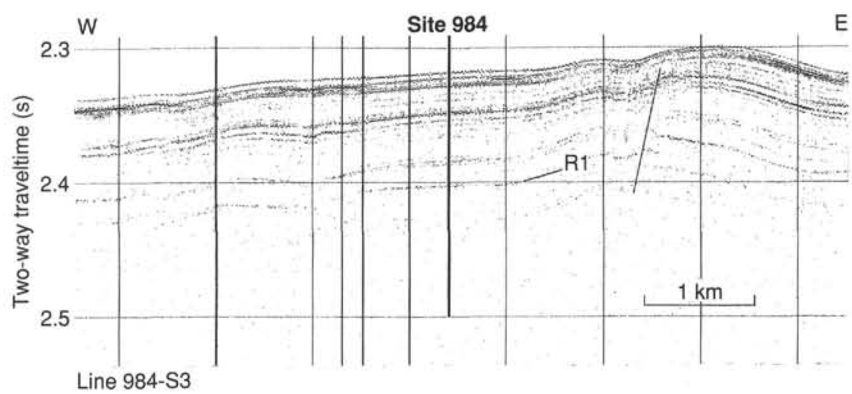

Figure 31. Sample of 3.5-kHz PDR record along Line 984-S3. Note the evenly spaced reflectors. See Figure 29 for location.

tion, this chapter) were used to calculate reflection coefficients below 98.7 mbsf. Discrete measurements of density and compressional velocity on the recovered cores (see "Physical Properties" section, this chapter) were used to calculate reflection coefficients above 98.7 mbsf. A water velocity of 1480 m/s and density of 1.03 g/cm^3 were assumed to calculate a reflection coefficient for the seafloor. Reflection coefficients were calculated as a function of both depth and TWT, to enable TWT on the synthetic seismogram to be related directly to depth (Fig. 33).

The bulk density values from the wireline log and the discrete measurements are similar near 98.7 mbsf, but the log velocities near this depth are 3.3% higher than those from measurements on the cores. To avoid generating a spurious reflection coefficient it was necessary to eliminate this step in velocity at the change from one type of data to the other. Two different methods of eliminating the step were tried: first, the discrete velocity measurements were multiplied by a constant and, second, a gain ramp was applied to the log velocities above 200 mbsf so that the velocity at 200 mbsf was unchanged while the velocity near 98.7 mbsf was reduced to match that obtained from discrete measurements. It was found that the latter method resulted in a better match between the TWTs of reflectors on the synthetic seismogram and the survey data, so this method was adopted for generation of the synthetic seismogram we present here.

The need to adjust the overall magnitude of velocities from the upper part of the recalculated sonic log may be explained by the fact that they were calculated using transit-time measurements from only two source-receiver pairs, and therefore are not borehole compensated (see "Wireline Logging" section, this chapter).

The seismic line used for correlation is Line 984-S3 of the Site 984 site survey. The seismic source signature of Line 984-S3 data was estimated by stacking the seafloor reflection on the 21 shots closest to Site 984 (see "Explanatory Notes" chapter, this volume). On the stacked trace, the first 58 ms after the start of the seafloor reflection were interpreted as representing the reflection of the source signature from the seafloor. These data were extracted and convolved with the reflection coefficient series (Fig. 33B) to produce the synthetic seismogram (Fig. 33C).

Figure 34 shows the synthetic seismogram inserted into Line 984-S3 at the location of the site. Most of the significant reflectors are clearly recognizable on the synthetic from their shape and amplitude. The close correspondence between the TWTs of reflectors on the synthetic seismogram and on the survey data confirms the accuracy of the velocity function used.

The origin of the TWT axis in Figure 33C is at the start of the initial trough of the seafloor reflection. All other TWTs reported in this chapter are measured from just before the onset of the first peak of

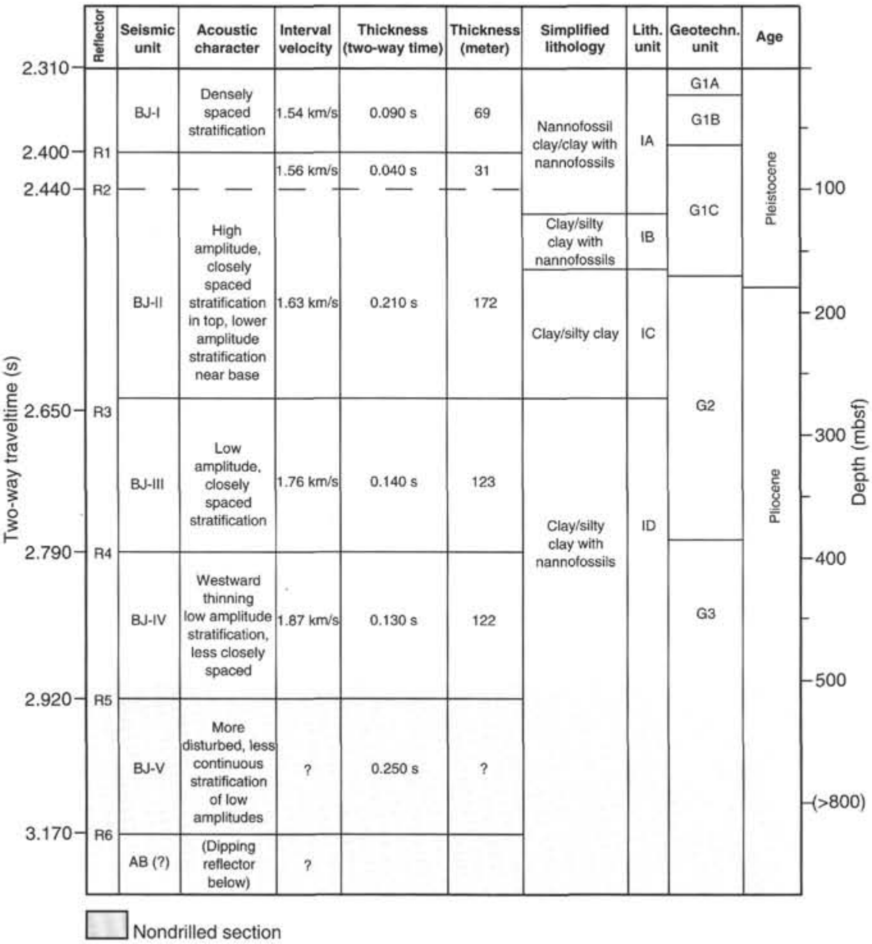

Figure 32. Relationships between seismic stratigraphy, lithostratigraphy, and geotechnical stratigraphy. The depth scale in mbsf is linear within the depths drilled, but note that the figure is not to scale below the drilled depth. AB = acoustic basement.

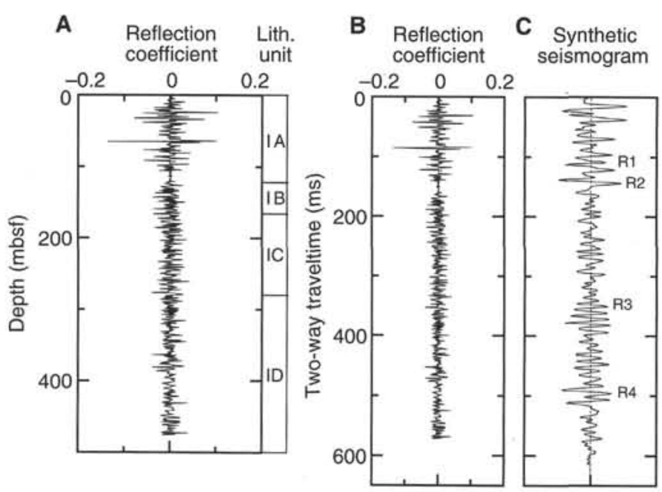

Figure 33. **A.** Reflection coefficients, calculated from log data (below 98.7 mbsf) and discrete measurements on cores (above 98.7 mbsf), plotted vs. depth. Also shown are the lithostratigraphic unit boundaries (see "Lithostratigraphy" section, this chapter). **B.** Reflection coefficients plotted vs. two-way traveltime. **C.** Synthetic seismogram plotted vs. two-way traveltime. Significant seismic reflectors, which have been identified by comparison with site survey Line 984-S3, are labeled on the synthetic seismogram.

the seafloor reflection, so the TWTs of all reflectors in Figure 33C have an apparent lag of 10 ms. The estimated seismic source signature contains two main peaks 16 and 39 ms after its start, with lower amplitude troughs before, between, and after these peaks. Therefore, the main seismic response to each reflection coefficient in Figure 33B is delayed by 16–39 ms. This is well illustrated by the large reflection amplitudes near Reflector R1, between 100 and 120 ms on the synthetic seismogram in Figure 33C. These large amplitudes are mainly a response to the large reflection coefficients between 85 and 88 ms, corresponding to depths of 64–66 mbsf. The fact that the largest positive and negative reflection coefficients are very close together in this interval causes a lot of destructive interference. If not for this, the amplitude of Reflector R1 would be much greater.

The large amplitude of Reflector R2, the peak of which is at 144 ms in Figure 33C, probably represents constructive interference between reflections from the boundaries represented by positive reflection coefficients at 108 and 129 ms, and the negative reflection coefficient at 122 ms. These reflection coefficients are at depths of 81–97 mbsf. A significant contribution to Reflector R3 (peak at 350 ms) is probably made by the positive reflection coefficient at 335 ms (261 mbsf), which is somewhat larger than the average for the deeper part of the hole. Directly below Reflector R3, we observe four more reflectors of similar amplitude with a regular 10-ms spacing between peaks. There does not appear to be a simple correspondence between these reflectors and individual reflection coefficients. Therefore, each of these reflectors is probably caused by constructive interference between reflections from several layer boundaries with small reflection coefficients. A possible cause of such regularly spaced and

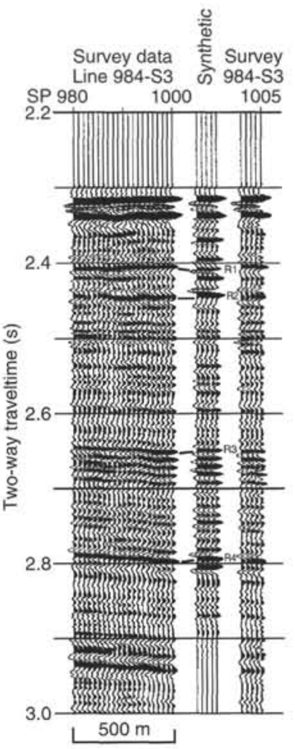

Figure 34. Part of site survey Line 984-S3 with five copies of the synthetic seismogram inserted at the location of Site 984.

relatively large amplitude reflectors is small, cyclic variations in velocity and density occurring at a wavelength that is strongly represented in the amplitude spectrum of the seismic source signature. This would cause resonance in the seismic reflection response. The average velocity in this interval is 1.76 km/s, so 10 ms represents 8.8 m. Reflector R4 (peak at 496 ms) cannot be simply explained by any large, discrete reflection coefficients and, therefore, it must also be an interference composite caused by a number of small reflection coefficients. In the interpretation of the survey data, the delayed seismic response has been accounted for by always marking the reflectors well above the first peak. Still, this may explain some discrepancies between core and seismic data.

Relationship to Core Data

The lithostratigraphy of Site 984 corresponds to that of Site 983 (see "Lithostratigraphy" section, this chapter). Only one lithostratigraphic unit is defined, with a subdivision in four subunits, IA to ID. The subdivision is based on changes in the spectral reflectance, the character of the magnetic susceptibility signal, and differences in the relative amount of clay, silty clay, and minor lithologies.

With few exceptions, the seismic stratigraphy does not correspond closely with the lithostratigraphy or geotechnical stratigraphy in the upper part of the drilled section. Reflector R1, however, is observed within 5 m of the boundary between geotechnical Subunits G1B and G1C, marked by an increase in *P*-wave velocities (see "Physical Properties" section, this chapter). The upper lithostratigraphic Subunit IA corresponds to seismic Unit BJ-I and the upper part of Unit BJ-II (Fig. 32). The boundary between lithostratigraphic Subunits IA and IB is placed at 120 mbsf, approximately 20 m below Reflector R2, which is a prominent internal reflector within seismic Unit BJ-II. As at Site 983, the methane concentration increases abruptly below 100 mbsf, that is, near the level of Reflector R2 (see "Inorganic Geochemistry" and "Organic Geochemistry" sections, this chapter).

Only the boundary between lithostratigraphic Subunits IC and ID shows a good correspondence with a seismic unit boundary, Reflector R3, at approximately 280 mbsf (Fig. 32). The need to change from APC to XCB coring at 295 mbsf indicates that a likely cause for the seismic reflector is an increase in the degree of induration of the sediments. This is supported by the increase in *P*-wave velocities at the boundary between geotechnical Units G5 and G6 (see "Physical Properties" section, this chapter). Above this level, the measured velocities show only a slight increase with depth, whereas below about 295 mbsf, the variations are high and the velocity gradient steeper. A likely explanation is that cementation in the lower part of Unit G2 and below prevents core expansion during recovery and that the measured velocities above Reflector R3 are too low. This explanation is also supported by a comparison between velocities measured by the downhole logging tools and the laboratory measurements (see "Wireline Logging" and "Physical Properties" sections, this chapter).

Both laboratory and downhole logging velocity measurements show two short (2–3-m) intervals of high velocities around 400 mbsf. This corresponds to Reflector R4, a prominent seismic unit boundary. The downhole Formation MicroScanner (FMS) as well as the resistivity logs also detected distinct changes at the same level, probably due to the presence of indurated beds. Furthermore, pore-water geochemistry indicate increased ossification of the sediments at this level (see "Inorganic Geochemistry" section, this chapter).

While coring apparently terminated above seismic Unit BJ-V, both increased *P*-wave velocities (see "Physical Properties" section, this chapter) and an increase in recovery in the lowermost core after 50 m of nonrecovery (see "Operations" section, this chapter), indicates that a change in sediment character had occurred. Given uncertainties in both estimating interval velocities and in picking the exact position of the reflector, it is possible that the bottom of Hole 984B penetrated the level corresponding to Reflector R5.

In summary, the comparison between seismic stratigraphy and core data shows that for sediments drilled at Site 984, as well as at Site 983, the most distinct changes causing acoustic impedance contrasts are related to cementation. The subtle and gradational changes in both lithology and seismic character in the uppermost 400 and 200 m of sediment at both sites, respectively, results in a relatively high degree of uncertainty in depth assignments of unit boundaries.

The seismic section shows no apparent unconformities at Site 984. Most strata are conformable over the length of the seismic survey, and unit thicknesses do not vary. An exception from this trend, is the northwestward thinning of Unit BJ-IV.

REFERENCES

Baldauf, J.G., 1984. Cenozoic diatom biostratigraphy and paleoceanography of the Rockall Plateau region, North Atlantic, Deep Sea Drilling Project Leg 81. *In* Roberts, D.G., Schnitker, D., et al., *Init. Repts. DSDP,* 81: Washington (U.S. Govt. Printing Office), 439–478.

Berggren, W.A., Hilgen, F.J., Langereis, C.G., Kent, D.V., Obradovich, J.D., Raffi, I., Raymo, M.E., and Shackleton, N.J., 1995. Late Neogene chronology: new perspectives in high-resolution stratigraphy. *Geol. Soc. Am. Bull.,* 107:1272–1287.

Bond, G., Broecker, W., Johnsen, S., McManus, J., Labeyrie, L., Jouzel, J., and Bonani, G., 1993. Correlations between climate records from the North Atlantic sediments and Greenland ice. *Nature,* 365:143–147.

Bond, G., Heinrich, H., Broecker, W., Labeyrie, L., McManus, J., Andrews, J., Huon, S., Janitschik, R., Clasen, S., Simet, C., Tedesco, K., Klas, M., Bonani, G., and Ivy, S., 1992. Evidence for massive discharge of icebergs into the North Atlantic ocean during the last glacial period. *Nature,* 360:245–249.

Bond, G.C., and Lotti, R., 1995. Iceberg discharges into the North Atlantic on millennial time scales during the last glaciation. *Science,* 276:1005–1010.

Boyle, E.A., and Keigwin, L.D., 1987. North Atlantic thermohaline circulation during the past 20,000 years linked to high-latitude surface temperature. *Nature,* 330:35–40.

Broecker, W.S., 1994. Massive iceberg discharges as triggers for global climate change. *Nature,* 372:421–424.

Davies, T.A., and Laughton, A.S., 1972. Sedimentary processes in the North Atlantic. *In* Laughton, A.S., Berggren, W.A., et al., *Init. Repts. DSDP,* 12: Washington (U.S. Govt. Printing Office), 905–934.

Fronval, T., Jansen, E., Bloemendal, J., and Johnsen, S., 1995. Oceanic evidence for coherent fluctuations in Fennoscandian and Laurentide ice sheets on millennium timescales. *Nature,* 374:443–446.

Gieskes, J.M., 1981. Deep-sea drilling interstitial water studies: implications for chemical alteration of the oceanic crust, layers I and II. *In* Warme, J.E., Douglas, R.G., and Winterer, E.L. (Eds.), *The Deep Sea Drilling Project: A Decade of Progress.* Spec. Publ.—Soc. Econ. Paleontol. Mineral., 32:149–167.

Hamilton, E.L., 1979. Sound velocity gradients in marine sediments. *J. Acoust. Soc. Am.,* 65:909–922.

Heinrich, H., 1988. Origin and consequences of cyclic ice rafting in the northeast Atlantic Ocean during the past 130,000 years. *Quat. Res.,* 29:142–152.

Imbrie, J., Boyle, E.A., Clemens, S.C., Duffy, A., Howard, W.R., Kukla, G., Kutzbach, J., Martinson, D.G., McIntyre, A., Mix, A.C., Molfino, B., Morley, J.J., Peterson, L.C., Pisias, N.G., Prell, W.L., Raymo, M.E., Shackleton, N.J., and Toggweiler, J.R., 1992. On the structure and origin of major glaciation cycles, 1. Linear responses to Milankovitch forcing. *Paleoceanography,* 7:701–738.

————, 1993. On the structure and origin of major glaciation cycles, 2. The 100,000-year cycle. *Paleoceanography,* 8:699–736.

Locker, S., and Martini, E., 1989. Cenozoic silicoflagellates, ebridians, and actiniscidians from the Vøring Plateau (ODP Leg 104). *In* Eldholm, O., Thiede, J., Taylor, E., et al., *Proc. ODP, Sci. Results,* 104: College Station, TX (Ocean Drilling Program), 543–585.

MacAyeal, D., 1993. Binge/purge oscillations of the Laurentide ice sheet as a cause of the North Atlantic's Heinrich events. *Paleoceanography,* 8:775–795.

McCartney, M.S., 1992. Recirculating components to the deep boundary current of the northern North Atlantic. *Prog. Oceanogr.,* 29:283–383.

Okada, H., and Bukry, D., 1980. Supplementary modification and introduction of code numbers to the low-latitude coccolith biostratigraphic zonation (Bukry, 1973; 1975). *Mar. Micropaleontol.,* 5:321–325.

Oppo, D.W., and Lehman, S.J., 1993. Mid-depth circulation of the subpolar North Atlantic during the last glacial maximum. *Science,* 259:1148–1152.

Rahmstorf, S., 1994. Rapid climate transitions in a coupled ocean-atmosphere model. *Nature,* 372:82–85.

Robinson, S., and McCave, I., 1994. Orbital forcing of bottom-current enhanced sedimentation on Feni Drift, NE Atlantic, during the mid-Pleistocene. *Paleoceanography,* 9:943–971.

Saltzman, B., and Verbitsky, M., 1994. Late Pleistocene climatic trajectory in the phase space of global ice, ocean state, and CO_2: observations and theory. *Paleoceanography,* 9:767–779.

Weaver, A.J., and Hughes, T.M.C., 1994. Rapid interglacial climate fluctuations driven by North Atlantic ocean circulation. *Nature,* 367:447–450.

Weaver, P.P.E., and Clement, B.M., 1986. Synchroneity of Pliocene planktonic foraminiferal datums in the North Atlantic. *Mar. Micropaleontol.,* 10:295–307.

Wold, C., 1994. Cenozoic sediment accumulation on drifts in the northern North Atlantic. *Paleoceanography,* 9:917–941.

Ms 162IR-106

Note: For all sites drilled, core description forms ("barrel sheets") and core photographs can be found in Section 3, beginning on page 391. Forms containing smear slide data can be found in Section 4, beginning on page 1147. All processed logs (including FMS, dipmeter, temperature data, high-resolution density and neutron data, and sonic waveforms not shown in printed form) are on the CD-ROM enclosed in the back pocket of this volume. Also on the CD-ROM are all tables from this chapter (including an extended coring summary table) and shipboard measurements (files containing GRAPE density, *P*-wave velocity, natural gamma radiation, magnetic susceptibility, index properties, and spectral reflectance data.).

SHORE-BASED LOG PROCESSING

Hole 984B

Bottom felt: 1659 mbrf
Total penetration: 503.7 mbsf
Total core recovered: 458.3 m (91%)

Logging Runs

Logging string 1: DIT/SDT/HLDT/CNTG/NGT
Logging string 2: FMS/GPIT/NGT
Logging string 3: GHMT/NGT
Logging string 4: ACT/GST/NGT
Wireline heave compensator was used to counter ship's heave.

Bottom-hole Assembly

The following bottom-hole/pipe/casing assembly (BHA) depths are as they appear on the logs after differential depth shift (see "Depth shift" section below) and depth shift to the seafloor. As such, there might be a discrepancy with the original depths given by the drillers on board. Possible reasons for depth discrepancies are ship's heave, use of wireline heave compensator, and drill-string and/or wireline stretch.

DIT/SDT/HLDT/CNTG/NGT: BHA at ~85 mbsf.
FMS/GPIT/NGT: BHA at ~107 mbsf.
GHMT/NGT: BHA at ~85 mbsf.
ACT/GST/NGT: BHA at ~85 mbsf.

Processing

Depth shift: Original logs have been interactively depth shifted with reference to NGT from ACT/GST/NGT run and to the seafloor (1660.5 m). Note that the depth of the seafloor as seen on the logs differs from the bottom felt depth given by the drillers (+1.5 m).

Gamma-ray processing: Data have been processed to correct for borehole size and type of drilling fluid.

Acoustic data processing: The array sonic tool was operated in standard depth-derived borehole compensated mode including long-spacing (8–10–10–12 ft) logs. The logs have been processed to eliminate some of the noise and cycle skipping experienced during the recording.

Geochemical processing: For detailed explanation of the processing, please refer to the "Explanatory Notes" chapter (this volume) or to the "geochem.doc" file on the CD-ROM (back pocket).

List of oxide factors used in geochemical processing:
SiO_2 = 2.139
$CaCO_3$ = 2.497
FeO* = 1.358
TiO_2 = 1.668
K_2O = 1.2052
Al_2O_3 = 1.889
FeO* = computed using an oxide factor which assumes a 50:50 combination of Fe_2O_3 and FeO factors.

Quality Control

Data recorded through the bottom-hole assembly, such as gamma-ray and neutron porosity data recorded above 85 mbsf, should be used qualitatively only because of the attenuation on the incoming signal. Invalid gamma-ray spikes were recorded at 69.5–78 mbsf.

Hole diameter was recorded by the hydraulic caliper on the HLDT tool (CALI) and the caliper on the FMS string (C1 and C2).

FACT = quality control curve in geochemical processing. Accuracy of the estimates is inversely proportional to the magnitude of the curve.

Note: Details of standard shore-based processing procedures are found in the "Explanatory Notes" chapter (this volume). For further information about the logs, please contact:

Cristina Broglia
Phone: 914-365-8343
Fax: 914-365-3182
E-mail: chris@ldeo.columbia.edu

Elizabeth Pratson
Phone: 914-365-8313
Fax: 914-365-3182
E-mail: beth@ldeo.columbia.edu

Hole 984B: Natural Gamma Ray-Resistivity-Sonic Logging Data

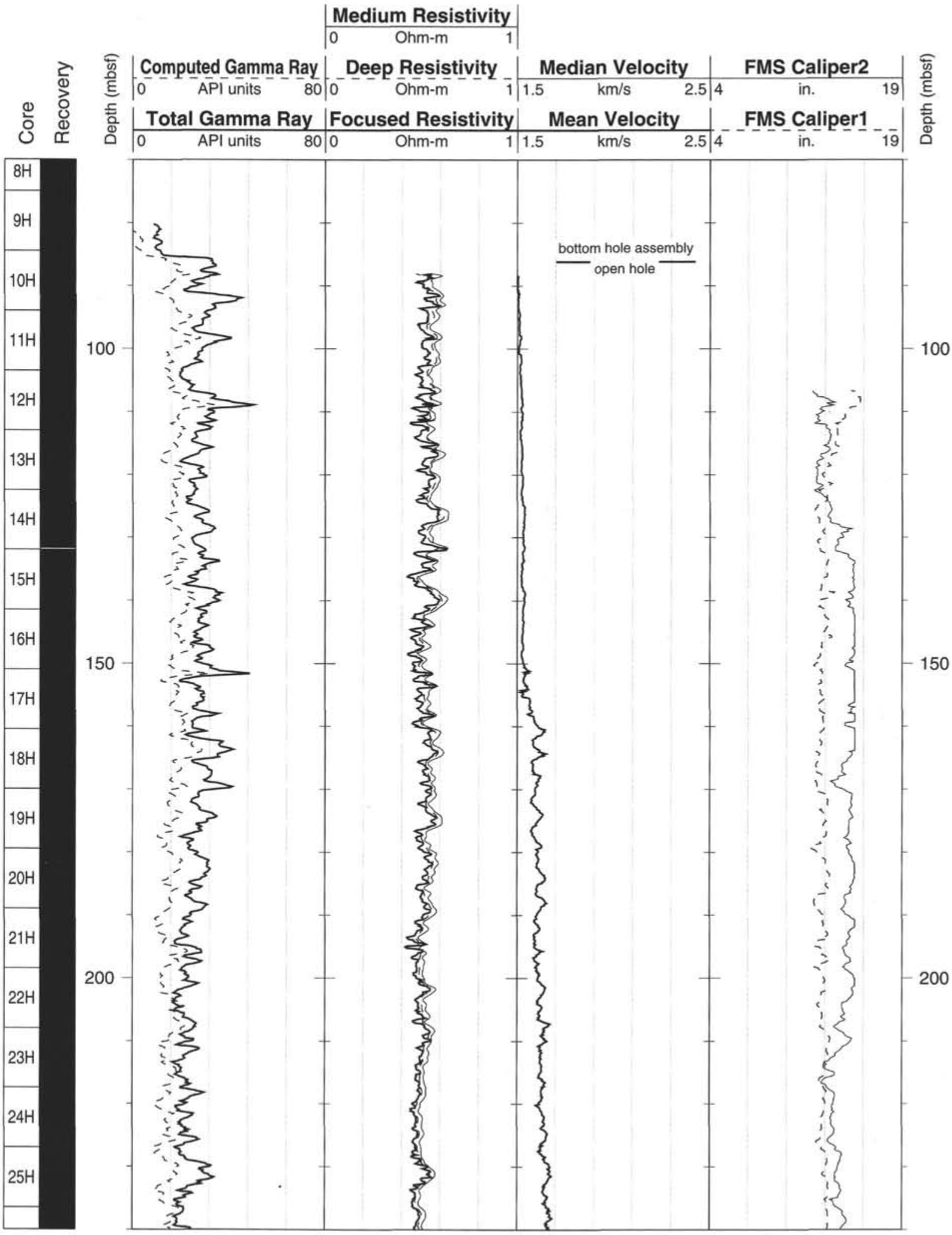

Hole 984B: Natural Gamma Ray-Resistivity-Sonic Logging Data (cont.)

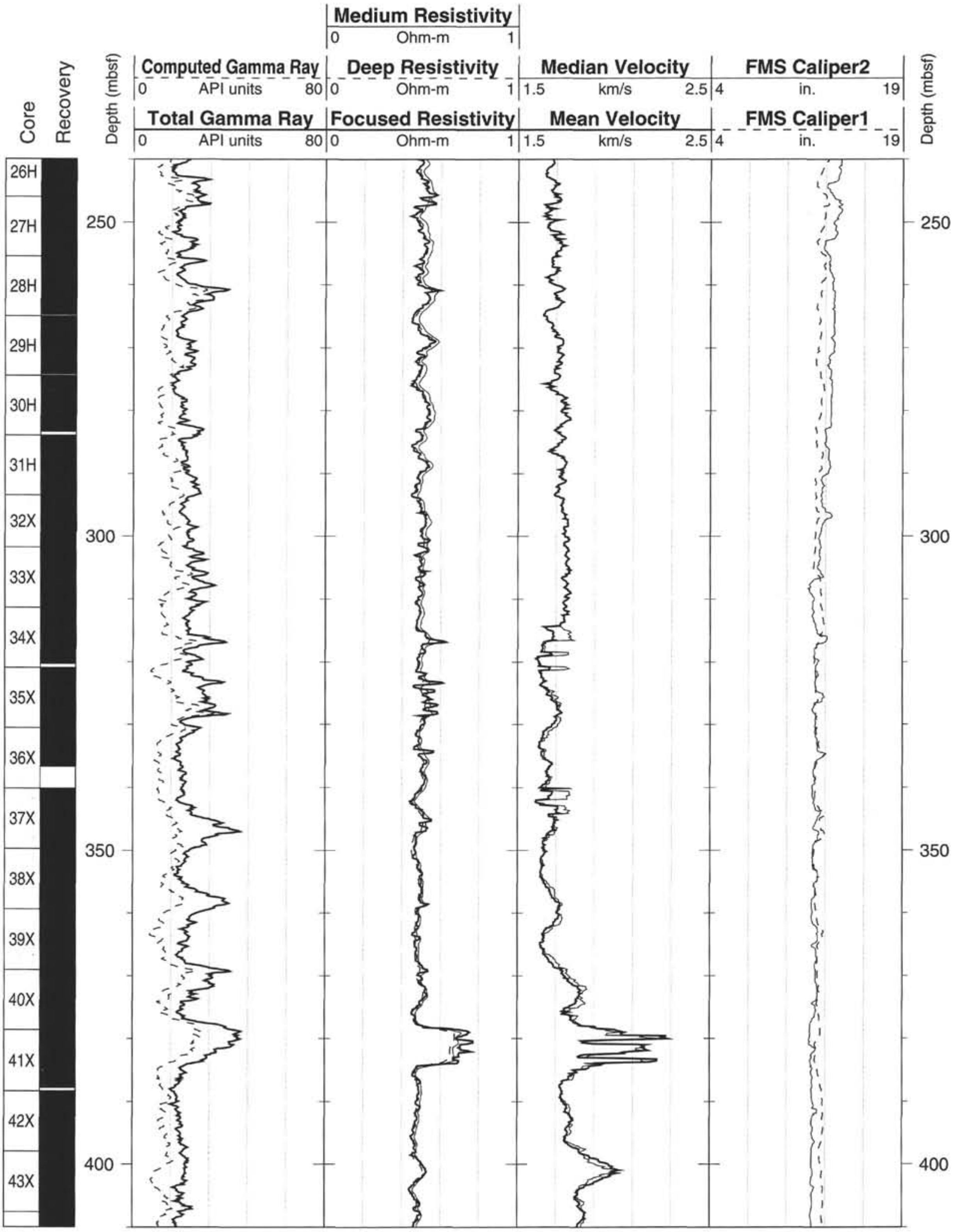

Hole 984B: Natural Gamma Ray-Resistivity-Sonic Logging Data (cont.)

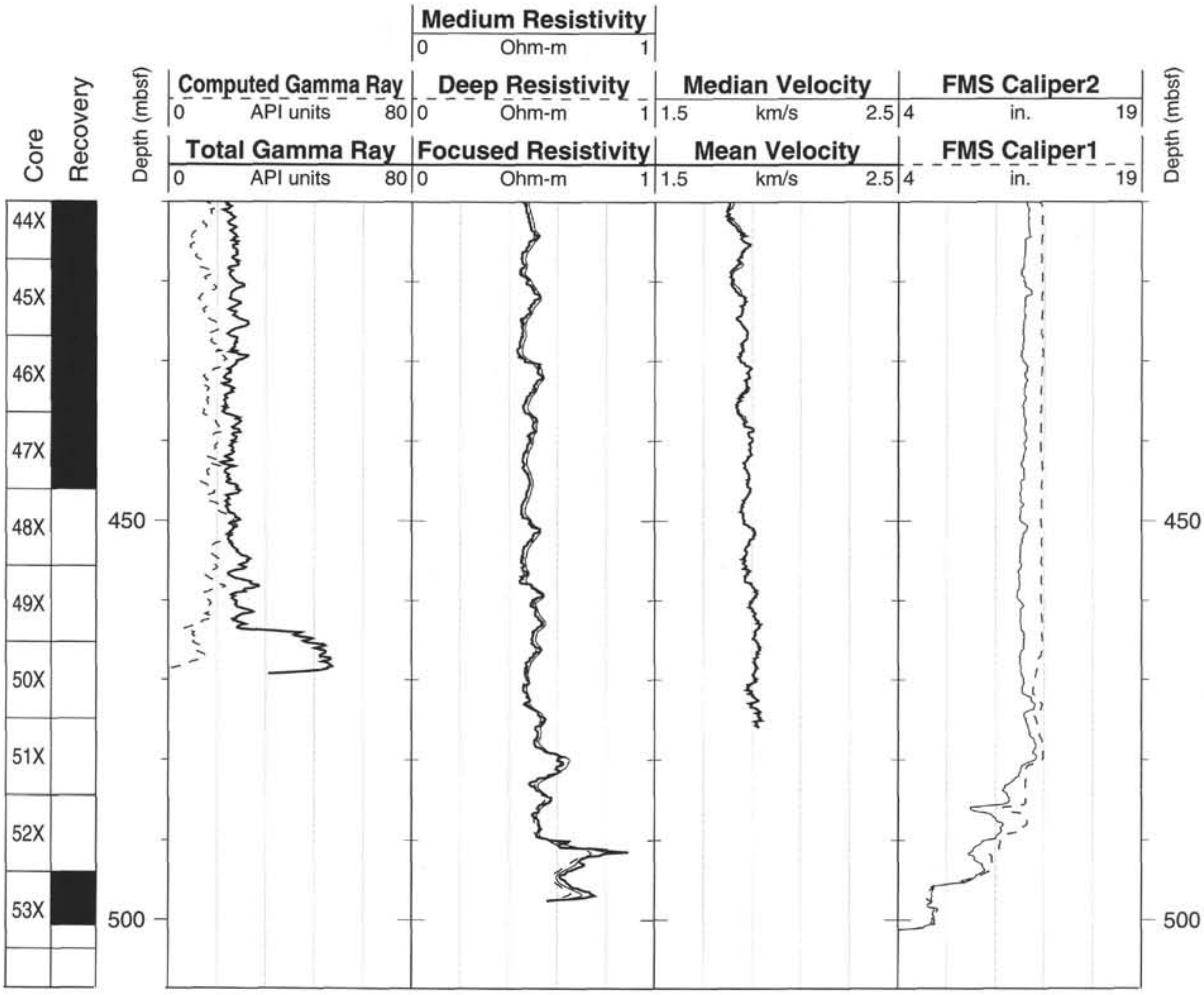

Hole 984B: Natural Gamma Ray Logging Data

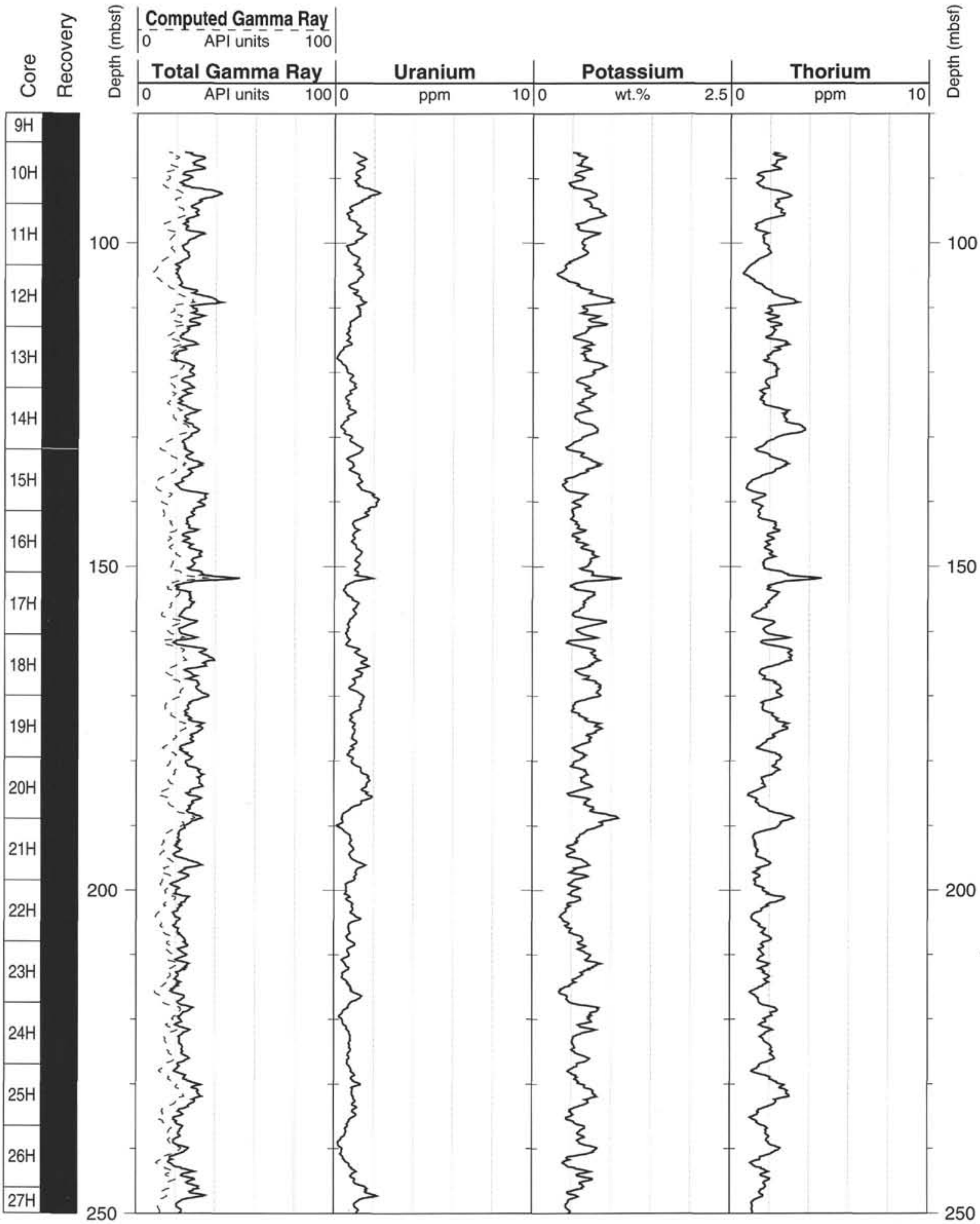

Hole 984B: Natural Gamma Ray Logging Data (cont.)

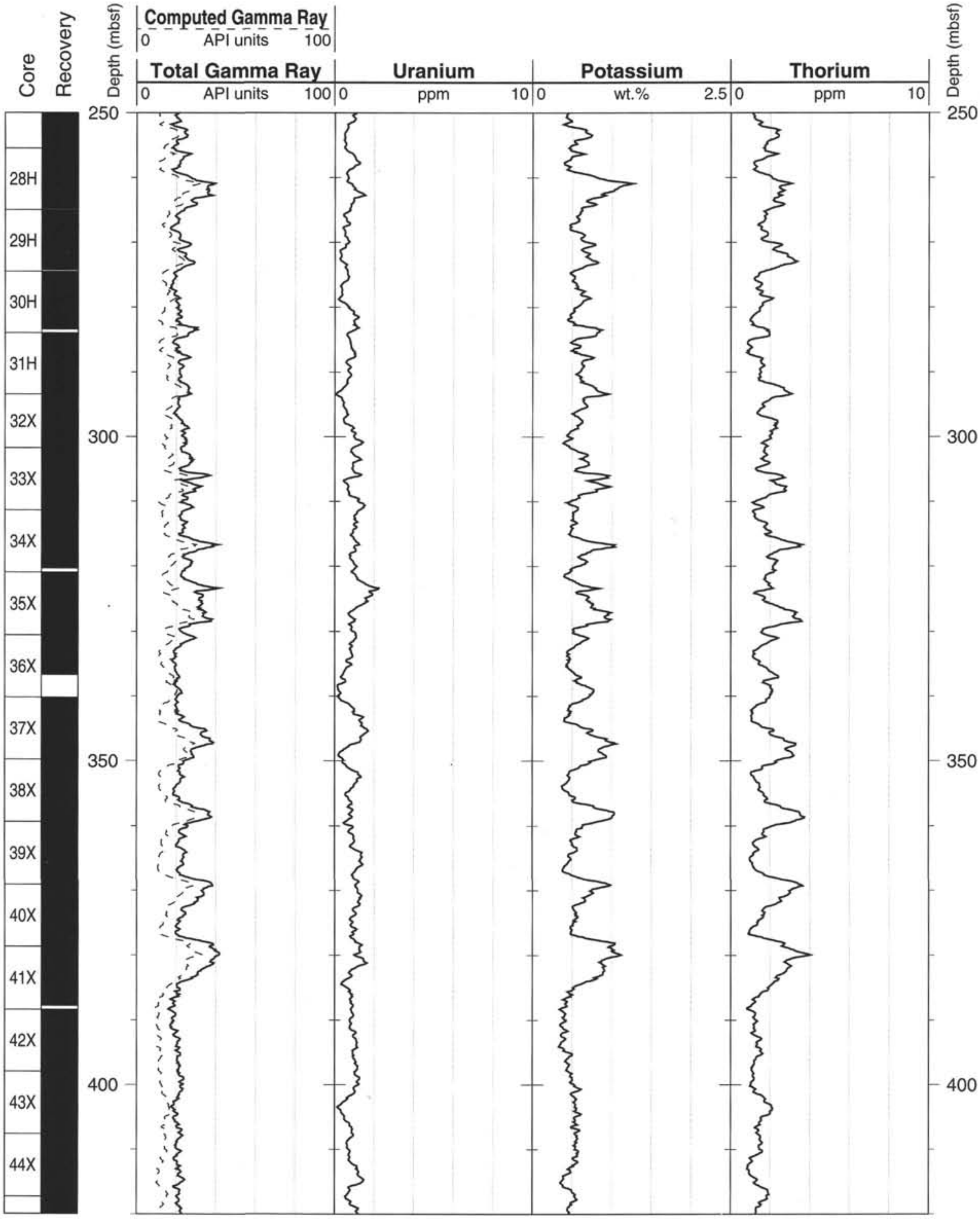

Hole 984B: Natural Gamma Ray Logging Data (cont.)

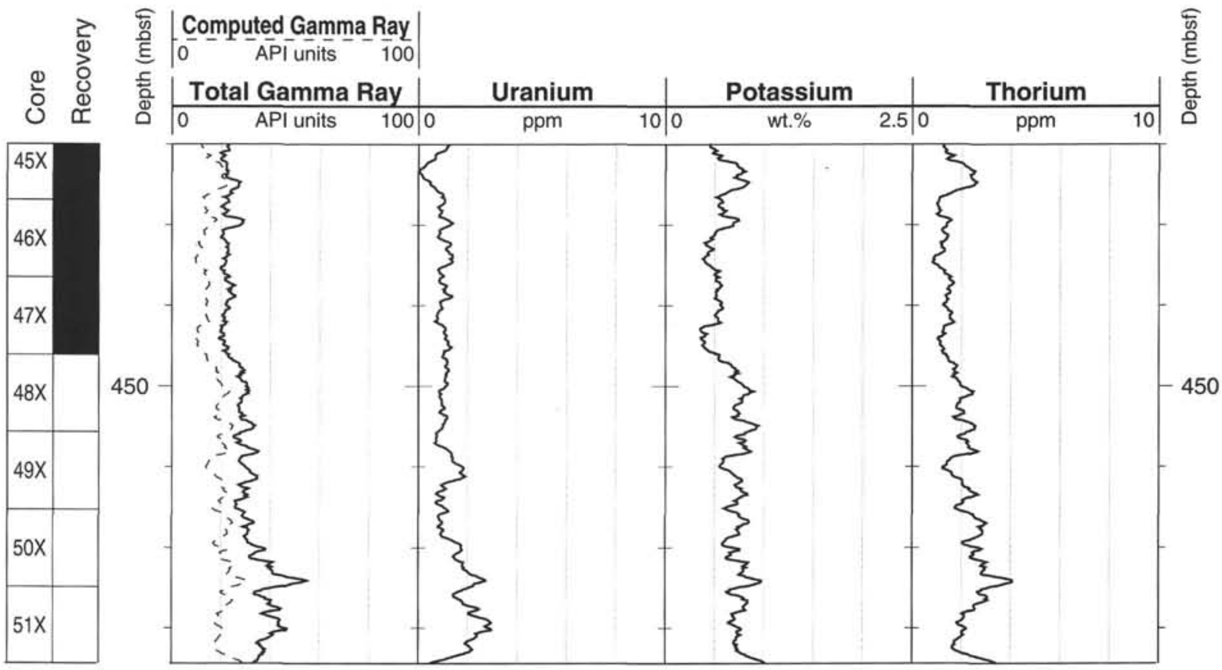

Hole 984B: Natural Gamma Ray-Density-Porosity Logging Data

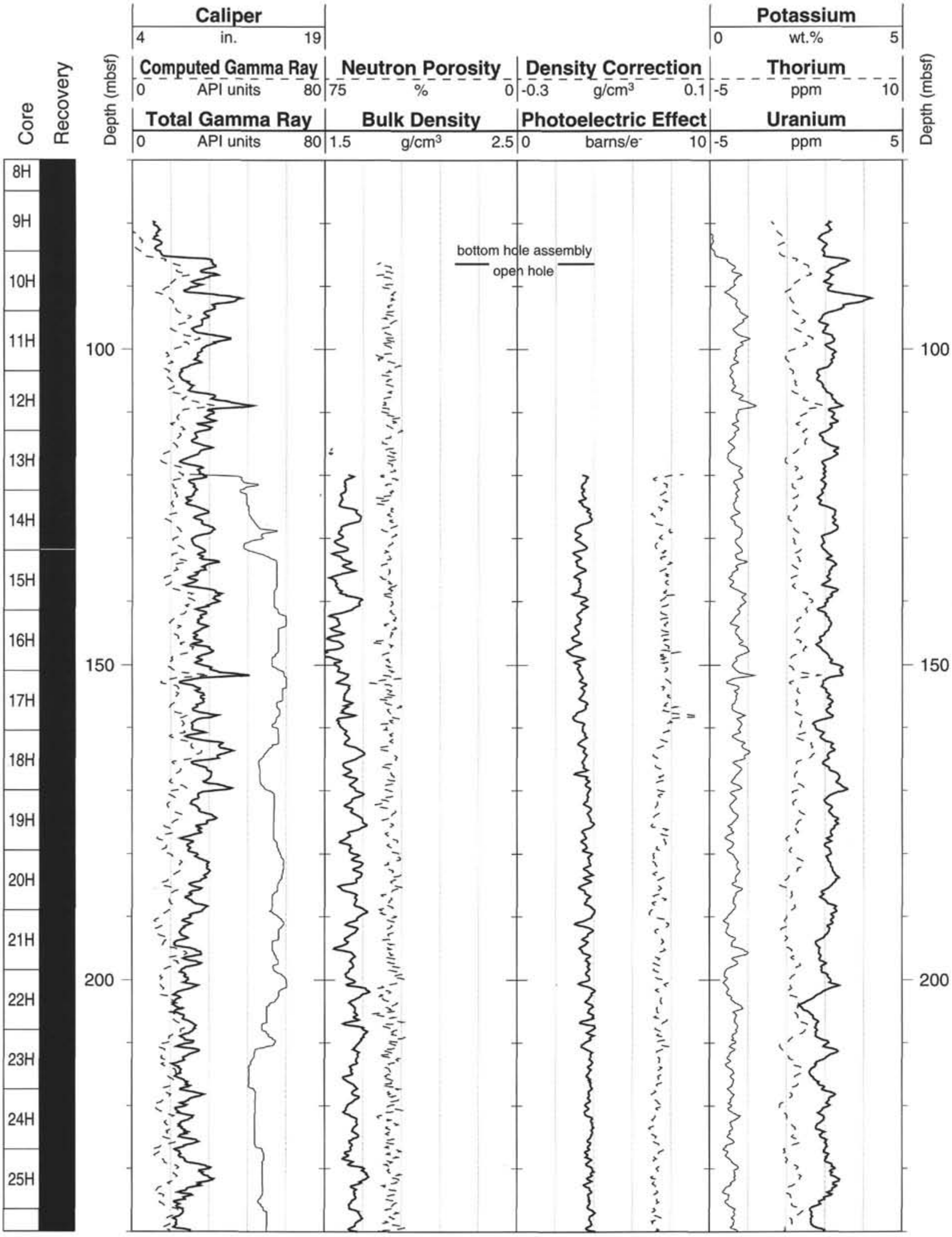

Hole 984B: Natural Gamma Ray-Density-Porosity Logging Data (cont.)

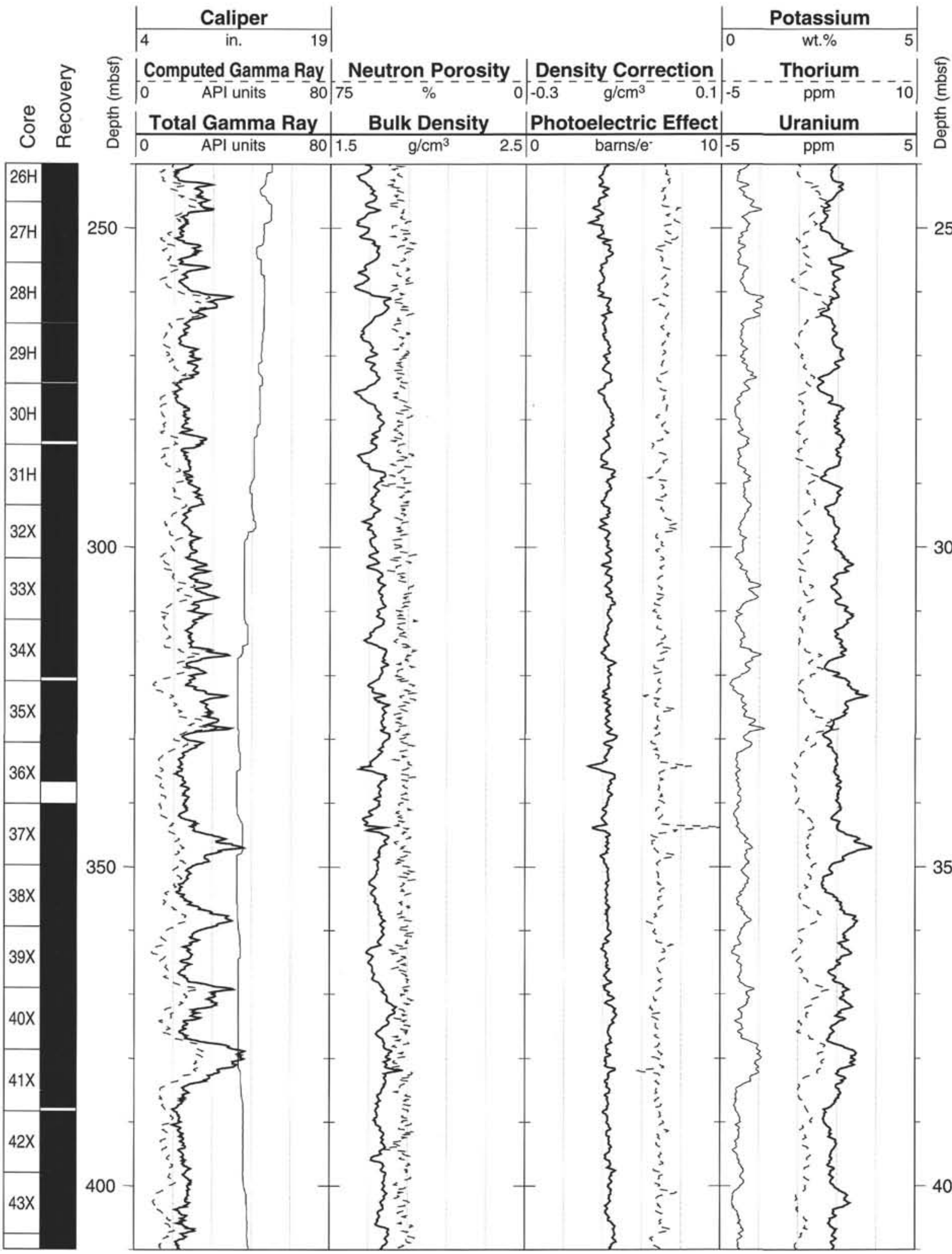

Hole 984B: Natural Gamma Ray-Density-Porosity Logging Data (cont.)

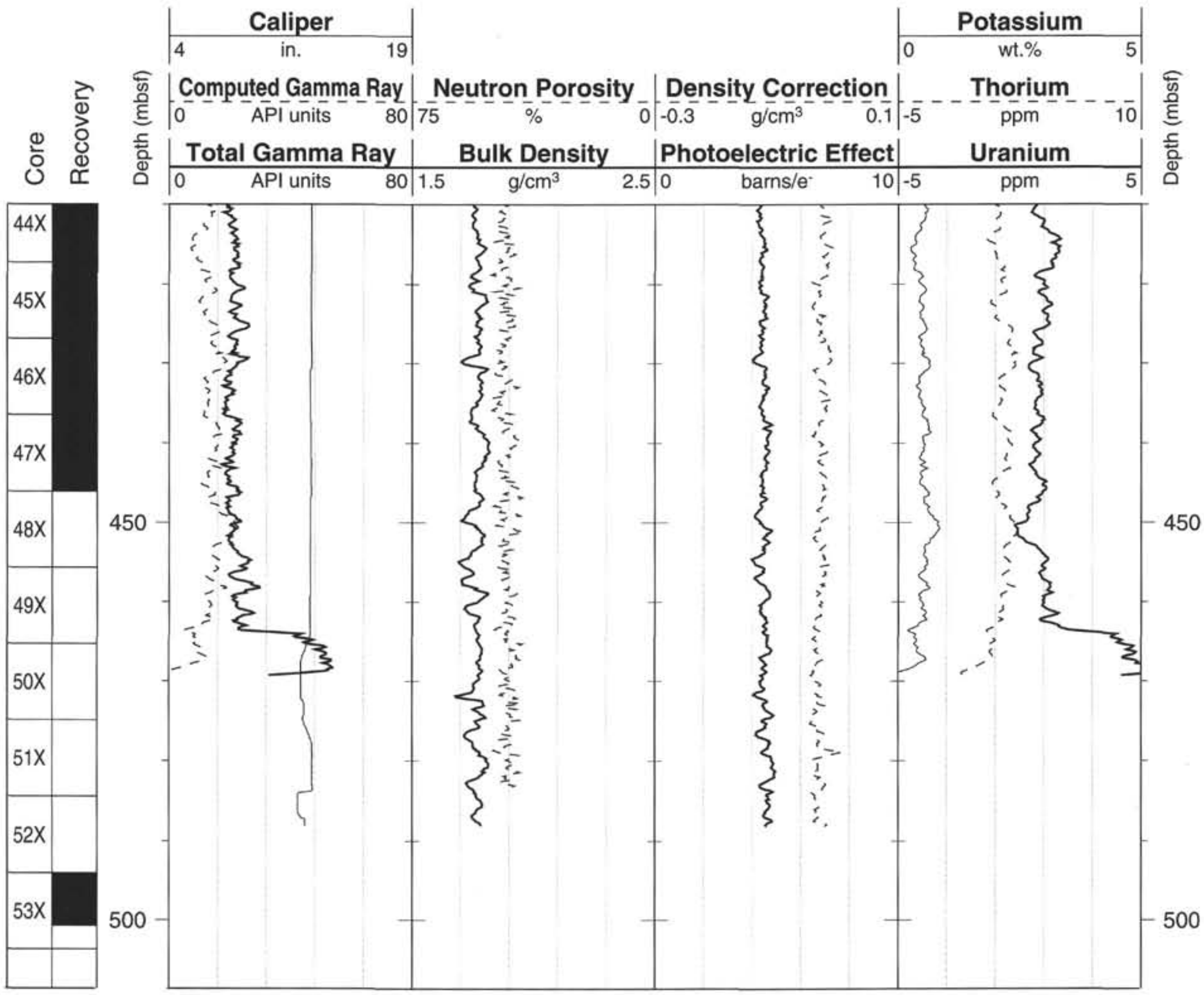

Hole 984B: Geochemical Logging Data

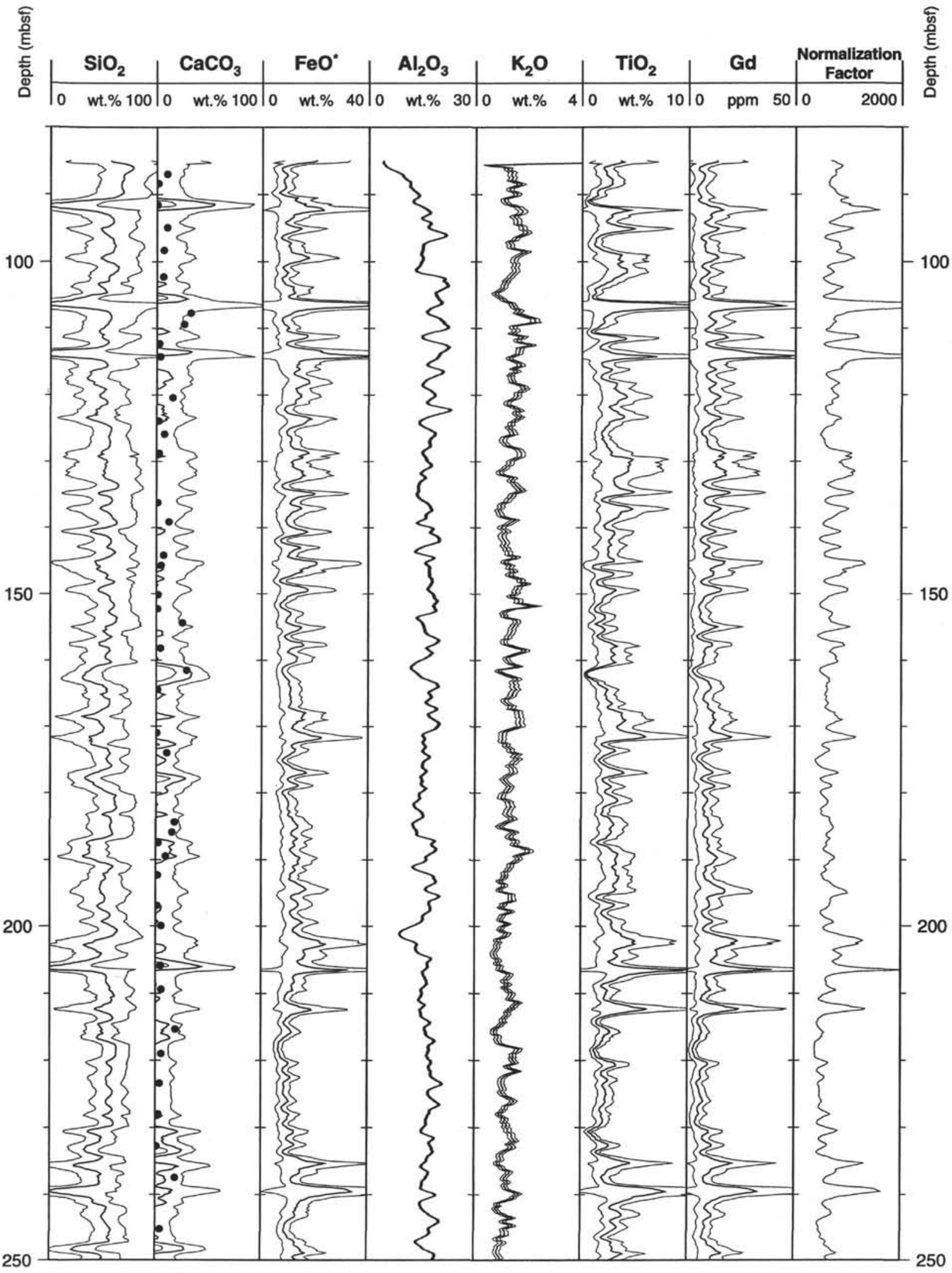

Hole 984B: Geochemical Logging Data (cont.)

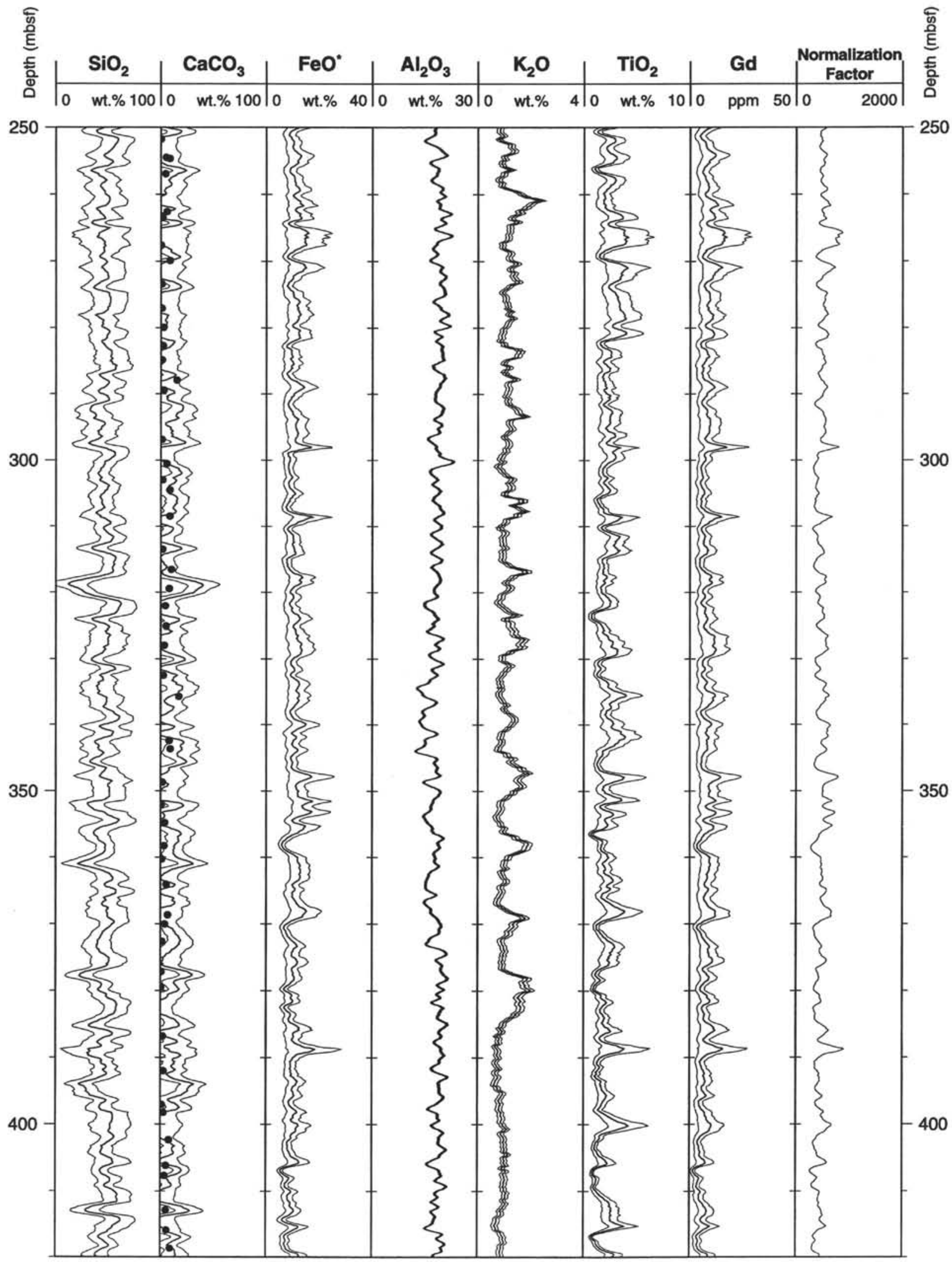

Hole 984B: Geochemical Logging Data (cont.)